

APPLICATION OF FIRST-ORDER SINGLE-REACTION MODEL  
FOR COAL DEVOLATILIZATION OVER A WIDE RANGE OF HEATING RATES

G.H. Ko, D.M. Sanchez, W.A. Peters, and J.B. Howard

Department of Chemical Engineering and Energy Laboratory  
Massachusetts Institute of Technology, Cambridge, MA, 02139

INTRODUCTION

The first-order single-reaction model offers a simple but effective mathematical description of coal devolatilization. Under conditions where the effects of physical transport processes and secondary reactions are relatively small but not negligible, the model approximates the complex chemical decomposition and any transport effects by a single global first-order decomposition reaction occurring uniformly throughout the particle. In more complete devolatilization descriptions that explicitly include mass transfer, the model represents only the chemical decomposition.

The model is most useful in applications where minimizing computational effort is important such as in large combustion or gasification models that fully describe fluid mechanics, heat and mass transport, and reaction kinetics; and in comprehensive devolatilization models that explicitly include the complex decomposition and secondary reaction chemistry, and multicomponent mass transfer in a gaseous or liquid phase environment. However, the model has a major weakness in that a different set of rate parameters is required at different heating rates. Thus, for a given set of rate parameters, the applicability of the model is confined to a narrow range of heating rates.

This paper presents a novel method to extend the applicability of the first-order single-reaction model over a wide range of heating rates. The two rate parameters in the model, a pre-exponential factor and activation energy, are derived in the form of heating rate dependent functions. The total weight loss data from devolatilization of a Montana lignite over heating rates from  $\approx 0.1$  to  $10^4$  C/s were used to illustrate the derivation procedure, and to test the reliability of this method.

EXPERIMENTAL DATA

The devolatilization weight loss data used in this work were obtained using the thermogravimetric analyzer at low heating rates (0.67-2.67 C/s) (1), and the electrical screen-heater reactor at high heating rates (650- $10^4$  C/s) (2). In both reactors, small samples (<20 mg) of a Montana lignite in the particle size range 50 to 100  $\mu$ m were used, with reactor conditions of 1 atm pressure and 1000 C maximum temperature.

The maximum volatiles yield,  $V^*$ , indicated by the upper asymptotic limit of the time-resolved yield curve, is one of the input parameters in the first-order single-reaction model. For a Montana lignite,  $V^*$  can be assumed to be independent of heating rate since the experimentally observed  $V^*$  is reported to be constant at  $\approx 40$  wt% (as-received) between the heating rates of 0.1 and  $10^4$  C/s (1,2,3). For higher rank coals, e.g., softening HVB coals, this assumption is still valid, but only over a narrower heating rate range. Suuberg et al. (3) observed a constant  $V^*$  of 47 wt% (as-received) between the heating rates of 350 and 15,000 C/s for a Pittsburgh Seam HVB coal under 1 atm, whereas Serio (4), and

Weimer and Ngan(5) reported a much lower  $V^*$  of 30 to 37 wt% (as-received) between 0.05 and 0.2 C/s for the same type of coal.

#### MODEL DESCRIPTION

The rate of volatiles evolution in the first-order single- reaction model is represented as,

$$dV/dt = k_{os} \exp(-E_s/RT) (V^* - V) \quad (1)$$

where  $V$  is the cumulative amount of volatiles evolved up to time  $t$ ,  $V \rightarrow V^*$  at large  $t$ , and the subscript  $s$  denotes single-reaction. The global rate parameters,  $k_{os}$  and  $E_s$ , are heating rate specific, and thus a given set is only applicable over a narrow range of heating rates. This limitation restricts the use of the model over the confined heating rate range in which the rate parameters are valid.

Integrating Eq.(1), using the approximation of Agrawal and Sivasubramanian (6), under a constant heating rate,  $m$ , up to temperature,  $T$ , yields

$$\ln [(V^*-V)/V^*] = \frac{-k_{os}RT^2}{mE_s} \left[ \frac{1-2(RT/E_s)}{1-5(RT/E_s)^2} \right] \exp(-E_s/RT) \quad (2)$$

The above equation was found to be the most accurate integral approximation among different methods reported in the literature (7,8,9). The approximation deviates  $< \pm 1\%$  from Simpson's 1/3 numerical method for the ranges of  $E_s$  and  $T$  typically encountered in coal devolatilization ( $E_s > \approx 10$  kcal/mole and  $T < \approx 1000$  C).

Another commonly used global devolatilization model, the multiple independent parallel reaction (MIPR) model was used (next section) to represent the experimental weight loss data from different heating rates. With just one set of rate parameters, the MIPR model successfully describes volatiles evolution data with heating rates that span several orders of magnitude (2,5,10,11), but it has a drawback in that it requires more computational effort. The rate of volatiles evolution in the MIPR model is expressed as the sum of the contributions from multiple first-order independent parallel reactions,

$$dV/dt = \sum k_{oi} \exp(-E_i/RT) (V_i^* - V_i) \quad (3)$$

where  $i$  denotes one reaction. The same pre-exponential factor is used for all reactions, i.e.,  $k_{oi} = k_o$ , and the activation energies are described by a Gaussian distribution with mean  $E_o$  and standard deviation  $\sigma$ . Thus,

$$f(E) = [\sigma(2\pi)^{1/2}]^{-1} \exp[-(E-E_o)^2/2\sigma^2] \quad (4)$$

where  $f(E) = V_i^*/V^*$  for a large number of reactions and  $V^*$  is the sum of the  $V_i^*$  for all  $i$ . Integration of Eq.(3) for any temperature history yields

$$(V^*-V)/V^* = \int_0^\infty \exp[-k_o] \int_0^t \exp(-E/RT) dt f(E) dE \quad (5)$$

## DERIVATION OF HEATING RATE DEPENDENT KINETIC PARAMETERS

To extend the use of the model over a wider heating rate range, we sought to relate  $E_s$  and  $k_{OS}$  to the heating rate,  $m$ , in the form of

$$E_s = f(m) \quad (6)$$

$$k_{OS} = g(m) \quad (7)$$

where  $f$  and  $g$  represent mathematical functions derived below.

The combined weight loss data of Ciuryla et al.(1) and Anthony et al.(2) were fitted using the MIPR model. Table 1 gives the best-fitted parameter values from fitting the combined data set, as well as those obtained by Ciuryla et al.(1) and Anthony et al.(2) using only their own data. The two groups of investigators(1,2) have shown that this model has an excellent capability to fit the data over a wide range of heating rates with just one set of parameter values.

An arrhenius plot (Fig.1) was then produced using the rate of total volatiles evolution predicted by the MIPR model at heating rates 0.1, 1, 10,  $10^2$ ,  $10^3$ , and  $10^4$  C/s [Eq.s (3) and (5), Table 1(c)]. The lines in the figure are sufficiently straight to assume a first-order single-reaction behavior for each of the heating rates. Table 2 gives the values of  $E_s$  and  $k_{OS}$  computed from Fig.1, which respectively represent the slope and the y-intercept of the lines in the figure.

Plotting individually the values of  $k_{OS}$  and  $E_s$  versus  $[3+\log_{10}(m)]$  from Table 2 produced the following relationship:

$$\log_{10}k_{OS} = -3.16514 + 0.941867(3+\log_{10}m) \quad (8)$$

$$E_s = 5909.411 + 182.7911(3+\log_{10}m) + 66.80278(3+\log_{10}m)^2 \quad (9)$$

The correlation coefficient exceeded 0.999 in both cases, assuring that the rate parameters computed from the above equations closely agree with those obtained from Fig.1.

## RESULTS AND DISCUSSION

Figure 2 shows that the predicted weight loss behavior by the first-order single-reaction model [Eq.s (2), (8) and (9)] agree well with the data represented by the predictions from the MIPR model [Eq.s (3) and (5), Table 1]. Thus, with the heating rate dependent kinetic parameters derived in this study, the single-reaction model can successfully be applied over a wide range of heating rates. Furthermore, the use of the integral approximation of Agrawal and Sivasubramanian(6) allows the volatiles evolution rate equation [Eq.(1)] to be expressed in an analytical form, which considerably reduces the computational effort.

The empirical coefficients in Eq.s (8) and (9) are specific for the data from which they were best-fitted. However, since a given data set can accurately be described by a set of MIPR model parameters, a more general form of Eq.s (8) and (9) may respectively be represented as functions  $\psi$  and  $\phi$

$$\psi(E_s, E_0, \sigma, k_0, m, T) = 0 \quad (10)$$

$$\phi(k_{OS}, E_0, \sigma, k_0, m, T) = 0 \quad (11)$$

$V^*$  also varies for different data, but it has no effect on the rate parameters of either models. Equating  $[(dV/dt)/(V^*-V)]/\ln[(V^*-V)/V^*]$  from Eq.s (1) and (2) to that from Eq.s (3) and (5) yields the function  $\psi$  in the form of

$$E_s^2 + (QRT^2/m)E_s - [5(RT)^2 + 2QR^2T^3/m] = 0 \quad (12)$$

where  $Q$  is  $[(dV/dt)/(V^*-V)]/\ln[(V^*-V)/V^*]$  obtained from Eq.s (3) and (5), and is a function of only  $E_0$ ,  $\sigma$ ,  $k_0$ ,  $m$  and  $T$ . Having obtained  $E_s$  from Eq. (12), rearranging Eq. (1) yields the function  $\phi$

$$k_{OS} - [(dV/dt)/(V^*-V)] \exp(E_s/RT) = 0 \quad (13)$$

where  $[(dV/dt)/(V^*-V)]$  is obtained from Eq.s (3) and (5). Although rigorous, the above equations are too complex to readily observe the effect of changing  $E_0$ ,  $\sigma$ , or  $k_0$  on  $E_s$  and  $k_{OS}$ . Also, for the same reason, it is difficult to detect any relationship between Eq.s (8) and (12), and Eq.s (9) and (13).

Although qualitative, Table 3 provides a useful means to predict the effect of a new data set on  $E_s$  and  $k_{OS}$ . For a given heating rate, the new time-resolved rate (or yield) curve is characterized by  $T_{max}$  and  $T_{sig}$ , where  $T_{max}$  represents the temperature at which the maximum rate occurs, and  $T_{sig}$  the temperature spread of the curve. The temperature spread is arbitrarily defined as the range of temperatures in which the yield is between two fixed values [e.g., Ko et al. (11) used 15.87 and 84.13% of the final yield]. Some examples will illustrate how to use the table. E.g., 1: for a fixed heating rate, the new data have higher  $T_{sig}$ , but no change in  $T_{max}$ . Table 3 shows that the newly fitted  $k_{OS}$  must be lower to match the increased  $T_{sig}$ , and the new  $E_s$  must also be lower to off-set the increase in  $T_{max}$  caused by the lower  $k_{OS}$ . E.g., 2: again for a fixed heating rate, the new data have higher  $T_{max}$ , but no change in  $T_{sig}$ . The table shows that the newly fitted  $E_s$  has to be higher to match the increased  $T_{max}$ , and the new  $k_{OS}$  is unchanged. Table 3 can also be used to relate qualitatively  $E_0$ ,  $\sigma$ , and  $k_0$  to  $E_s$  and  $k_{OS}$ . For example, the reason why the fitted  $E_s$  and  $k_{OS}$  for the same data are generally smaller than the  $E_0$  and  $k_0$ , respectively, is that a finite  $\sigma$  requires  $k_{OS}$  to be smaller than  $k_0$  to produce to same  $T_{sig}$ . Since lowering  $k_{OS}$  increases  $T_{max}$ ,  $E_s$  must also be smaller to off-set the increased  $T_{max}$ .

The correlation procedure developed here can easily be applied to describe the evolution of total volatiles of other coals, and individual product species. A new set of  $E_0$ ,  $\sigma$ ,  $k_0$  and  $V^*$ , best-fitted using the MIPR model, can be used to represent the new data set. Despite the lack of rigorous proof, the form of the Eq.s (8) and (9) are expected to remain the same, only the coefficients need to be re-fitted using the newly computed values of  $E_s$  and  $k_{OS}$  at different heating rates.

## CONCLUSIONS

This work has demonstrated that the first-order single-reaction model can successfully be applied over a wide range of heating rates using the heating rate dependent kinetic parameters [Eq.s (8) and (9)].

The use of the integral approximation method of Agrawal and Sivasubramanian(6), provides an accurate analytical solution of the single-reaction model rate equation [Eq.(1)] for the ranges of  $E_s$  and  $T$  typically encountered in coal devolatilization.

The heating rate dependent kinetic parameters combined with this integral approximation are expected to be useful in applications where minimal computational effort is desired.

#### ACKNOWLEDGEMENTS

The authors are grateful to the U.S. Department of Energy, Morgantown Energy Technology Center, for financial support of this work under Contract No. DE-RA21-85MC-22049. A 1967 Science and Engineering Scholarship to GHK from the Natural Sciences and Engineering Council of Canada is also appreciated.

#### REFERENCES

1. Ciuryla, V.T., Weimer, R.F., Bivans, D.A., and Motika, S.A.: *Fuel*, 58, 748 (1979).
2. Anthony, D.B., Howard, J.B., Hottel, H.C., and Meissner, H.P.: *Fifteenth Symposium (International) on Combustion*, 1303, The Combustion Institute, Pittsburgh, 1974.
3. Suuberg, E.M., Peters, W.A., and Howard, J.B.: *Seventeenth Symposium (International) on Combustion*, 117, The Combustion Institute, Pittsburgh, 1979.
4. Serio, M.A., *Secondary Reactions of Tar in Coal Pyrolysis*, Ph.D. Thesis, Dept. of Chemical Engineering, M.I.T., Cambridge, Mass., 1984.
5. Weimer, R.F., and Ngan, D.Y.: *Am. Chem. Soc. Div. Fuel Chem. Preprints*, 24 (3), 129 (1979).
6. Agrawal, R.K., and Sivasubramanian, M.S.: *AIChE J.*, 33, 1212 (1987).
7. Coates, A.W., and Redfern, J.P.: *Nature*, 201, 68 (1964).
8. Gorbachev, V.M.: *J. Thermal Anal.*, 11, 125 (1977).
9. Li, C.H.: *AIChE J.*, 31, 1036 (1985).
10. Sprouse, K.M., and Schuman, M.D.: *Combustion and Flame*, 43, 265 (1981).
11. Ko, G.H., Peters, W.A., and Howard, J.B.: submitted for publication in *Energy and Fuel* (1987).

Table 1 : Best-Fitted Global Rate Parameters for the Multiple Independent Parallel Reaction Model Using Total Weight Loss Data from Montana Lignite.

	(a)		(b)	(c)	
Fitted By:	Ciuryla et al.(1)		Anthony et al.(2)	This Study	
Data Source:	Ciuryla et al.(1)		Anthony et al.(2)	Ciuryla et al.(1) Anthony et al.(2)	
Heating Rate: (C/s)	0.67	2.67	650-10 <sup>4</sup>	0.67-10 <sup>4</sup>	
Cooling Rate: (C/s)	- <sup>c</sup>	- <sup>c</sup>	≈200	≈200	
Log(ko/s <sup>-1</sup> )	13.22 <sup>b</sup>	13.22 <sup>b</sup>	13.22 <sup>b</sup>	13.22 <sup>b</sup>	8.91 <sup>a</sup>
Eo, kcal/mole	54.3	53.3	56.3	56.8	38.6
σ, kcal/mole	1.32	1.21	1.09	1.16	0.706
V*, wt% as received	41.1	41.2	40.6	41.0	40.0

<sup>a</sup> Allowed to vary. This set of parameters was used to produce Fig.1.

<sup>b</sup> This parameter was fixed.

<sup>c</sup> Continuous heating until all reactions are completed.

Table 2 : Computed E<sub>s</sub> and k<sub>os</sub> from the Arrhenius Plot in Fig. 1.

Heating Rate <sup>a</sup> C/s	Pre-Exponential Factor(kos) s <sup>-1</sup>	Activation Energy(Es) cal/mole
0.1	0.05076	6528
1	0.4578	7078
10	4.089	7718
10 <sup>2</sup>	36.19	8489
10 <sup>3</sup>	309.2	9385
10 <sup>4</sup>	2582.0	10480

<sup>a</sup> Continuous heating until all reactions are completed.

Table 3 : The Effect of Changing Tmax and Tsig on the Global Rate Parameters of the First-Order Single-Reaction Model ( $E_s$  and  $k_{os}$ ) and of the Multiple Independent Parallel Reaction Model ( $E_o$ ,  $\sigma$  and  $k_o$ ).

The Effect of Increasing(†) the parameter X on :		$T_{max}$	$T_{sig}$
Parameter X			
$E_s, E_o$		†	- <sup>a</sup>
$k_{os}, k_o$		†	†
$\sigma$		-	†

<sup>a</sup> No change.

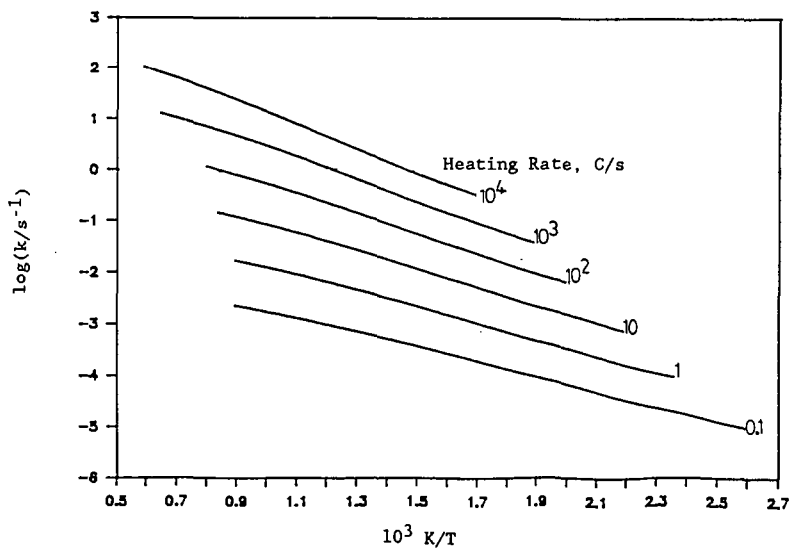


Figure 1 : Arrhenius Plot for Total Volatiles Evolution of Montana Lignite Described by the MIPR Model [Eq.(3) and (5), Table 1(c)]. The lines represent the rates computed between 1 to 99% of total volatiles yield.

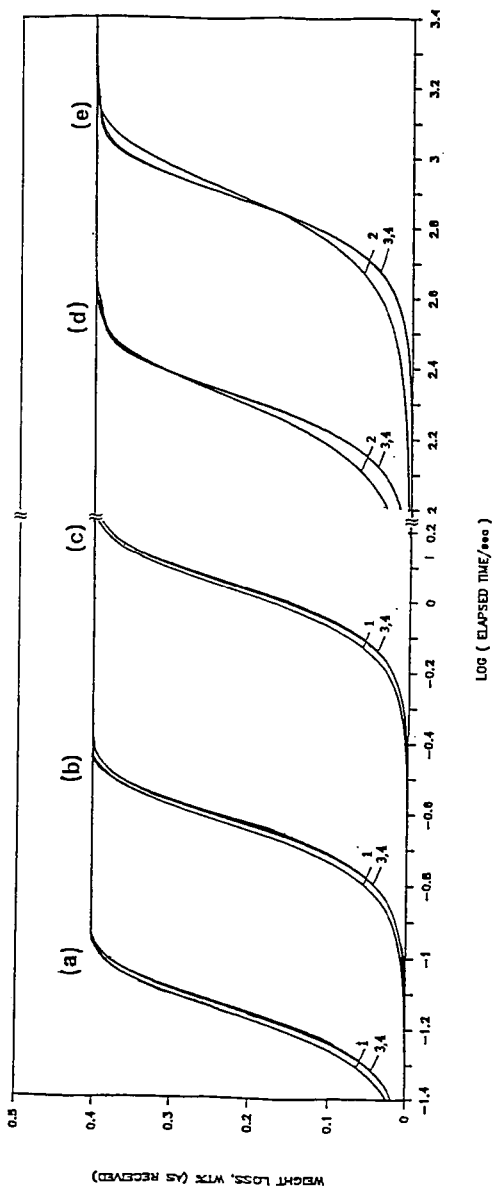


Figure 2 : Comparison of Predicted Total Volatiles Yield from the First-Order Single-Reaction Model [Eq.s (2), (8) and (9)] and from the MIPR Model [Eq. (5) and Table 1].

Heating, cooling rates in C/s (a)  $10^4$ , 200; (b) 3000, 200; (c) 650, 200; (d) 2.67 continuous heating to  $T_{max}$ ; (e) 0.67 continuous heating to  $T_{max}$  ( $\leq 1000$  C).

The curves represent model, source of kinetic parameters 1. MIPR, Anthony et al. (1974); 2. MIPR, Ciuryla et al. (1979); 3. MIPR, this study; 4. First-Order Single-Reaction, heating rate dependent kinetic parameters derived in this study. The kinetic parameter values for the curves 1, 2 and 3 are given in Table 1, and those for the curve 4 can be computed from Eq.s (8) and (9). For non-continuous heating cases [curve sets (a), (b) and (c)], let  $m$  be the equivalent heating rate equal to  $m_H m_C / (m_H + m_C)$  where  $m_H$  and  $m_C$  are heating and cooling rates respectively.



## NUMERICAL MODELING OF DIRECT SORBENT INJECTION FOR $SO_2$ REMOVAL

J. J. Lee

The University of Tennessee Space Institute, Tullahoma, Tennessee, 37388

### Abstract

A modeling study of steady, turbulent, reactive multi-phase flow in a duct injection flue gas desulfurization (FGD) system is reported in this paper. The stream-function/vorticity method was used in finite difference form. The  $\kappa$ - $\epsilon$  model was used for turbulence closure. A simple integrated formulation was employed to compute the behavior of sorbent droplets injected into the flue gas stream. The sorbent may be injected either as slurry or solution into a hot flue gas, or a dry sorbent may be injected into a cooled and humidified flue gas. A comprehensive heat and mass transfer model was developed to simulate the evaporation of the sorbent droplets and the absorption/reaction of  $SO_2$  in the sorbent droplets. Dissolution kinetics of lime particles within a slurry droplet was also included in this model to determine the overall  $SO_2$  removal rate. Numerical calculations and comparisons with available experimental data were made and are discussed.

### 1. Introduction

In the United States, the emission of sulfur oxides has attracted much attention. The dispersion of sulfur oxides arising from combustion of fossil fuels has a dramatic impact on the environment. Removal of sulfur oxides from flue gases is very important in air pollution control. A sorbent in-duct injection system is proposed as a method for flue gas desulfurization. Chemically the system is similar to a spray dryer or dry scrubber.

In the sorbent in-duct injection system, a chemically reactive sorbent, usually lime or hydrated lime or dolomite, is injected into a highly turbulent flue gas containing sulfur dioxide. The sorbent may be injected as slurry or solution into the hot (typically 275 to 350° F) flue gas, or a dry sorbent may be injected into a cooled and humidified flue gas (typically 160 to 180° F). Processes that occur in the duct include the evaporation of water from slurry or solution spray with resulting cooling and humidification of the gas; sorption of sulfur dioxide into the water of the slurry or solution droplet; dissolution of the slaked lime into the water; reaction of the sulfur dioxide with the lime or dolomite; and some as-yet less understood effects, such as, the reaction of sulfur dioxide with "dry" sorbent after evaporation of slurry or injection of dry sorbent following humidification of the gas.

The Energy Conversion Research and Development Programs of the University of Tennessee Space Institute (UTSI) is presently involved in research of direct sorbent injection for combined  $SO_2/NO_x$  removal under Department of Energy Pittsburgh Energy Technology Center contract<sup>1</sup>. Experiments are being conducted in the Direct Sorbent Injection Facility (DSIF). The objective of testing in this facility is to confirm the feasibility of a direct sorbent injection FGD system to control emissions of sulfur dioxide and nitrogen oxide from a fossil fuel plant. An extensive literature search also has been conducted at UTSI to collect and collate associated spray chemical reaction models.<sup>2</sup> As a prelude to the development of an in-duct sorbent injection FGD system for commercial application by 1992, this literature search was carried out by UTSI at the request of Brookhaven National Laboratory and Department of Energy, Pittsburgh Energy Technology Center. The overall objective of the study was to assist the above organizations in ascertaining the state-of-the-art of computational methods applicable to the in-duct sorbent injection FGD system. This effort included analysis of existing analytical models, identifying salient features and shortcomings, and determining the ability of these models to be extended to adequately design and scale-up sorbent injection systems.

From the above studies, it is found that there is an extremely large gap between the needs of the design engineer in practice and the understanding and proposed research tasks of the academic researcher who desires to make a contribution on the FGD modeling front. Literature which describes numerical models for the sorbent injection FGD process is limited. Numerical models for predicting chemical reaction in multi-phase turbulent flow occurring in in-duct sorbent injection systems rest on two foundations: mathematical models of physical processes (turbulence, evaporation, absorption, reaction, and multi-phase effects) and computer codes for solving the appropriate level of sophistication of the resulting nonlinear governing differential equations.

Attempts to calculate the detailed performance of the FGD processes have only been undertaken during the last few years. Prior to 1986, the best computations available were based on overall global calculations<sup>4-6</sup>. The details of the interaction processes between the flue gas and the reacting, evaporating particle/droplet were not quantitative. Modeling of turbulent, reactive multi-phase flow in a spray dryer FGD processes is still in a state of development. Recent reviews of this subject for the FGD systems are given in reference materials.<sup>1, 3, 5, 8, 10, 11</sup> It has been determined that no model currently exists that will completely and accurately model the complex flow field and chemical reactions that take place in the sorbent injection system. However, models are available for portions

of the overall process. The available models that have been reviewed at UTSI are summarized in reference 3.

One objective of the FGD research at UTSI is to develop a numerical modeling for predicting steady, turbulent, reactive multi-phase flow in a spray dryer FGD system. In the  $SO_2/NO_x$  removal process development, a modeling technique using an adaptation of the LEE-2 computer program<sup>2</sup> has been employed at UTSI to simulate operation of the experimental program in order to delineate data that has been collected and to provide a route which leads to the accomplishment of design objectives. These efforts have included analyses directed at achieving an adequate model of the gas/particle dynamics and heat/mass transfer with or without chemical reaction for evaluation of experiments.

## 2. FGD Modeling Efforts

This section summarizes the numerical models which characterize the complex gas/particle flow field features for the direct sorbent injection in the FGD system. This work was undertaken to aid in evaluation of experimental performance of the DSIF test train. Its objectives were to provide a means by which the flowfields and the  $SO_2$  removal process that develop within the FGD system could be viewed and qualified. Background on the model development and case studies that were performed using this numerical code in its original form are contained in the published works of Lee<sup>2,12-14</sup>. For this present study, the model was refined to make it more amenable to the FGD duct. These refinements included a recasting of the governing flow equations to incorporate the effects of multi-phase flow behavior. A detail description of the model used is much too involved for any indepth discussion herein. However, a general overview of the model highlighting some of its techniques and salient features is briefly presented in following paragraphs.

The numerical model provides a solution to the elliptical, fully turbulent form of flowfield conservation equations in either a two-dimensional Cartesian or an axisymmetric coordinate system. The gas dynamic model which utilizes a stream function/vorticity formulation to the Navier-Stokes equations for compressible, turbulent flows forms the basis for the modeling. This approach provides a powerful means of analyzing recirculating flows wherein explicit dependency of the flow upon pressure is eliminated. Recovery of both the pressure and the velocity distributions throughout the flow is accomplished once the stream function and vorticity are defined from solution. The model utilizes the standard high Reynolds number form of the  $\kappa$ - $\epsilon$  model for turbulence closure.<sup>15</sup> The model employs the law-of-the-wall and its related techniques to address near wall phenomena. This hypothesis allows realistic predictions of both wall shear losses and convective heat/mass transfer rates.

To solve the flow field equations in a non-equal spacing grid system a chain-rule technique is used to transform the physical spray-dryer plane into a rectangular computational plane. The governing equations and boundary conditions are rewritten in terms of computational plane coordinates and solved using finite-difference approximations. In order to extend the finite-difference equations beyond second order accuracy, a "decay function"<sup>16</sup> is introduced. This technique assures stability in numerical manipulation of the equations at interior grid points of computational field. Solution of the finite-difference equations together with prescribed boundary conditions is achieved by an iterative, point by point, successive under/over relaxation Gauss-Seidel scheme.

The equations needed to model the particle or droplet trajectories are the differential equations of motion<sup>17</sup>. The particle trajectories are computed by integrating these equations, gravitational force, gas viscosity and gas velocity are assumed constant over the time of integration. The spray model involves mass, momentum and energy transfer processes which through their mutual coupling define the local state of the flow. This coupling can be either unilateral or bilateral, in other words, it can be assumed that the effects on the gas flow of the spray embedded within it are negligible, or, the effects of the presence of particles on the gas phase can be accounted for. The unilaterally coupled spray trajectory model is a useful first approximation to the overall behavior of a spray within a complex aerodynamic flow field. This technique becomes more exact as the spray becomes more dilute. Therefore, unilateral coupling is assumed for the spray trajectory model for the initial investigation. In order to employ this assumption, particle trajectories are computed by the equations of motion given the gas phase flow field for a variety of assumed initial particle sizes, velocities, and spray angles.

A heat and mass transfer model, SPRAYMOD, of  $SO_2$  removal in a spray-dryer FGD system developed by Damle<sup>5</sup> was employed to simulate the evaporation of the sorbent droplets and the absorption/reaction of  $SO_2$  in the sorbent droplets. The code of SPRAYMOD was written in BASIC. This code was translated to FORTRAN for incorporation into LEE-2. The model is based on the assumption that the spray dryer could be simulated using a plug or backmixed flow model. Under this assumption, the effect of relative velocity between the flue gas and droplet is ignored. If the relative velocity is zero, the evaporation is the same as in a still-air condition. However, the initial velocity of the droplet at the exit of the nozzle is much higher than the surrounding flow. The effects of relative velocity on the simultaneous heat transfer from gas phase to the droplet, and mass transfer from the droplet to the gas phase have been considered during the constant rate of drying period. The particle/droplet trajectories of various droplet sizes and sorbent particle diameters superimposed in the two-dimensional turbulent flow stream have also been taken into account.

### 3. Results and Discussions

The numerical results performed in modeling of the DSIF are presented and discussed. A uniform gas velocity profile (Figure 1) adjusted in magnitude to satisfy mass conservation was used at the entrance to the test duct. Shown in Figure 2 is a 16" ID, 18' long cylindrical duct. Flue gas at 305° F enters from the left with a velocity of 10 m/s. The water particles at 110° F with a uniform velocity of 36 m/s enters from the left through a single water spray nozzle producing a 35° cone. The trajectories of the evaporating and reacting particles were calculated once the gas flowfield was obtained from solution. Figure 2 shows the trajectories of particles 25  $\mu$ m in diameter superimposed in the gas flow stream. The shape of the particle trajectory is directly influenced by the magnitude and relationship between the drag forces and the buoyancy forces. A comparison to experimental data<sup>1</sup> obtained from the DSIF is shown in Figures 3 and 4. Therein it can be seen that the two-dimensional model for predicting this turbulent, two-phase flow is in near agreement with the laboratory experiments.

Figures 5-11 show the predicted  $SO_2$  removal efficiency for both sorbent solution (sodium carbonate) and slurry (hydrated lime) cases. The results were computed subject to variety of sorbent particle diameters, dry sorbent reaction rate coefficients, inlet droplet diameters, inlet droplet temperature, inlet gas temperature, approach to saturation, and  $Ca/S$  stoichiometric ratio. The specifications for the spray dryer chosen as a reference case was based on the input conditions of DSIF SL00103A<sup>17</sup>. These are as follows: inlet gas temperature of 722 R, inlet gas velocity of 30 ft/sec, inlet droplet temperature of 600 R, inlet droplet diameter of 40 micron, inlet droplet velocity of 250 ft/sec, inlet  $SO_2$  of 1171 PPM, a molecular weight of sorbent ( $Ca(OH)_2$ ) of 74 lb/mole, sorbent density of 137 lbm/ft<sup>3</sup>, sorbent particle diameter of 4 micron, dry sorbent reaction rate coefficient of  $1.0 \times 10^7$ , mole fraction of water in inlet gas of 9.3, approach to saturation of 29° C, and  $Ca/S$  stoichiometric ratio of 1.86. The discussion of these figures are given as following:

**Effect of Inlet Sorbent Particle Size.** Figure 5 shows that  $SO_2$  removal efficiency decreases with increasing inlet sorbent particle diameter for the sorbent slurry. Smaller sorbent particles provide a larger cumulative surface area for reaction and would, thus, enhance the  $SO_2$  removal efficiency. On the other hand, since the sorbent solution are highly soluble, the  $SO_2$  removal efficiency is expected to be higher than that of sorbent slurry case. The sorbent solution case is shown not to be a function of inlet sorbent particle size.

**Effect of Inlet Droplet Size.** Figure 6 shows that  $SO_2$  removal efficiency slightly decreases for the sorbent solution and slightly increases for the sorbent slurry with increasing inlet droplet diameter.

**Effect of Dry Sorbent Reaction Rate Coefficient.** The reaction rate coefficient depends on the diffusivity of  $SO_2$  in the solid material, the particle size, and the moisture content of the particle/droplet.<sup>9</sup> The ability of the chemical reaction model to predict observed efficiency is highly dependent on the user's choice of a reaction rate coefficient. Figure 7 shows the correspondence between the reaction rate coefficient and  $SO_2$  removal efficiency for the set of operating conditions. This figure indicates that the reaction rate coefficient does not affect the efficiency until the coefficient exceeds a value of  $10^6$  cm<sup>2</sup>/gmole.s. In the present study, a value of  $10^7$  was assumed until further information becomes available.

**Effect of Inlet Droplet Temperature.** Figure 8 shows that  $SO_2$  removal efficiency decreases very slightly with increasing inlet droplet temperature for both solution and slurry cases.

**Effect of Inlet Gas Temperature.** Several conclusions have been reported regarding the effect of inlet gas temperature on  $SO_2$  removal efficiency. The experimental results performed by Apple and Kelly<sup>18</sup> indicate that  $SO_2$  removal efficiency increases with increasing inlet gas temperature. However, Buell<sup>9</sup> concluded from his experimental tests that the inlet gas temperature has a negligible effect. The numerical results performed by Damle, et al.<sup>9</sup> and Ma, et al.<sup>10</sup> indicate that  $SO_2$  removal efficiency increases slightly with increasing inlet gas temperature. Figure 9 shows that  $SO_2$  removal efficiency increases for the sorbent solution and decreases for the sorbent slurry with increasing inlet gas temperature. This implies that the effect of inlet gas temperature on  $SO_2$  removal efficiency depends upon the form of sorbent.

**Effect of Approach to Saturation.** Approach to saturation is defined as the difference between flue gas exit temperature and dew point. Once the gas exit temperature and dew point are defined from the solution based on the process stream material and energy balance, the approach to saturation temperature can be computed. This is an important process parameter. Numerical results indicate that  $SO_2$  removal efficiency decreases with increasing approach saturation temperature<sup>6,9</sup> as illustrated in Figure 10. This is due to the decrease in total droplet area resulting from the decreased volume of spray during the drying period and the decrease in core volume of equilibrium water held by the solid after the drying period ends.

**Effect of Inlet  $Ca/S$  Stoichiometric Ratio.** Stoichiometric ratio is defined as the moles of  $Ca(OH)_2$  fed to the system per mole of  $SO_2$ . This parameter is thought to be the most important factor influencing the FGD system performance. The overall  $SO_2$  removal efficiency increases successively with increasing inlet  $Ca/S$  ratio.<sup>4,6,9,19</sup> Figure 11 demonstrates this for both sorbent solution and slurry cases. This is due mainly to the decrease in liquid-phase resistance to  $SO_2$  mass transfer during the drying period.

Finally, a comparison to DSIF experimental  $SO_2$  removal data for this calculation is given in Figure 12. The

model predicted the  $SO_2$  removal efficiency with a tendency to under-predict at the upstream of the spray dryer. Since no good correlations are available to estimate the liquid-phase resistance in the droplet to the mass transfer<sup>5</sup> the difference between predicted and measured efficiencies was anticipated.

#### 4. Conclusions

The numerical results presented above predict several significant phenomena in the FGD system. Although it is the author's opinion that a full understanding of these phenomena is far from being achieved, it is hoped that these results will aid in advancing the future research efforts. Major highlights and conclusions of the present study are:

1. A general two-dimensional computational procedure was developed to model steady, turbulent, reactive, multi-phase flow in a spray dryer FGD system. A chemical modeling program, SPRAYMOD, was successfully incorporated into a general fluid modeling program, LEE-2.
2. The effects of relative velocity on the simultaneous heat transfer from gas phase to the droplet, and the mass transfer from the droplet to the gas phase were considered during the constant rate of drying period. The particle/droplet trajectories superimposed in the two-dimensional turbulent flow stream were also taken into account.
3. Comparison with one set of the DSIF data shows good agreement between model predicted and observed particle velocity distributions.
4. Parametric studies reviewed herein have brought to light some of the gross effects of inlet-gas specifications and operating parameters on the duct injection FGD performance. The numerical results show that inlet  $Ca/S$  stoichiometric ratio remains the single most important aspect of the duct injection on its performance. However, other variables which showed appreciable influence included the dry sorbent reaction rate coefficient and the form of sorbent. This study provided a considerable insight for duct injection FGD performance optimization and scale-up.
5. To correct the tendency to under-predict the  $SO_2$  removal efficiency at the upstream of the duct injection would require modeling of the wet particle stage.
6. A three-dimensional numerical model for a duct injection FGD system will be pursued as a future effort to compute the gas flow field, the droplet or sorbent particle dynamics, and the evaporation and chemical reactions simultaneously. The droplet/particle size distribution, agglomeration of particles, and wall deposition should also be considered in the model.

#### Acknowledgement

The author would like to thank Mr. T. E. Dowdy and Dr. J. M. Henry for providing valuable suggestions on the chemical model. The author would also like to thank Professor J. T. Lineberry for his assistance with this work. This work was sponsored by the U. S. Department of Energy under Contract DOE/PETC-DE-AC22-85PC81008.

#### References

1. Dowdy, T. E., et al., "Direct Sorbent Injection for Combined  $SO_2/NO_x$  Removal," Annual Technical Progress Report, DOE Contract No. DE-AC22-85PC81008, August 1985 - July 1986.
2. Lee, J. J., "Theoretical Studies of Recirculating Duct Flows for the UTSI MHD Combustor and Diffuser Designs," Ph.D. Dissertation, The University of Tennessee, Knoxville, December 1983.
3. Sheth, A. C., et al., "Review of Fluid Dynamics Math Models for In-Duct Sorbent Injection FGD Systems," Process Sciences Division, Department of Applied Science, Brookhaven National Laboratory and United States Department of Energy, Pittsburgh Energy Technology Center, November 1987.
4. Parsons, E. L., et al., " $SO_2$  Removal by Dry FGD," Proceedings of Sixth Symposium on Flue Gas Desulfurization, Houston, Texas, EPA-600/9-81-0196, Vol. 2, April 1981.
5. Damle, A. S., "Modeling of  $SO_2$  Removal in Spray-dryer Flue-gas Desulfurization System," EPA/600/7-85/038, December 1985.
6. Harriott, P and Kinzey, M., "Modeling the Gas and Liquid Phase Resistances in the Dry Scrubbing Process for  $SO_2$  Removal," Third Annual Pittsburgh Coal Conference, Pittsburgh, PA, September 1986.
7. Maibodi, M., "Simulation of Spray Dryer Absorber for Removal of  $SO_2$  from Flue Gases," M. S. Thesis, University of Tennessee, Knoxville, March 1986.
8. Pearson, T. E., "Mathematical Model for the Removal of Sulfur-Dioxide in a Pilot Scale Spray Dryer," M. S. Thesis, University of Tennessee, Knoxville, March 1984.
9. Damle, A. S. and Sparks, L. E., "Modeling of  $SO_2$  Removal in Spray Dryer Flue Gas Desulfurization System," 1986 AIChE Spring National Meeting, New Orleans, LA, April 1986.
10. Ma, H. K. Huang, H. S., and Chiu, H. H., "Turbulent Group Reaction Model of a Spray Dryer Scrubber," Accepted for Publication in the International Journal of Energy Systems.

11. O'Rourke, P. J., Wadt, W. R., "Two-Dimensional, Two-Phase Numerical Model for Spray Dryers," NTIS, PC A06/MF A01, Order No. DE82021847, July 1982.
12. Lee, J. J., Lineberry, J. T., and Wu, Y. C. L., "MHD Diffuser Studies," 23rd SEAM, Paper Ref. No. 22, Somerset, PA, June 1985.
13. Lee, J. J. and Lineberry, J. T., "Theoretical Studies of CFFF Radiant Furnace," AIAA-87-0385, AIAA 25th Aerospace Sciences Meeting, Reno, Nevada, January 1987.
14. Lee, J. J. and Schulz, R. J., "Numerical Studies of Recirculating Ducted Flows," Journal of Propulsion and Power, Vol. 3, No. 4, July-August 1987.
15. Launder, B. E. and Spalding, D. B., "The Numerical Computation of Turbulent Flows," Computer Methods in Applied Mechanics and Engineering, Vol. 3, pp 269-289, 1974.
16. Chien, J. C., "A General Finite-Difference Formulation with Application to Navier-Stokes Equations," Computers and Fluids, Vol. 5, pp 15-31, 1977.
17. Dowdy, T. E., et al., "Direct Sorbent Injection for Combined  $SO_2/NO_x$  Removal," Quarterly Technical Progress Report, DOE Contract No. DE-AC22-85PC81008, January-March 1987.
18. Apple, C. and Kelly, M. E., "Mechanisms of Dry  $SO_2$  Control Processes," Radian Corporation's Report, 1983.
19. Partridge, G. P., et al., "A Mathematical Model for  $SO_2$  Removal in a Spray Dryer Absorber," 1987 AIChE Spring National Meeting, Houston, Texas, March 1987.

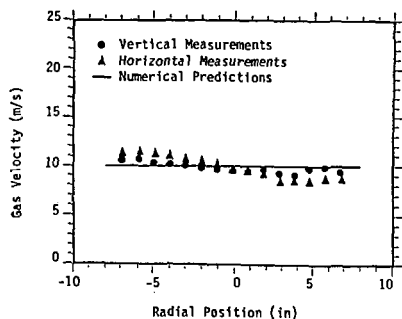


Figure 1. Gas Velocity Profile at Inlet to Test Section

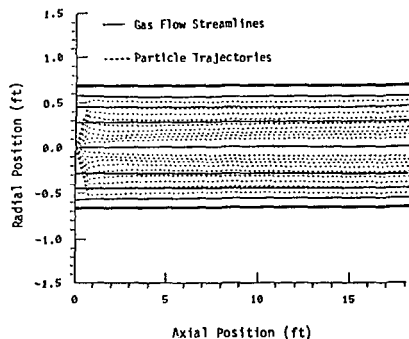


Figure 2. Particle Trajectories of  $25\mu\text{m}$  in Diameter Superimposed in the Gas Flow Stream

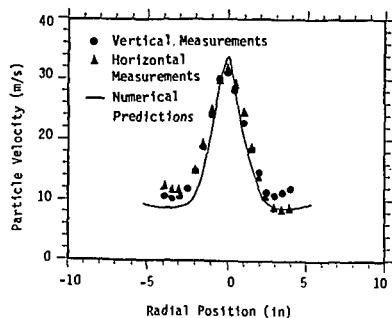


Figure 3. Particle Velocity Distributions, 18" Downstream of Spray Nozzle

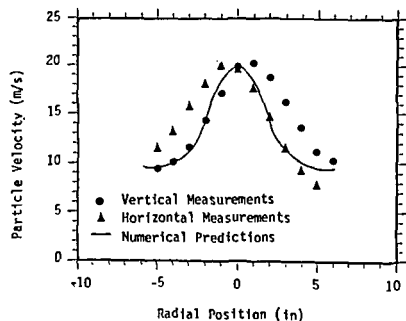


Figure 4. Particle Velocity Distributions, 36" Downstream of Spray Nozzle

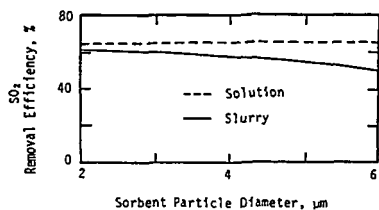


Figure 5. Effect of Inlet Sorbent Particle Size

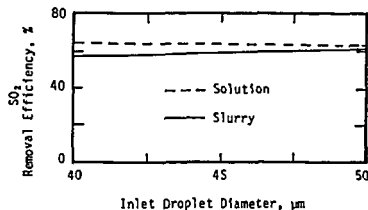


Figure 6. Effect of Inlet Droplet Size

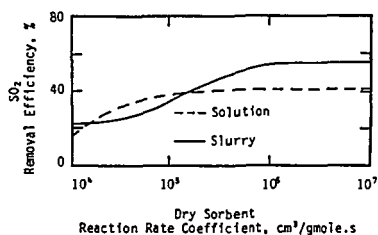


Figure 7. Effect of Dry Sorbent Reaction Rate Coefficient

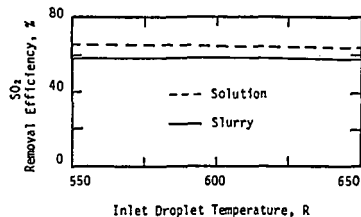


Figure 8. Effect of Inlet Droplet Temperature

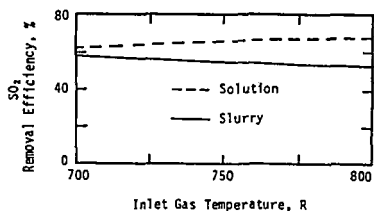


Figure 9. Effect of Inlet Gas Temperature

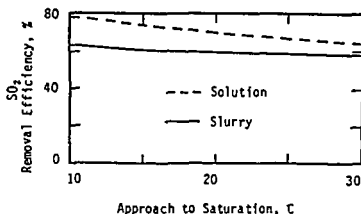


Figure 10. Effect of Approach to Saturation Temperature

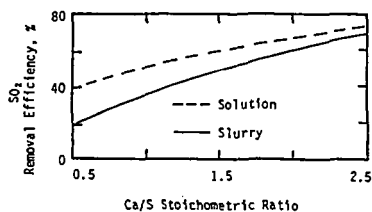


Figure 11. Effect of Inlet  $Ca/S$  Stoichiometric Ratio

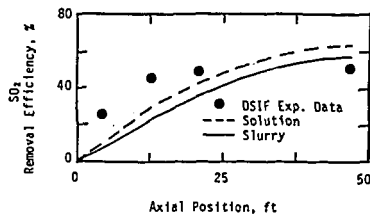


Figure 12. Calculated vs. Experimental  $SO_2$  Removal Efficiency

## A MECHANISTIC MODEL FOR AXISYMMETRIC CAVITY GROWTH DURING UNDERGROUND COAL GASIFICATION

Jerald A. Britten and Charles B. Thorsness

Lawrence Livermore National Laboratory, P.O. Box 808, L-367, Livermore, California 94550

Underground coal gasification (UCG) is a process in which coal energy is recovered without mining by artificially enhancing gas permeability in a section of a coal seam, igniting the coal remotely, partially combusting and gasifying coal by means of injected oxygen-steam-air mixtures, and collecting the product gas for cleanup and processing for a variety of end uses. The technology has been the subject of active field, laboratory and modeling research in the U.S. and Europe for more than 15 years, and during this time significant advances have been made and the process is nearing commercialization.

The size of the cavity formed during UCG impacts directly the economic and environmental factors crucial to its success. Lateral dimensions influence resource recovery by determining the spacing between modules, and ultimate overall dimensions dictate the hydrological and subsidence response of the overburden. Field experiments of UCG are expensive, and unless the cavity can be excavated after the experiment, cavity geometry can only be approximately inferred from post-burn coring, thermowell responses, electromagnetic and seismic mapping data and material balance calculations. In 1986, normal coal mining operations at the site of an UCG field test performed in 1983 near Centralia, Washington, the Partial Seam CRIP or PSC test (1), offered a unique opportunity to excavate a cavity of near-commercial scale. This excavation (2,3) provided data on ultimate cavity shape and characteristics which have profoundly aided our understanding of the UCG process. However, the data provide only indirect information as to cavity growth dynamics, and it is clear that a reliable mechanistic model for UCG cavity evolution and gas production would be extremely useful for site characterization and process simulation. Previous cavity growth models (e.g. (4-7)) are of limited use since they rely on one or more of the following: arbitrary assumptions regarding oxidant flow distribution in the cavity, oversimplification of some crucial phenomena at the expense of detailed modeling of others, or boundary conditions on upward or outward cavity growth, either arbitrarily chosen or fitted to field data, which decouple growth rates from heat and mass balance constraints. Also, until now detailed data for full-scale cavity dimensions were not available to compare with model results.

The model described in this paper applies to flat-seam UCG of subbituminous or lower rank coals in which the oxidant injection point remains low in the coal seam, and has progressed, we feel, to the point where it has become a useful tool with predictive ability for these conditions. It is based on a few key assumptions which are difficult to verify fully at the scale of interest, but which seem to be justified by model comparisons with field data. The global cavity growth model integrates results of interacting submodels describing water influx from the coal aquifer, dispersion of injected reactants in a rubble bed at the cavity bottom, thermal degradation and chemical attack of rubble-covered coal sidewalls, and recession of cavity surfaces enclosing a void space in the upper cavity, caused by radiation-driven spalling and gasification. Also, a submodel which calculates the growth of an outflow channel through which hot product gas flows to the production wellhead, is included for cases in which a horizontal uncased production borehole is utilized. The global model is of course highly idealized in the interest of tractability, and all apparent geometrical and physicochemical symmetries have been exploited to simplify the problem, but it retains sufficient physics to describe very well leading order UCG process

dynamics.

A mathematical description of the model and its many submodels would require far too many pages than allotted. The following sections describe briefly in words the submodels and their integration into the global cavity growth simulator, present comparisons of model results with results of two field experiments, and finish with a prediction of cavity characteristics for a proposed field test. Complete details of the model and its many parts can be found in (8-15).

## MODEL FORMULATION

The model envisions upward and outward growth of a cavity with origin at the point of injection of gaseous reactants. Figure 1 shows typical cavity cross-sections at varying stages of development. The cavity itself consists of up to four zones of differing properties: an ash rubble pile at the bottom of the cavity, left by reacted coal; a rock rubble or slag pile which can exist on top of the ash rubble once the cavity has grown to incorporate overburden rock; and a void space at the top of the cavity through which radiative heat transfer from hot rubble surfaces drives reaction and/or rubblization of exposed coal and rock surfaces. Also, geometrical considerations based on surface area distribution of the coal-void interface and the location of the oxygen source, reinforced by early modeling results and observations of the aforementioned excavated cavity, suggest that a pile of pyrolyzed char rubble can accumulate around the edge of the cavity and is therefore modeled. Densities of the rubble in the various regions are specified and assumed constant. Dynamics of flow, heat and mass transfer, and chemical reaction in and across these zones and in the surrounding coal seam are described by the following submodels, and results incorporated into the global cavity growth simulator. Reaction chemistry is simplified by lumping  $CO_2 + H_2O$  and  $H_2 + CO$  into single gasification reactant and product species, respectively, with suitably defined heats of formation (15). This simplification is justified by the similar stoichiometric and kinetic behavior of the individual species in the reactions of importance. By use of the assumption of equilibrium of the water-gas shift reaction at the calculated product gas temperature and a carbon balance, detailed gas compositions can be calculated from model results. The model does not treat tar evolution or its secondary reactions.

**Water Influx Submodel** Water influx to a UCG reactor plays a major role in determining process efficiency. Water can enter the reactor through drying of overburden rock, gravity drainage, depressurization of the coal aquifer, and reflux of condensate from escaped product gas if gas losses to the formation occur. Although some water in the UCG reactor is essential as a gasification agent, often far more than desired enters the reactor, and the energy necessary to vaporize and heat it to the product gas temperature is essentially lost.

The water influx submodel used in the global simulation, described in detail in (8), calculates flow of free water through the (assumed) homogeneous aquifer of the coal seam by gravity drainage, which occurs independent of the reactor pressure, and depressurization of the coal seam, which occurs when the reactor is operated below the hydrostatic pressure. The model assumes that strata above and below the coal seam are impermeable. (Water from overburden drying is accounted for naturally in the roof recession submodel.) Reactor geometry in the influx submodel is idealized as a cylinder extending the full height of the seam representing the cavity, and a noninteracting slot of variable width representing a horizontal outflow channel. Cylinder and slot volumes are specified by demanding equality with cavity and outflow channel volumes at each time step. We assume that gas displacing the water in the coal strata is of sufficiently high mobility that only the flow equations for the water-filled region need be considered. Also, capillary pressure effects are assumed negligible. These assumptions imply that the gas pressure on all



water/gas interfaces are equal. The two-dimensional (radial and axial) flow problem for gravity drainage is reduced to a one-dimensional problem by use of the so-called Dupuit approximation (16) which considers Darcy flow only in the radial direction based on a radial gradient in piezometric head. This system has been solved numerically using a finite difference scheme to discretize the differential equation in the space dimension and integrating the resulting system of ODE's in time using a standard solver. In (8) it is shown that, except for very early times, the Dupuit approximation gives flowrate values in very close agreement with those calculated by solution of the full two-dimensional solution, for both stationary and uniformly expanding cylinder walls. Depressurization is included in this formulation by matching the drainage solution valid in the cone of depression with the solution for unsteady potential flow in the fully saturated far field aquifer, at the boundary where both solutions are valid.

In coupling the water influx submodel to the global cavity growth solution, the model equations are solved for a fixed geometry over a time interval equal to the time step of the full problem. At the start of each time step a new grid system is established with its inner boundary on outer edge of the cavity or outflow channel. Values of hydraulic head are obtained through interpolation of the previous solution. Drainage and depressurization water is assumed to enter the at the ash-rubble covered sidewall in the lower cavity. Values for parameters characterizing water influx, with the exception of flow porosity, can be obtained from standard well hydrology testing. One additional parameter, an initial pumping time, has been introduced to make allowance for the time during which the wells are pressurized or pumped down before initiating the UCG burn.

Injection Gas Flow Submodel At any instant flow through the ash rubble is quasi-steady, since the evolution of its geometry is over a much longer time scale than the flow residence time. The flow distribution is described by the compressible form of Darcy's law in the axisymmetric volume of the ash rubble pile (see Figure 1), with a source term at the origin, and an impermeable cavity floor. We assume a region of high permeability exists at the ash pile-coal sidewall boundary, since it is here that void space is being created by removal of carbon and volatiles from the coal. This assumption is critical to the success of the model. We also assume that the char rubble overlying the outer edges of the ash rubble is highly permeable. This is justified by observations of rubble characteristics of the excavated UCG cavity (3). These assumptions imply that the sides and top of the ash rubble are at the same sink pressure while the cavity remains in the coal seam. Once rock rubble enters the cavity, a resistance to upward flow through the central ash pile is added, proportional to the height of the rock rubble and the permeability ratio of rock to ash rubble. The system is solved by a finite difference method. A vertical half-plane with origin at the center of the axisymmetric rubble pile is mapped onto a grid rectangular in  $r$  and  $z$  coordinates, which is normalized at each time step to maximize the number of nodes lying inside the rubble pile. Permeability values at nodes lying on or outside the rubble pile are set very large, effectively tying the edge of the pile to the sink pressure  $P_s$ . The difference equations for the pressure at each node, linear in  $P^2$ , are solved iteratively using successive overrelaxation. The solution for the previous time step is used as the initial guess for the next step. Calculated fluxes at boundary nodes are smoothed with a polynomial fit for each of the interfaces adjacent to the coal sidewall, void and char bed. The integrated flow out of the entire boundary is normalized with the injection flow to remove errors introduced by the smoothing, and average flowrates to each of the three zones are computed.

Wall Recession Submodel The wall region is defined as the cavity boundary extending downward to the cavity floor from point d in Figure 1A. We assume the existence of a thin, highly permeable, char-filled zone between the ash and the solid coal wall. Here oxygen entering from the ash side

combusts char, supplying heat to drive gasification reactions, vaporize and heat influxed water and dry, pyrolyze and degrade fresh coal to char rubble. The net effect of this rubblization, which involves relaxation of thermal and drying induced (shrinking) stresses coupled with overburden stresses at the solid wall, is to propagate this permeable reaction zone into the coal. We describe this failure mechanism in terms of a convective heat transfer rate from hot gas at temperature  $T_w$  to the coal wall at a specified failure temperature  $T_f$ , with the heat flux balanced by that required to dry and heat coal to temperature  $T_w$  at the rate of the sidewall recession. Also, settling of char and/or ash from above and upward flow of product gas is considered to occur in this layer. Solution of the fully-coupled two-dimensional heat and material flow problem described here is far beyond the scope of a module to be used in a global UCG simulation. A major simplification is the division of the wall into several discrete elements in the axial direction, and the assumption that the temperature is constant within a given segment. This temperature is presumed to be given by the formula for the effective extinction temperature of the steam/char reaction in a packed bed (12,13), subject to the constraints of energy and mass balances and the convective heat transfer conditions at the cold coal wall. This temperature is primarily a function of the Arrhenius kinetic parameters of the steam-char reaction and the local flux of the product gas in the layer. This formulation allows the computation of recession velocities and char conversion rates for each segment.

Void/Rubble Zone Submodel This submodel describes the interaction of the coal, overburden and rubble pile surfaces enclosing the void region at the top of the developing cavity. Competent coal or rock surfaces here are exposed to high temperatures, and thermally induced and lithostatic stresses interact in a fashion not completely understood to cause spalling (small scale failure) of material on the order of centimeters to occur. A one-dimensional transient model (14,15) has been developed to describe drying, pyrolysis, gasification and spalling of coal (or rock) exposed to a constant high temperature radiative heat source. Spalling behavior is empirically characterized by a failure length  $\ell_f$  and a failure temperature  $T_f$ , in such a way that when the temperature a distance  $\ell_f$  from the surface exceeds  $T_f$ , an element of this size is removed from the surface and the process repeated. Values of  $\ell_f$  and  $T_f$  are obtained from analysis of one-dimensional transient heating experiments on overburden cores (17) when available, or appropriate values are chosen and regarded as model parameters. This model is used to calculate mean recession rates and related quantities, averaged over a series of spalls, as functions of the mean surface temperature. Heat transfer to the curved roof surface can be considered one-dimensional, since the thermal penetration depth is always much smaller than the local radius of curvature. The void space is assumed to be well-mixed.

The roof surface is divided into several conic sections. Oxygen exiting the top of the ash pile combusts with char which spalls onto this surface while the cavity is in the coal, and combusts product gas at the surface of the rock rubble when it is present, creating a hot surface which radiates to the other surfaces. Radiative exchange equations are written for the surfaces enclosing the void, in which the temperature of the roof surfaces determines their recession rates, and material and energy balances are solved (9,15) subject to two constraints, as discussed in a later section. While the cavity is in the coal seam, it is demanded that no char accumulate on the central surface of the ash rubble; all char arriving here must be reacted by combustion and gasification. When overburden rock is present, complete combustion of oxygen with product gas ( $H_2 + CO$ ) at this surface is demanded. The char pile at the outer cavity edge is considered a one-dimensional packed bed modeled as in (13) in which oxygen and steam entering from below react with char, and the product gas exits into the void. Reaction chemistry is simplified in this region by considering  $H_2 + CO$  as one chemical species, and  $CO_2 + H_2O$  as another, as described

in (15), with suitably defined reaction enthalpies.

**Outflow Channel Model** This model describes growth of an outflow channel, originally an open horizontal borehole in the coal seam, by thermally-induced rubblization of the coal as described above, driven by convective heat transfer from the hot product gas. Heat transfer is modeled in a semi-empirical fashion with constants fitted to the PSC excavation data (12). This channel is considered physically removed from the cavity such that no geometrical interaction occurs to break the symmetry of the cavity. Channel volumes calculated, and measured in the field, typically amount to about 10% of the main cavity volume.

**Global Cavity Growth Module** An initial cavity is defined as a series of line segments connecting points along one-half of a cavity cross section looking from the side. Initial cavities are defined as cylinders with unit height/diameter ratio and specified total, char and ash rubble volumes. (Parametric studies have shown that initial cavity configuration has a very small effect on late-time cavity characteristics.) This geometrical data is passed to the submodels which calculate temperatures, recession rates and chemical reaction rates for the various surface segments. The control segment then advances cavity segments over a time step, tentatively computes new cavity boundaries and rubble amounts. A unique cavity shape is calculated differently depending on whether the cavity interacts with overburden rock. When the cavity is contained in the coal, this shape is determined by noting that the amount of char which falls into the inner ash pile surface determines the upward growth of this surface, the temperature distribution in the enclosure and the amount of char remaining in the rubble bed. In other words, there is only one solution for the amount of char deposited on the ash-void interface, for which the location of point a in figure 1A simultaneously satisfies both char and ash material balances. When the cavity grows to encompass overburden rock, the ash pile ceases to grow upward and thus point b in Figure 1B is determined solely by the ash material balance. In this case the location of point a is fixed by simultaneous satisfaction of char and rock rubble material balances. Provision is made during late stages of cavity development for complete coverage of char by rock rubble, and also for the eventual depletion of the char rubble, by adjustment of point c in Figure 1D. The control algorithm also periodically performs various smoothing and point equalization operations on the calculated results. These are necessary since adjacent cavity points moving at significantly different velocities could cross paths if no intervention occurred, leading to highly irregular, multiply-connected cavity shapes numerically and physically unrealistic. Cavity volumes are computed before and after each smoothing operation and the errors incurred as a result of smoothing are recorded. For all cases considered, the cumulative smoothing error is about 3-6% of the total cavity volume. Time steps are constrained such that no point on the cavity surface can advance farther than a specified fraction of its distance from the cavity origin.

The present version of the code developed for this simulation requires relatively little memory and uses about 5 seconds per time step early on when an iteration on the void radiative exchange equations is required, decreasing to less than a second per time step for the latter stages of the calculation. Total cpu time on a Cray 1 computer needed for a 15 day simulation is about 3 minutes.

## RESULTS AND COMPARISON WITH FIELD DATA

**Partial Seam CRIP Field Test** The parameter with the largest effect on model results is the ratio of permeability between the rock and ash rubble piles. This parameter controls the split of injected oxidant flow between the sidewalls and the void region once overburden is exposed, which occurs relatively early in the life of the burn. Generally, oxidant which is forced to the cavity sidewalls

comes in intimate contact with coal, producing high quality gas, while oxidant passing into the void partially combusts product gas, heating overburden rock which represents an energy loss. A lower rock rubble permeability thus diverts more oxidant flow to the sidewalls, resulting in a wider, shorter ultimate cavity and enhanced energy recovery. This permeability ratio is very difficult to quantify. From observations of ash and rock rubble during the excavation of the PSC site (3) it was concluded that the rock rubble was probably somewhat less permeable than the ash, since much of it had fused, leaving an irregular network of fissures to conduct the gas, while the ash rubble clinker appeared relatively more porous. The effect of this permeability ratio is seen in Figure 2, which shows the molar ratio of produced hydrogen and carbon monoxide to injected oxygen, and excellent measure of process efficiency. Results using physical and process parameters given in Table 1A, corresponding to the PSC test conditions and with permeability ratios spanning three orders of magnitude, are here compared with test data. It is clearly seen that  $\kappa_R/\kappa_A = 1$  gives the best agreement. This result, and the observation that past field tests also exhibited gradual declines in product gas quality, instead of consistent high values or precipitous declines when overburden was encountered, suggest that this ratio is of  $O(1)$  and we therefore specify a value of unity for all subsequent calculations.

The model calculation for  $\kappa_R/\kappa_A = 1$  resulted in a final cavity shape which is compared in Figure 3 with that mapped during the excavation. The actual cavity was slightly asymmetric with respect to the injection point, but the agreement is quite good; both in sweep and the narrowing of the cavity midsection. This latter phenomenon occurs because this area of the cavity is covered for most of the burn with insulating char rubble, and is not exposed to direct oxidant attack as below, or high-efficiency radiative heat transfer as above. The simulation predicts total coal volume gasified to be  $675 \text{ m}^3$ . Analysis of the field data (1) suggest that about  $700 \text{ m}^3$  of coal was gasified during the part of the test in which this cavity was formed. While the upper part of the actual cavity was destroyed by mining operations and cavity shape in the overburden cannot be directly compared, but the good agreement in produced gas quality shown in Figure 2 suggests that the simulation calculated reasonably the volume of overburden affected.

**Rocky Mountain I Field Test** The recently completed Rocky Mountain I (RMI) UCG field test provides another opportunity to test model results with a system in which oxidant injection remained low in the coal seam. Flow and pressure schedules used during the test and parameter values taken from a number of literature sources characterizing the Hanna coal, given in Table 1B, were used as inputs in the simulation. Day zero is defined as the beginning of forward gasification with steam and oxygen, and the initial cavity volume is specified by carbon removed during air gasification which occurred for about 3 days prior. Figure 4 compares model results of  $(H_2 + CO)/O_2$  for these conditions with the test data. The agreement is striking. Figure 5 compares calculated cavity volumes with that calculated for the actual cavity by a material balance which assumes no char accumulation in the underground system. Also on this figure the product gas temperature is compared. Volumes agree quite well early but diverge by about 15% for later stages of the 40 day burn of the first cavity. Also, the predicted product gas temperature is somewhat higher than actual, though the slight upward trend with time is well-represented. The actual cavity shape is not reliably known, so no direct comparisons can be made. Qualitatively, the computed cavity shape is similar to that calculated for the PSC simulation, since this is largely determined by the proximate analysis of the coal, which is similar for these two coals.

Two weaknesses of the model are its neglect of the hydrogasification reaction ( $2H_2 + C \rightarrow CH_4$ ) and its neglect of tar evolution and secondary tar reactions. The former may account for the discrepancy in  $CH_4$  production between model and data (7% -vs- 11% respectively, on a dry gas

basis). This reaction is endothermic and thus its inclusion in the model would serve to reduce product gas temperature. Tar cracking could produce a considerable amount of  $H_2$  and  $CO$ , since tar amounts to as much as 15% by weight of the original coal (20). This could explain the equivalent  $H_2 + CO$  production rates between model and data, when the model predicts up to 15% more coal was affected. One must keep in mind in interpreting this test data, however, that it is raw data; known errors have not yet been removed.

**Proposed Brazilian UCG Field Test** As part of the Lawrence Livermore Laboratory effort to provide technical support for a UCG feasibility study in Brazil, cosponsored by the DOE, a simulation was performed using all available data concerning the coal and overburden at the proposed test site, near Porto Alegre in southern Brazil. This simulation provided estimates for sweep width and coal recovery used in planning link numbers and spacing for the two year demonstration test plan. Coal and overburden physical data specific to the site, as well as operating parameters are given in Table 1C. Rubble pile densities were adjusted from values measured at the PSC excavation based on the density differences in the original materials, and other necessary data unavailable for this site, such as coal and rock failure criteria, were taken as the same as for the PSC simulation. This test is of great interest because the characteristics of the coal, very dry, very impermeable and of a high ash content, represent conditions felt to be ideal for flat seam UCG.

Figure 6 shows the cavity shape produced by the simulation at approximately 11.5 days. The high ash content of this coal results in a larger volume of the cavity filled by ash rubble compared with coals previously studied. Thus, a larger fraction of the cavity surface is covered by rubble. The void region of the cavity is relatively small, such that the efficient radiative heat transfer mechanism dominant in the void is focused largely at the topmost part of the cavity, which gets quite hot and recedes rapidly. These factors combine to form a cavity wide at the bottom with a chimney-type upper end. The simulation was terminated when the void space became filled with bulked rubble, a situation that cannot be treated by the present model. The behavior of the system would not be expected to change substantially in the short term once the cavity is completely filled, however. The bed of pyrolyzed, unreacted char which persists in simulations of other UCG systems studied, disappears early on in this system. The volume of coal and rock affected by the cavity predicted by the simulation is 454 and 220  $M^3$ , respectively. The results suggest that gas production efficiencies at sites such as this are expected to be quite good, but very hot product gas temperatures may be experienced.

## CONCLUSIONS

A model for cavity growth and gas production during UCG, based on the assumption of cylindrical cavity symmetry and applicable for gasification of shrinking coals when injection low in the coal seam can be maintained, has been developed. The model is highly idealized, but treats includes all important factors impacting cavity growth such as water influx, porous media flow, heterogeneous and homogeneous chemical reactions, radiative and convective heat transfer, and rock mechanics. Model predictions have been shown to agree very well with available field data, and while detailed produced gas compositions cannot be estimated, it is felt quite adequate to describe in a semiquantitative fashion cavity evolution, energy recovery, aquifer response, and effects of process parameter changes, and therefore is a useful tool for UCG site characterization and module optimization.

**Acknowledgement** This work was performed under the auspices of the U.S. Department of Energy by Lawrence Livermore National Laboratory under contract number W-7405-Eng-48.

## REFERENCES

1. Cena, R.J., Hill, R. W. and Thorsness, C. B., (1988) 'The Partial Seam CRIP Underground Coal Gasification Test' Lawrence Livermore National Lab. UCRL rept. (in press)
2. Oliver, R.L., (1987) 'Results of the Controlled Excavation of the TONO I UCG Cavity, Centralia, Washington' Proc. 13th UCG Symp. (in press)
3. Cena, R.J., Britten, J.A. and Thorsness, C.B., (1987) (Proc. UCG Symp. (in press) Lawrence Livermore Nat'l Lab. preprint no. 97245
4. Chang, H.L., Himmelblau, D.M. and Edgar, T.F (1984) Proc 10th UCG Symp. U.S. DOE rept. DOE/METC/85-5 460-476.
5. Thorsness, C.B and Cena, R.J., (1983) Proc. 9th UCG Symp. U.S. DOE rept. DOE/METC/84-7 246-281
6. Kunselman, L.V., Faucett, D.W and Mones, C.G., (1983) Proc. 9th UCG Symp., U.S. DOE rept. DOE/METC/84-7 182-195
7. Riggs, J.B. and Edgar, T.L., (1983), in *Underground Coal Gasification, the State of the Art*, W.B. Krantz and R.D. Gunn, eds. AIChE Symp. Ser. 226 108-120
8. Thorsness, C.B. and Grens, E.A., (1987) Proc. 13th UCG Symp., (in press) Lawrence Livermore Nat'l Lab. preprint no. 97203
9. Thorsness, C.B. and Britten, J.A., (1986) Proc. 12th UCG Symp. DOE/FE/60922-H1 239-251
10. Grens, E.A. and Thorsness. C.B., (1985) Proc. 10th UGC Symp. DOE/METC-85-7 448-461
11. Grens, E.A. and Thorsness. C.B., (1986) Proc. 11th UGC Symp. DOE/METC-85/6208 413-423
12. Britten, J.A. and Thorsness, C.B., (1987) Proc. 13th UCG Symp., (in press) Lawrence Livermore Nat'l Lab. preprint no. 96461
13. Britten, J.A. (1988) 'Extinction Phenomena in Countercurrent Packed Bed Coal Gasifiers: A Simple Model for Gas Production and Char Conversion Rates' *Ind. Eng. Chem. Research* (in press)
14. Britten, J.A. (1986) *Int. J. Heat Mass Transfer* 29 965-978
15. Britten, J.A. and Thorsness, C.B., (1985) Proc. 11th UGC Symp. DOE/METC-85/6208, 365-380
16. Bear, J. (1972) *Dynamics of Fluids in Porous Media* American Elsevier Publishing, New York, ch. 8
17. Tantekin, S.B. (1986), M.S. Thesis, University of Colorado
18. Kotowsky, M.D. and Gunn, R.D., (1976) Laramie Energy Research Center rept LERC/RI-76/4
19. Mason, J.M., Oliver, R.L., Schrieber, J.D., Moody, C., Smith, P., and Healy, M.J., (1987) Western Research Institute Rept. 86-062
20. Hill, R.W. and Thorsness, C.B., (1987) Lawrence Livermore National Lab. rept. UCID 20951

**Table I. Physical and process parameters used in the simulations.**

**A. Partial Seam CRIP**

coal specific gravity 1.39, 17% water, 21% ash, 28% fixed carbon  
 rock specific gravity 2.10, 12% water  
 coal failure temperature (K) 700 (roof) 850 (sidewalls)  
 rock failure temperature (K) 700 (roof) 850 (sidewalls)\*\*  
 coal roof failure length (cm) 1; rock roof failure length (cm) 2  
 rubble specific gravities; ash 1.0, rock 1.3, char 0.8  
 permeabilities (mD); ash rubble 10000, rock rubble 10000, native coal 30  
 hydrostatic head (kPa)\* 630, pumpdown time (days) 10  
 seam height 6 (m), initial cavity height & radius (m) 1.0 & 0.5  
 nominal gas flow (mol/s) 30, steam/oxygen ratio 2/1, ramp time (days) 5  
 injection temperature (K) 400, cavity pressure (kPa) 430  
 References: (1), (3), (8)

**B. Rocky Mountain I**

coal specific gravity 1.39, 9% water, 27% ash, 32% fixed carbon  
 rock specific gravity 2.10, 10% water  
 coal failure temperature (K) 700 (roof) 700 (sidewalls)  
 rock failure temperature (K) 660 (roof) 660 (sidewalls)  
 coal roof failure length (cm) 1; rock roof failure length (cm) 1.7  
 rubble specific gravities; ash 1.0, rock 1.3, char 0.8  
 permeabilities (mD); ash rubble 10000, rock rubble 10000, native coal 140  
 hydrostatic head (kPa) 990, pumpdown time (days) 12  
 seam height 7.6 (m), initial cavity height & radius (m) 3.6 & 1.8  
 gas flow schedule from actual data, injection temperature (K) 400  
 cavity pressure schedule from actual data  
 References: (17), (18), (19)

**C. Brazil Test**

coal specific gravity 1.78, 8% water, 46% ash, 28% fixed carbon  
 rock specific gravity 2.42, 4% water  
 coal failure temperature (K) 700 (roof) 850 (sidewalls)  
 rock failure temperature (K) 700 (roof) 850 (sidewalls)  
 coal roof failure length (cm) 1; rock roof failure length (cm) 2  
 rubble specific gravities; ash 1.1, rock 1.5, char 0.9  
 permeabilities (mD); ash rubble 10000, rock rubble 10000, native coal 0  
 seam height 3.7 (m), initial cavity height & radius (m) 1.0 & 0.5  
 nominal gas flow (mol/s) 30, steam/oxygen ratio 2/1, ramp time (days) 5  
 injection temperature (K) 400, cavity pressure (kPa) 1500  
 Reference: (20)

\* measured from bottom of coal seam

\*\* best fit to excavated outflow channel volume

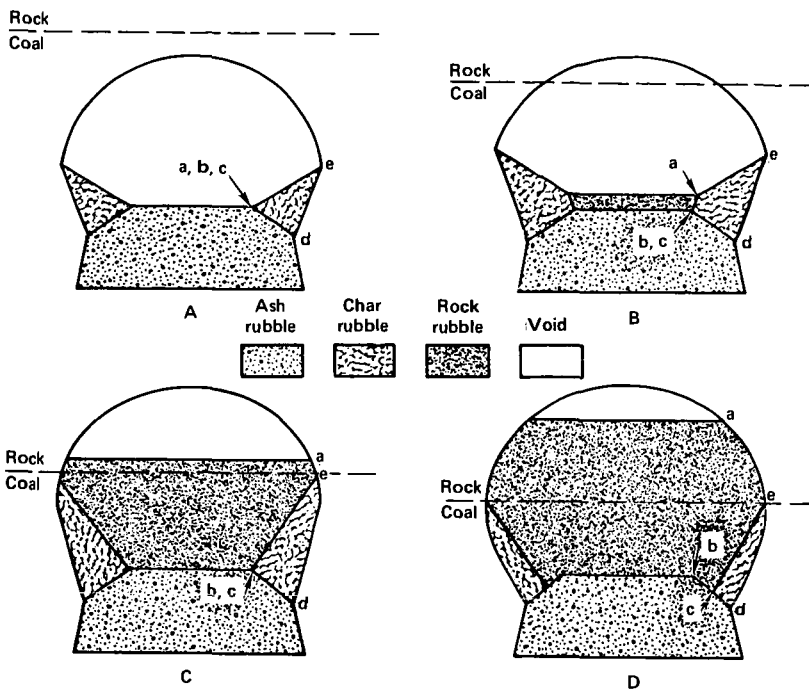


Figure 1 Generic cavity shapes constructed by the model.

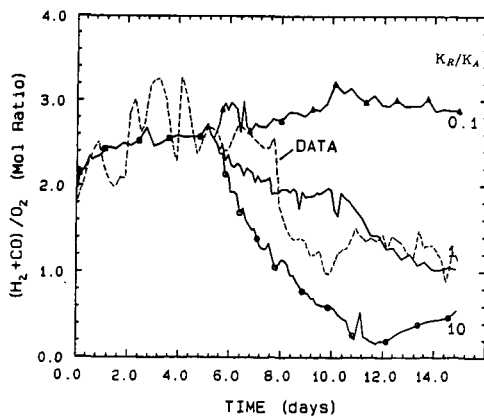


Figure 2 Effect of rock-to-ash rubble permeability ratio on the ratio of  $H_2 + CO$  produced to  $O_2$  injected. Conditions of Table 1A. Field data from PSC field test shown as dashed line



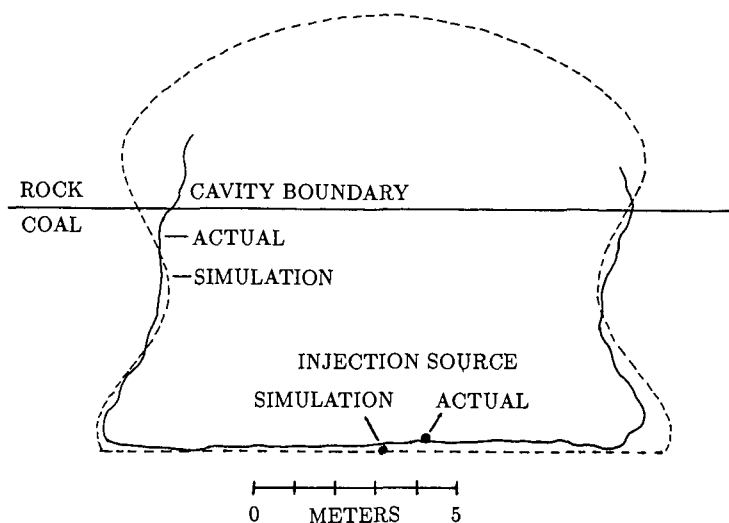


Figure 3 Comparison of actual and calculated cavity shapes in the plane perpendicular to the injection borehole at the injection point of the PSC CRIP cavity. Simulation used parameter values of Table 1A

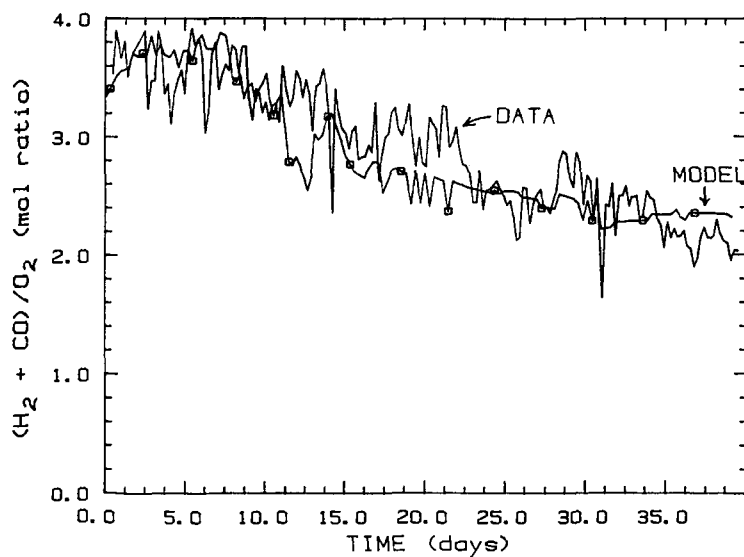


Figure 4 Ratio of  $H_2 + CO$  produced to oxygen injected calculated for the simulation of the RMI field test compared with actual data. Conditions of Table 1B.

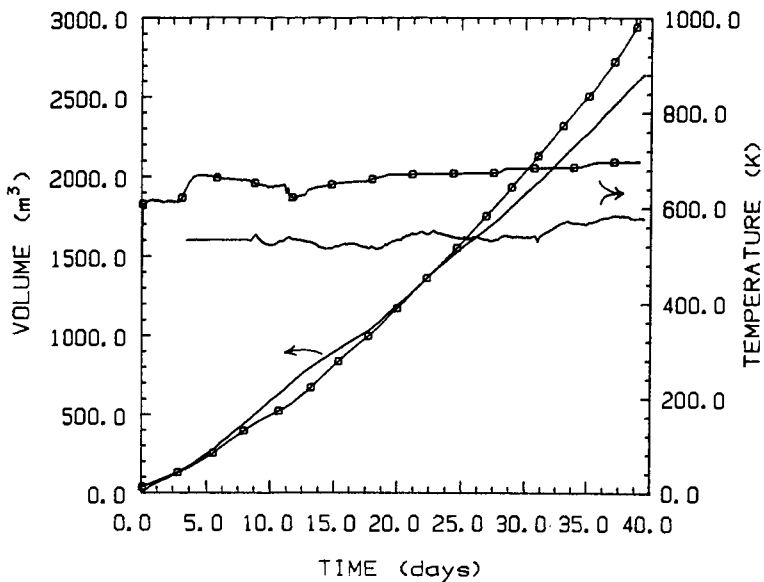


Figure 5 Cavity volumes and product gas temperature calculated by the model (marked lines), compared with material balance and temperature data from RMI CRIP side cavity.

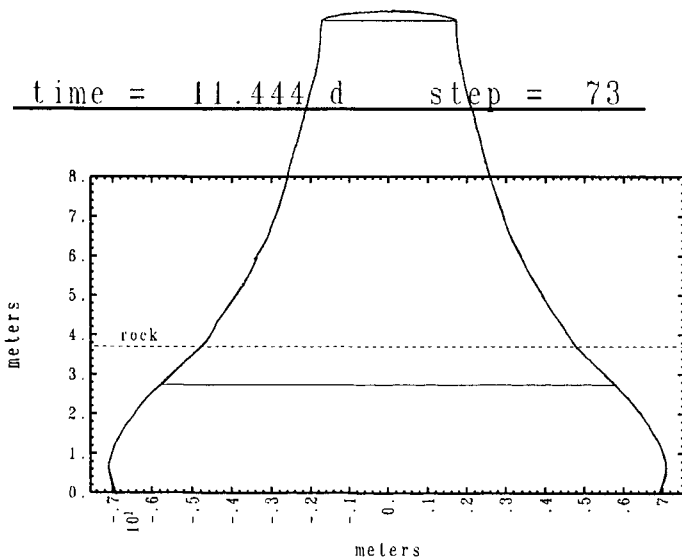


Figure 6 Cavity profile calculated at 11 days for simulation of the proposed UCG field test in Brazil. Simulation used parameter values given in Table IC.

## MODELING OF A HIGH-TEMPERATURE DIRECT COAL GASIFICATION PROCESS IN A TWO-STREAM REACTOR

K. Hanjalić and M. Sijerčić

University of Sarajevo-Energoinvest, Sarajevo, Yugoslavia

C. T. Crowe and S. Wojcicki

Washington State University, Pullman WA, 99164-2920

### ABSTRACT

A new scheme for direct gasification of pulverized coal has been analyzed by a mathematical model. Gasification occurs in the annular region of a cylindrical reactor during the cocurrent flow of a steam/coal mixture, with combustion products in the reactor core region serving as an internal heat source. The model incorporates the two equation model for turbulence, mass exchange between phases due to chemical reactions and radiative heat transfer. Detailed calculations are carried out to assess the feasibility of the scheme.

### INTRODUCTION

The basic concept for a two-stream gasifier for pulverized coal has been described in earlier publications (see reference 1). The basic configuration is shown in figure 1. Steam and coal are introduced on the periphery of the reactor while air and coal are injected as the core flow. It is assumed that the gasification will occur in the annular region of the cylindrical reactor during the cocurrent flow of a coal/steam mixture with hot combustion products in the reactor core region, the latter serving as the heat source. In this manner, the scheme capitalizes on two well known gasification concepts: direct supply of heat from internal combustion and hydrodynamic separation of gasification products from the combustion gases. The product gases, acceptably clean, are ducted away at the end of the reactor through an annular slot while the combustion gases from the core region are utilized for heat recovery in the system.

A global analysis of the system shows that the scheme is feasible provided that:

- a) sufficient radiative heat transfer occurs between the two streams in cocurrent flow to ensure the completion of the gasification process and,
- b) proper fluid dynamic conditions are achieved to avoid intensive mixing of the two streams in the reactor.

An experimental investigation of the process and the conditions which satisfy these requirements would require costly and extensive experimentation. We have chosen to develop a computer model as the first phase of a research program aimed at establishing the potential feasibility of the scheme and elucidating the important parameters in system design. If the scheme appears feasible, the results of the numerical model will be used to complement design of the experimental rig.

### MATHEMATICAL MODEL

The mathematical model of the gasification process entails solving the appropriate conservation equations for the gas and particle phases, as well as a number of auxiliary equations which describe various phenomena and interactions in the process. The model is based on the following assumptions:

- the process is adiabatic.
- the flow and temperature fields are axisymmetric.
- chemical reactions are first order reactions.
- thermal radiation is monochromatic and scattering due to the particles is isotropic.

The gas phase is described by a system of time-averaged conservation equations for momentum, mixture enthalpy and concentrations of chemical species. In addition the equation set contains conservation equations for the kinetic energy and dissipation rate of turbulence following the well known  $k - \epsilon$  model (2). The general form for the conservation equations is

$$\frac{\partial}{\partial x}(\rho U \phi) + \frac{1}{r} \frac{\partial}{\partial r}(\tau \rho V \phi) = \frac{\partial}{\partial x}(\Gamma_{\phi} \frac{\partial \phi}{\partial x}) + \frac{1}{r} \frac{\partial}{\partial r}(\tau \Gamma_{\phi} \frac{\partial \phi}{\partial r}) + S \quad (1)$$

where  $U$  and  $V$  are the axial and radial velocity components and the dependent variable  $\phi$  represents the density, velocity components, turbulence parameters, enthalpy and concentration of chemical species. The chemical composition of the gases is assumed to be nitrogen, oxygen, carbon dioxide, water vapor and gasification products (carbon monoxide and hydrogen). The transfer function  $\Gamma_{\phi}$  represents such quantities as effective viscosity, thermal conductivity and diffusion coefficients. The source term  $S$  incorporates such phenomena as production or depletion of chemical species due to chemical reaction and the mass, momentum and energy sources provided by the particle phase. The definition of these terms will not be included in the interest of brevity.

In order to evaluate thermal radiation exchange, the number density of the particles is needed. Equation 1 is utilized with the transfer function being the effective diffusion coefficient, as taken from Melville and Bray (3), and the source term being zero. The influence of the particulate phase on the effective viscosity of the gas is also modeled with a corrective factor based on the local mass concentration of the particles.

The thermal radiation is simulated with the "six-flux" model (4) with the assumption that the gas radiation is a volume phenomena and the particle radiation is a surface phenomena. It is also assumed that the radiation scattering by the particles is isotropic. Two diffusion-type equations are solved for the radiative heat flux in the axial and radial directions.

The particle velocities and temperatures are obtained by integrating the momentum and energy equations along trajectories for single particles. The effect of particle dispersion due to turbulence is accounted for by adding a "diffusive" velocity to the particle motion which is proportional to the concentration gradient and the effective diffusion coefficient (5). The particle energy equation relates the change in thermal energy of the particle to the convective and radiative heat transfer as well as the energy associated with the change of phase.

To simplify the gasification model, the coal is regarded as char. The mass rate of change of the coal particle is given by

$$\frac{dm_p}{dt} = \dot{r}_c + \dot{r}_g \quad (2)$$

where  $\dot{r}_c$  is the reaction rate for combustion and  $\dot{r}_g$  for gasification. It is assumed that chemical kinetic and diffusion processes occur in parallel so the reaction rates are given by

$$\dot{r}_g = m_p A_p \rho X_{H_2O} / \left[ m_{H_2O} \left( \frac{1}{K_g} + \frac{d_p}{ShD} \right) \right] \quad (3a)$$

$$\dot{r}_c = 1.5 m_p A_p \rho X_{O_2} / \left[ m_{O_2} \left( \frac{1}{K_c} + \frac{d_p}{ShD} \right) \right] \quad (3b)$$

where  $\rho$  is the gas density,  $A_p$  is the particle cross-sectional area,  $X_{O_2}$  and  $X_{H_2O}$  are the mass fractions of oxygen and water vapor,  $m$  is the molecular weight,  $Sh$  is the Sherwood number and  $d_p$  is the particle diameter. The chemical reaction rates are given in the form of Arrhenius expressions with coefficients determined experimentally for Yugoslav coals (6); namely,

$$K_g = 1.2 \times 10^6 \exp\left(-\frac{23077}{T}\right) \quad (4a)$$

$$K_c = 5.6 \times 10^4 \exp\left(-\frac{15035}{T}\right) \quad (4b)$$

It must be mentioned that these coefficients can vary by an order of magnitude or more depending on the literature source.

The phase coupling in the model is accomplished using the PSI cell scheme (7). Particles are released from a discrete number of radial locations to simulate an initially uniform particle number density. The number flow rate along each trajectory is constant. The change in particle mass, momentum and energy are recorded as each trajectory traverses a computational cell and these become the source terms in the gas-phase flow equations. The energy source term also includes the radiative heat transfer from the particles.

The boundary conditions for the gas phase follow the standard formulations used in conjunction with the  $k - \epsilon$  turbulence model (2). The gradient for the concentration of the chemical species is set equal to zero at the wall. Also the incident radiation at the wall is set equal to the wall radiation.

### MODEL PREDICTIONS

The verification of the computational model has been partially achieved through its application to simple flow fields for which data are available. Reasonably good agreement between model predictions and experimental results has been achieved for turbulent flows in a circular pipe (8) and a "cold" model of the gasification reactor (9). Verification of the model under realistic conditions for the reactor has yet to be established.

The model was applied to reactor geometry for which the lip separating the two streams was set at a radius ratio of 0.8. The initial velocity of the inner core flow was 6.4 m/s while a velocity of 3.87 m/s was selected for the annular flow. The initial temperature of the inner flow was 1300 K and that of the outer flow was 900 K.

The development of the axial velocity profile at progressive distances downstream is shown in figure 2. There is a rapid mixing initially and momentum diffuses into the low speed outer annular flow to increase the velocity. The temperature of the core stream increases rapidly with the combustion of the coal and there is a consequent acceleration of the flow to satisfy mass flow continuity because of the decreased gas density. Then radiative heat transfer to the outer stream cools down the core flow and heats the outer flow giving rise to velocity changes in each stream (decelerating the core flow and accelerating the annular flow) which drive them both toward velocity equilibrium.

The radial profiles for the gasification products,  $H_2$  and  $CO$ , at progressive downstream locations are shown in figure 3. One notes that the gasification products remain basically in the outer region of the reactor and could be separated by an annular slot shown schematically in figure 1. This prediction supports the feasibility of the concept.

The fraction of coal consumed in the gasification process is shown in figure 4. One notes that 60% of the coal at the outside of the reactor has been gasified at approximately five reactor radii from the inlet. Of course, the rate of coal consumption will depend strongly on the gasification rate for specific coals.

The predicted isotherms are shown in figure 5. One notes a very rapid temperature change at the reactor inlet due to combustion of the coal and the subsequent decrease in temperature as the heat is radiated from the hot core to the annular flow. The gas composition at three duct diameters downstream from the inlet is shown in figure 6. One notes, as also shown in figure 3, that the gasification products remain in the peripheral region while the combustion products are concentrated in the core. As shown in the figure, if the slot for the removal of the gasification products were located at a radius ratio of 0.7, the recovery would be primarily  $CO$  and  $H_2$  with some  $CO_2$  and water vapor. The relative fractions of chemical species in the slot would be

$$CO + H_2 = 0.54$$

$$CO_2 = 0.16$$

$$H_2O = 0.05$$

$$N_2 = 0.25$$

Of course, the fraction of gasification products to combustion products can be increased by increasing the radius ratio of the slot. However the yield of the gasification products would be reduced. The optimum design remains to be established.

### CONCLUSION

Based on the predictions of the mathematical model, the proposed gasification concept appears feasible. The scheme is attractive because of the direct contact heat exchange and the separation of combustion and gasification products. The ultimate assessment of the scheme will only be possible through well-designed pilot plant tests in which the operational conditions and configurations are changed to achieve an optimum design. The numerical model developed here will be a useful tool to complement the design and operational adjustments of an actual system.

### ACKNOWLEDGEMENTS

The authors acknowledge the support of Dr. Soliman of the International Programs Office of the US Department of Energy.

### REFERENCES

1. Hanjalić, K., Sijerčić, M., Crowe, C.T. and Wojcicki, S. (1985) Analysis of a Two-Stream Coal Gasification System, Spring Meeting, The Combustion Institute, San Antonio, TX.
2. Launder, B.E. and Spalding, B.D. (1972) *Mathematical Models of Turbulence*, Academic Press, London.
3. Melville, W.K. and Bray, K.N.C. (1979) The Two Phase Turbulent Jet, *Int. Jnl. Heat and Mass Trans.*, 22, 279.
4. Chu, C-M and Churchill, S.W. (1955) Numerical Solution of Problems in Multiple Scattering of Electromagnetic Radiation, *Jnl. Phys. Chem.* 59, 855.
5. Smoot, L.D. and Pratt, D.T. (ed.) (1979) *Pulverized Coal Combustion and Gasification*, Plenum Press, New York.
6. Karč, H. (1986) Isledovanie gazifikaciji i szigania burogo uglja "Zenica", *Politechnika Wroclawska*.
7. Crowe, C.T., Sharma, M.P. and Stock, D.E. (1977) The Particle-Source-in-Cell (PSI-Cell) Model for Gas-Droplet Flows, *Jnl. of Fluids Engr.* 99, 2, 325.
8. Laws, E.M., Lim, E.H. and Livesey, J.L. (1974) Turbulent Pipe Flows in Development and Decay, 2nd Symposium on Turbulent Shear Flows, London
9. Krajišnik, S., Žerajić, D. and Sijerčić, M. (1982) Eksperimentalno izucavanje procesa strujanja u reaktoru za direktnu gasifikaciju uglja, *Energoinvest -ITEN*.

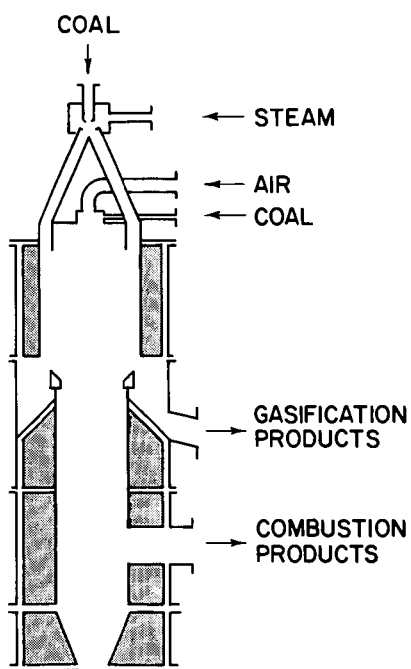


Figure 1. Schematic Diagram of Gasification Reactor.

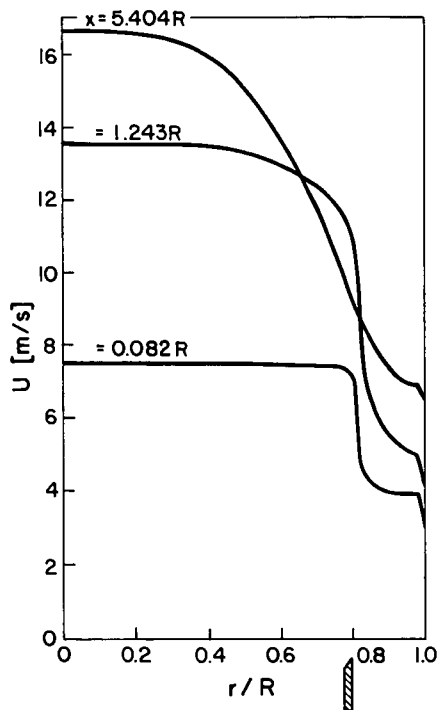


Figure 2. Development of axial velocity profile along reactor.

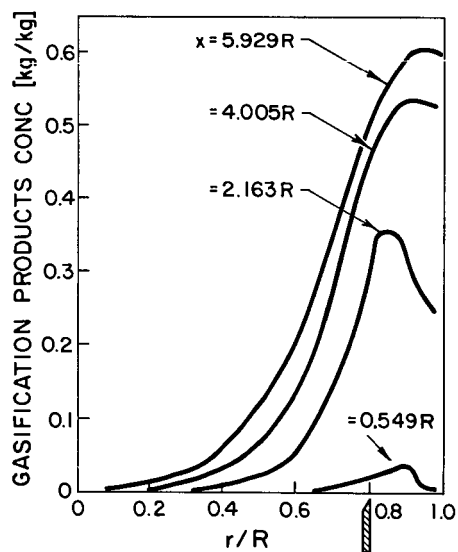


Figure 3. Development of concentration profiles for gasification products along reactor.

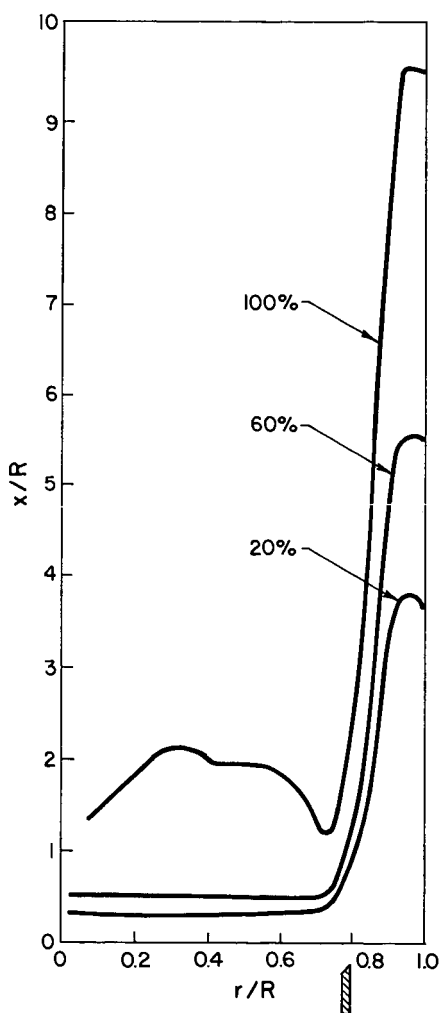


Figure 4. Fraction of coal particle consumption along reactor.



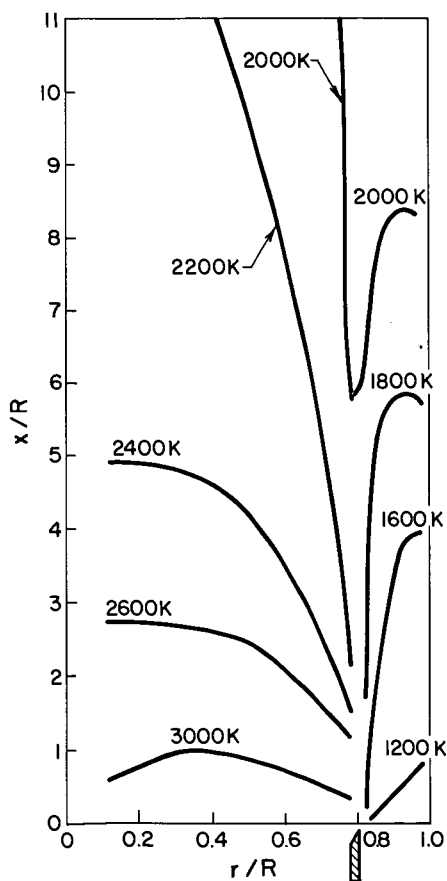


Figure 5. Isothermal profiles in reactor.

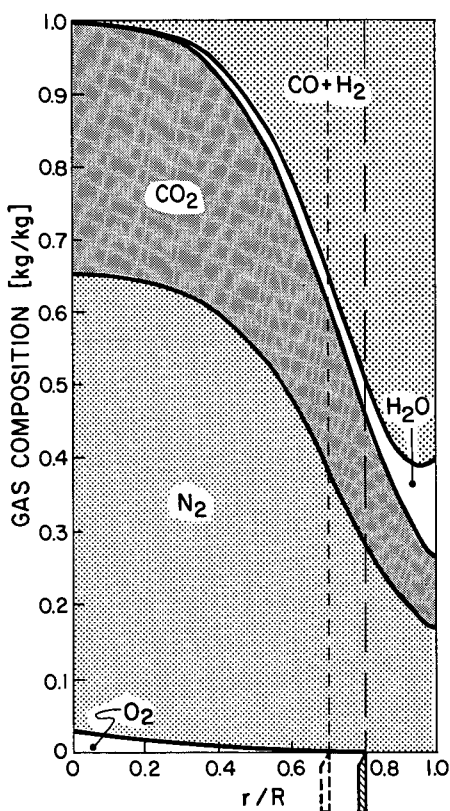


Figure 6. Radial gas phase composition at three duct diameters from inlet.

## PERFORMANCE SIMULATION OF FLUIDIZED-BED COAL COMBUSTORS

Ravi R. Chandran and Denny D. Sutherland

The Babcock & Wilcox Company, R&D Division, Alliance, Ohio 44601

### ABSTRACT

*A code, referred to as FBFSIM, is being developed to predict large-scale atmospheric fluidized-bed combustor (AFBC) performance with fundamental fuel data from bench-scale test units as input. This work is carried out as a part of AFBC fuels characterization program sponsored by the Electric Power Research Institute (EPRI). The code accounts for the physics of fluidization, which is unit specific, and the chemistry of combustion, which is fuel specific. The code includes a 3-D model and modules on bed hydrodynamics, chemical kinetics, solid distribution, and transport phenomena. The model for in-bed combustion incorporates a two-region particle mixing formulation. The code for in-bed combustion has been validated for different AFBC unit sizes (0.1, 2, and 20 MW) and different coals (two bituminous and a lignite). Sensitivity analyses have been carried out to identify the controlling variables and guide experimental work. Computer simulations have also been performed to delineate system response to operational parameters.*

### INTRODUCTION

Test results from small-scale to pilot plant AFBC units have proven the viability of fluidized-bed combustion technology for large-scale applications. However, commercialization of this technology has been slow due in part to concerns regarding scale-up for unit size and fuel type. To overcome this hurdle, Babcock & Wilcox (B&W) under the sponsorship of EPRI has developed an AFBC fuels characterization method (1)(2). The approach involves the generation of fundamental fuel data using inexpensive bench-scale tests and the development of a mathematical model or performance code to link bench-scale results to large-scale operation. The objectives are to 1) facilitate the optimal design of commercial-size AFBC units, and 2) quantify the fuel flexibility of existing AFBC designs. For a review of the models reported in the literature along with the rationale for the present model, the reader is referred to an earlier publication (3).

### FORMULATION

The performance code (FBFSIM) under development for bubbling-bed combustion comprises a model and four modules, and has been set up in this fashion so that it is easily adaptable to circulating as well as pressurized FBC. The first module evaluates hydrodynamics, which is unit specific. It accounts for fluidization regime, gas flow, bubble dynamics, and solids mixing characteristics. The second module deals with chemical kinetics (devolatilization, char combustion, and sorbent sulfation), which is influenced by coal and sorbent properties. The third module accounts for solids distribution in bed and above bed due to swelling, fragmentation, attrition, elutriation, and entrainment. The fourth module deals with transport phenomena such as interphase heat and mass transfer. For a given coal and specified operating conditions, the code seeks to predict overall combustion and sulfur capture efficiencies and combustion split and sulfur capture split between in-bed and freeboard. The first goal of this code development was to model in-bed combustion for the underbed-feed mode of operation. Additional goals are to model freeboard combustion, overbed-feed mode, and sulfur capture. The in-bed combustion model is described here.

#### Model for In-Bed Combustion

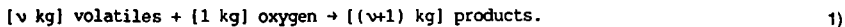
The in-bed combustion model currently addresses underbed feed with zero recycle. Future modifications will account for recycle. Figure 1 shows an idealization of the combustion sequence, and Figure 2 shows the corresponding conceptual model. The figures depict a unit cell defined as the bed cross section served by one feedpoint. Primary air enters the bed through a distributor plate, while coal particles of a broad size distribution (typically 6.35 mm x 0, or 1/4 inch x 0) and transport air enter through the feedpoint. Based on a review of the pertinent physical and chemical time scales, it is suggested that these coal particles entering the bed be classified in a binary fashion for modeling volatile release and heterogeneous combustion. Material below the maximum elutriable size for the given operating conditions is termed "fines" and the larger size fraction is denoted as "coarse". For example, at typical AFBC operating conditions, the fines would correspond to material passing through 30 sieve (590 microns).

The solids injected through the feedpoint flow up through the bed and diffuse laterally. The fines are considered to be in plug flow. They heat up, devolatilize, and burn while convecting axially and dispersing radially until they reach the bed surface and elutriate. The coarse particles also heat up and devolatilize as they mix above the feedpoint. If the coal contains a significant proportion of volatiles, a volatile-rich zone above the feedpoint could result. The volatiles released would rise as a plume and burn in a gaseous diffusion flame with the surrounding oxygen. Whether this plume closes within the bed or not would depend on the coal's ratio of volatile to fixed carbon, feedpoint spacing, and the bed operating conditions. Some coarse particles could fragment during devolatilization if their size exceeds the critical stable size for fragmentation. The coarse char particles mix in the bed, generate flakes and fines due to combustion-enhanced mechanical attrition (CEMA), and combust in the oxidizing zone outside the plume until they reach the elutriable size. The flakes and fines resulting from CEMA are subject to the competing processes of combustion in the bed and elutriation to the freeboard. Therefore, feedpoint spacing has different implications for different coal ranks with regard to in-bed combustion. For low volatile coals or other solid fuels, the wider the feedpoint spacing, the lower the combustion of fines in the feed due to high concentration of fuel and low concentration of oxygen above the feedpoint. For high volatile coals, the occurrence of a volatile-rich plume additionally could diminish in-bed combustion. A video of the bed surface taken recently during 0.1 MW AFBC operation supports the conceptual model discussed above.

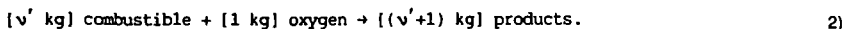
To model in-bed combustion, it is necessary to properly account for the combustion of volatiles, devolatilized fines in the feed, and coarse char particles. These three components burn in a coupled fashion and the degree of combustion is governed by fluidization physics and fuel chemistry. The underlying physical and chemical processes are complex and not fully understood. Therefore, some simplifying assumptions have been introduced (3). Consequently, combustion is visualized to occur in two regions. The first region is where the physical processes of convection and dispersion of coal particles are important. This region lies directly above the feedpoint and provides the setting for coal particle heat up, volatile release, volatile combustion, and the combustion of fines in the feed. Although swelling and fragmentation could occur in this region, they do not involve an oxidation step and need not be considered here. The second region includes the whole unit cell, where the coarse char particles are uniformly distributed and undergo heterogeneous combustion in the oxidizing zone outside the plume. The unit cell coordinate geometry for the 3-D formulation is shown in Figure 3.

Considerable attrition occurs in underbed feed systems (1)(2). A distributed fracture model along with an experimentally determined coal-specific attrition parameter are used to estimate the coal particle size distribution  $F_i(\bar{d}_i)$  entering the bed.

**Region I.** The formulation here corresponds to an adaptation of the model of Bywater (4). Five conservation equations are used to designate the problem. These are for the concentration of i) volatiles remaining in the coarse coal particles ( $C_{VC}$ ), ii) volatiles remaining in the fines ( $C_{VF}$ ), iii) solid combustibles in the devolatilized fines ( $C_{CF}$ ), iv) gaseous volatiles ( $C_G$ ), and v) oxygen ( $C_O$ ). The gaseous volatiles are assumed to combust according to the stoichiometric reaction,



Also the fast reaction or large Damkohler limit is presumed to apply. The heterogeneous combustion of devolatilized fines is considered to follow the reaction,



The reaction order in oxygen is taken to be 0.6 based on the work of Daw (5). Finally, the classical treatment of Burke and Schumann (6) is applied to the combustion of gaseous volatiles. This facilitates the description of a new variable,

$$C_{Go} = C_G - vC_O, \quad (3)$$

and reduces the number of variables (and equations) by one.

The mass balance equations are normalized by defining the following variables:

$$x^* = \frac{x}{x_b}, y^* = \frac{y}{y_b}, z^* = \frac{z}{H}, x_f^* = \frac{x_f}{x_b}, x_o^* = \frac{x_o}{x_b}, y_f^* = \frac{y_f}{y_b}, y_o^* = \frac{y_o}{y_b},$$

$$C_{vc}^* = \frac{C_{vc}}{C_{vci}}, C_{vf}^* = \frac{C_{vf}}{C_{vfi}}, C_{cf}^* = \frac{C_{cf}}{C_{cfi}}, C_{go}^* = \frac{C_{go}}{C_{goi}}$$

where subscript i denotes the parameter value at feedpoint or distributor,  $x_b$  and  $y_b$  are the length and width of the unit cell, and  $H$  is the bed plus splash zone height.

The governing equations in dimensionless form are:

$$\frac{\partial C_{vc}^*}{\partial z^*} = \alpha_x \frac{\partial^2 C_{vc}^*}{\partial x^{*2}} + \alpha_y \frac{\partial^2 C_{vc}^*}{\partial y^{*2}} - k_{vc}^* C_{vc}^* J_c, \quad 4)$$

$$\frac{\partial C_{vf}^*}{\partial z^*} = \beta_x \frac{\partial^2 C_{vf}^*}{\partial x^{*2}} + \beta_y \frac{\partial^2 C_{vf}^*}{\partial y^{*2}} - k_{vf}^* C_{vf}^* J_f, \quad 5)$$

$$\frac{\partial C_{cf}^*}{\partial z^*} = \beta_x \frac{\partial^2 C_{cf}^*}{\partial x^{*2}} + \beta_y \frac{\partial^2 C_{cf}^*}{\partial y^{*2}} - k_{cf}^* C_{cf}^* (-C_{go}^*)^{0.6} LI, \text{ and} \quad 6)$$

$$\begin{aligned} \frac{\partial C_{go}^*}{\partial z^*} = & \gamma_x \frac{\partial^2 C_{go}^*}{\partial x^{*2}} + \gamma_y \frac{\partial^2 C_{go}^*}{\partial y^{*2}} + \frac{k_{cf}^* C_{cf}^* (-C_{go}^*)^{0.6} LI \psi R_{fi}}{v} \\ & + k_{vc}^* C_{vc}^* J_c \phi + k_{vf}^* C_{vf}^* J_f \psi - k_{oc}^* C_{go}^* I, \end{aligned} \quad 7)$$

where

$$J_c = \begin{cases} 0 & \text{if } (z^* H' / u_{sc} - \tau_c) \leq 0 \\ 1 & \text{if } (z^* H' / u_{sc} - \tau_c) > 0 \end{cases} \quad J_f = \begin{cases} 0 & \text{if } (z^* H' / u_{sf} - \tau_f) \leq 0 \\ 1 & \text{if } (z^* H' / u_{sf} - \tau_f) > 0 \end{cases}$$

$$L = \begin{cases} 0 & \text{if } C_{vf}^* > 0 \\ 1 & \text{if } C_{vf}^* = 0, \end{cases} \quad I = \begin{cases} 0 & \text{if } C_{go}^* \geq 0 \\ 1 & \text{if } C_{go}^* < 0 \end{cases}$$

Subject to the boundary conditions:

$$\text{at } z^* = 0: \left. \begin{aligned} C_{vc}^*(x^*, y^*, 0) \\ C_{vf}^*(x^*, y^*, 0) \\ C_{cf}^*(x^*, y^*, 0) \\ C_{go}^*(x^*, y^*, 0) \end{aligned} \right\} = \begin{cases} 1 & \text{for } x_f^* - \frac{x_o^*}{2} \leq x^* \leq x_f^* + \frac{x_o^*}{2}, y_f^* - \frac{y_o^*}{2} \leq y^* \leq y_f^* + \frac{y_o^*}{2} \\ 0 & \text{for } 0 \leq x^* < x_f^* - \frac{x_o^*}{2}, x_f^* + \frac{x_o^*}{2} < x^* \leq 1, \\ & 0 \leq y^* < y_f^* - \frac{y_o^*}{2}, y_f^* + \frac{y_o^*}{2} < y^* \leq 1 \\ -1 & \text{for } 0 < x^* \leq 1, 0 < y^* \leq 1 \end{cases}$$

$$\text{for } z^* > 1: \quad \frac{\partial C_{vc}^*}{\partial x^*}, \frac{\partial C_{vf}^*}{\partial x^*}, \frac{\partial C_{cf}^*}{\partial x^*}, \frac{\partial C_{go}^*}{\partial x^*} = 0 \text{ at } x^* = 0, 1$$

$$\frac{\partial C_{vc}^*}{\partial y^*}, \frac{\partial C_{vf}^*}{\partial y^*}, \frac{\partial C_{cf}^*}{\partial y^*}, \frac{\partial C_{go}^*}{\partial y^*} = 0 \text{ at } y^* = 0, 1$$

$\alpha$ ,  $\beta$  and  $\eta$  are dimensionless dispersion coefficients,  $k_{vc}^*$  and  $k_{vf}^*$  are normalized devolatilization rate constants,  $k_{cf}^*$  is a non-dimensional rate constant for oxidation of combustibles in devolatilized fines,  $\phi$  and  $\psi$  are dimensionless solid to gas flux transfer parameters,  $R_{fi}$  is the ratio of  $C_{cfi}$  and  $C_{vfi}$  at the feedpoint, and  $k_{oc}^*$  is a normalized reaction rate constant for the depletion of oxygen in the bed due to coarse char particle combustion.

The parameter  $J$  accounts for the effect of finite heating rate and the consequent delay in the onset of volatile evolution. It activates the volatile generation term when the particles have convected a distance that corresponds to the heatup time  $\tau$ .  $L$  and  $I$  are off/on switching parameters for the heterogeneous combustion of devolatilized fines and coarse char particles respectively. Equations 6 and 7 are coupled through the fines heterogeneous combustion term and hence need to be solved simultaneously. Finally, the last term in equation 7 requires a trial and error procedure to match the coarse char particle combustion occurring in Region II.

**Region II.** The objective here is to determine the rates of oxygen consumption and elutriation due to the heterogeneous combustion of coarse char particles. This can be accomplished by carrying out solids population balances of the type proposed by Levenspiel, et al. (7)(8).

The flow rates pertaining to the different steps of the combustion sequence are shown in Figure 4. Sorbent and ash particles are assumed to be inert for this analysis. Coarse coal particles represented by  $(n-m)$  cut sizes undergo devolatilization. The inflow rate of cut  $i$  with mean diameter  $\bar{d}_i$  is denoted as  $F_i(\bar{d}_i)$ . To simplify the analysis, swelling is decoupled from devolatilization. A differential mass balance for the devolatilization step yields:

$$F_w(\bar{d}_i) = (1 - v_i) F_i(\bar{d}_i) \text{ for } i = m+1, m+2, \dots, n, \quad (8)$$

where  $v_i$  is the gaseous volatile yield fraction for the  $i$ th cut.

Size as well as density change during swelling. Therefore, a number balance rather than a mass balance is indicated. The number flow rate before swelling is related to the mass flow rate according to:

$$N_w(\bar{d}_i) = F_w(\bar{d}_i) / (\rho_{wi} \bar{d}_i^3/6) \quad (9)$$

with  $\rho_{wi} = \rho_{coal}(1 - v_i)$  and  $\rho_{coal}$  is coal density.

From a steady state number balance, the number flow rate after swelling is:

$$N_f(\bar{d}_i) = N_w(\bar{d}_{i-1}) (SI_{i-1} - 1) \frac{\bar{d}_{i-1}}{\bar{d}_i - \bar{d}_{i-1}} + N_w(\bar{d}_i) \left[ 1 - (SI_i - 1) \frac{\bar{d}_i}{\bar{d}_{i+1} - \bar{d}_i} \right] \quad (10)$$

for  $i = m+1, m+2, \dots, n$ ,

with  $N_w(\bar{d}_m) = 0$ .  $SI_i$  is the swelling index for the  $i$ th cut size.

The corresponding mass flow rate is:

$$F_f(\bar{d}_i) = N_f(\bar{d}_i) \rho_{fi} (\bar{d}_i^3/6) \text{ for } i = m+1, m+2, \dots, n, \quad (11)$$

where  $\rho_{fi} = \rho_{wi} / S i_i^3$ .

For typical underbed feed sizes (6.35 mm x 0, or 1/4 inch x 0, experimental data indicates fragmentation to be negligible, therefore,

$$F_c(\bar{d}_i) = F_f(\bar{d}_i) \text{ for } i = m+1, m+2, \dots, n, \quad (12)$$

and

$$\rho_{ci} = \rho_{fi}.$$

The model for char combustion would depend upon coal properties and is likely to correspond to either shrinking size or shrinking core kinetics. Bench-scale experimental data suggest that a shrinking particle model would be a reasonable approximation for bituminous coals. A solids population balance carried out with the modification suggested by Overturf and Kayihan (9) for discrete cut sizes gives:

$$W_c(\bar{d}_i) = \frac{[F_c(\bar{d}_i) - F_{bd}(\bar{d}_i)] \Delta d_i + W_c(\bar{d}_{i+1}) S_c(\bar{d}_{i+1}) \Delta d_i / \Delta d_{i+1}}{S_c(\bar{d}_i) + E_c(\bar{d}_i) \Delta d_i + 3 S_c(\bar{d}_i) \Delta d_i / \bar{d}_i} \quad (13)$$

for  $i = n, n-1, \dots, (m+1), m$ ,

with  $W_c(\bar{d}_{n+1}) = 0$  and  $F_c(\bar{d}_m) = 0$ .  $W_c(\bar{d}_i)$  is weight of char particles of size  $\bar{d}_i$  in bed and  $\Delta d_i$  is size interval for  $i$ th cut. Tests in the 1-x 1-foot (1 x 1) and 6-x 6-foot (6 x 6) AFBC units at B&W indicate that the char content of the bed drain solids is very small, therefore,

$$F_{bd}(\bar{d}_i) = 0 \text{ for } i = n, n-1, \dots, (m+1), m. \quad (14)$$

$E_c(\bar{d}_i)$  denotes entrainment rate constant of char particles of size  $\bar{d}_i$  from the bed surface. The overall shrinkage rate  $S_c(\bar{d}_i)$  is expressed as the sum of the shrinkage rates due to combustion and attrition (10)(11):

$$S_c(\bar{d}_i) = S_{cc}(\bar{d}_i) + S_{ca}(\bar{d}_i). \quad (15)$$

Attrition rate here corresponds to the flakes and fines generated in the CEMA tests. The shrinkage rate for char combustion according to a first order reaction is:

$$S_{cc}(\bar{d}_i) = - \left. \frac{d\bar{d}_i}{dt} \right|_{cc} = \frac{2 \bar{C}_{ob}}{\rho_{ci} f_{cci} \left[ \frac{1}{\lambda_i R_{mc}} + \frac{1}{R_{cc}} \right]} \quad (16)$$

where  $\bar{C}_{ob}$  is the mean oxygen concentration in the bed,  $f_{cci}$  is the weight fraction of equivalent carbon in char,  $R_{mc}$  is the external mass transfer coefficient, and  $R_{cc}$  is the chemical rate coefficient for char combustion.  $\lambda_i$  is a parameter that depends on stoichiometry and has a value between 3/8 for  $C + O_2 \rightarrow CO_2$  reaction at the char surface and 3/4 for  $C + 1/2 O_2 \rightarrow CO$  reaction.

The shrinkage rate due to attrition  $S_{ca}(\bar{d}_i)$  is:

$$S_{ca}(\bar{d}_i) = k_{ca}(u_o - u_{mf}) / (3 f_{cci}), \quad (17)$$

where  $k_{ca}$  is CEMA rate constant for carbon,  $u_o$  is superficial gas velocity, and  $u_{mf}$  is the superficial gas velocity at minimum fluidization.

The flakes and fines generated due to CEMA seem to follow the Rosin-Rammler distribution. If  $q_{fi}$  and  $q_{ni}$  are the weight fraction of flakes and fines of size  $\bar{d}_i$ , and  $f_{fi}$  is the proportion of flakes in the attrited material, then the weight of char particles of size  $\bar{d}_i$  by mass balance is:

$$w_c(\bar{d}_j) = \frac{\sum_{i=m}^n w_c(\bar{d}_i) s_{ca}(\bar{d}_i) (q_{1j} f_{f1} + q_{nj} (1-f_{f1})) \frac{\Delta d_j}{\Delta d_i} + w_c(\bar{d}_{j+1}) s_{cc}(\bar{d}_{j+1}) \frac{\Delta d_j}{\Delta d_{j+1}}}{s_{cc}(\bar{d}_j) + E_c(\bar{d}_j) \Delta d_j + 3 s_{cc}(\bar{d}_j) \Delta d_j / \bar{d}_j} \quad (18)$$

for  $j = m-1, m-2, \dots, 1$ .

The shrinkage rate  $S_{cc}$  depends upon  $\bar{C}_{ob}$ , the mean oxygen concentration in the bed which is not known a priori. So the procedure is to start with a guess value of  $\bar{C}_{ob}$  and iterate in conjunction with Region I model until convergence. The flow chart for the computer code is given in Figure 5. Subroutines are listed within quotation marks. "FSATT" accounts for feed system attrition, "HYDRO" for bed hydrodynamics, "SOLDIS" for solids distribution, and "CHEMK" for chemical kinetics. "TRANSP" provides interphase heat and mass transfer coefficients and "TEMP" evaluates burning char particle temperature by energy balance. The code is written in FORTRAN and makes use of ACM Algorithm #565, PDETWO/PSETM/GEARB, for solving partial differential equations. Run times for in-bed performance simulations typically range from 2-6 CPU minutes on a DEC VAX 11/785.

To conserve space, the ensuing discussion will be qualitative and will not include equations. From the bed char weight distributions determined above, the rate of oxygen consumption due to char combustion ( $w_{occl}$ ), char elutriation rate from the bed and the conversion of char in the bed ( $X_c$ ) are evaluated. It is assumed that any volatiles remaining in the coarse coal particles when they reach the bed surface (based on the solution of Equation 4) are released uniformly in the bed. The oxygen consumption rate due to this component is added to  $w_{occl}$  to calculate the overall rate of oxygen consumption in Region II ( $w_{ocII}$ ).

By integrating the bed-surface concentrations computed in Region I, the fraction of the volatiles released in-bed from the fines ( $X_{vf}$ ), the conversion of gaseous volatiles in-bed ( $X_v$ ), and the conversion in the bed of combustibles in devolatilized fines ( $X_{cf}$ ) are determined. Also, the oxygen consumption rate in Region I ( $w_{ocI}$ ) is calculated by mass balance. The parameter  $k_{oc}^*$  is adjusted until  $w_{oc}$  values converge. Then the iteration for  $\bar{C}_{ob}$  is performed until convergence. From the converged values for  $X_v$ ,  $X_{cf}$ , and  $X_c$ , the total in-bed carbon conversion ( $X_{ic}$ ) and in turn the in-bed combustion efficiency ( $E_{ic}$ ) are computed.

Typical parameters for which the performance code requires input and their origin are indicated in Table 1.

## VALIDATION

The objective is to validate the performance code for different AFBC unit sizes and fuel types. The code predictions for in-bed combustion of Kentucky No. 9 coal are compared with experimental data from 1 x 1 [B&W], 6 x 6 [EPRI/B&W], and 20 MW<sub>e</sub> [TVA/EPRI] AFBC units in Figure 6. The data correspond to a gas residence time of about 0.5 second based on superficial velocity. Good agreement is observed. The in-bed combustion efficiency tends to decrease with an increase in feedpoint spacing but does not exhibit a smooth variation. The relatively high value obtained in the case of the 1 x 1 unit is due to lower gas velocity and lesser feed system attrition.

Figure 7 presents the results for Texas lignite. The square symbol stands for experimentally determined in-bed combustion efficiency and the solid line represents the code predictions. Experimental values of the overall combustion efficiency are also plotted for comparison. Predicted in-bed combustion and experimental overall combustion efficiency curves diverge with an increase in superficial gas velocity. This implies increased freeboard combustion at higher gas velocities. This is to be expected in view of the greater freeboard solids loading caused by CEMA, elutriation, and carry over of fines in the feed. Additional comparisons for Kentucky No. 9 and Pittsburgh No. 8 bituminous coals have been presented in a previous paper (3).

## SENSITIVITY ANALYSIS

An analysis for sensitivity over the range of parameter uncertainty is desirable to further evaluate the code, identify the controlling parameters, and guide experimental work. The parameters which have significant impact on code predictions are anticipated to differ with AFBC unit size, design, and coal type. Therefore, a number of test analyses are required to generalize the results. Based on initial studies, the sensitivity of different parameters for burning Kentucky No. 9 coal in two different AFBC units (1 x 1/0.1 MW and 18 x 12/ 20 MW<sub>e</sub>) are given in Table 2. Volatile conversion in-bed is typically complete (~100%) in the 1 x 1 AFBC unit and there-

fore its performance is primarily sensitive to char conversion parameters. VYULT impacts char fraction and hence is important. Due to the large feedpoint spacing in the 20 MW<sub>g</sub> pilot plant, the parameter COFDO assumes a lead role. It is difficult to combust fines in a short residence time and consequently DHOP exerts a considerable influence on performance of both units.

## SIMULATION

The response of the 20 MW<sub>g</sub> pilot plant to changes in the fines content of the feed and feed system attrition coefficient are shown in Figure 8. COFATT of 11.0 corresponds to the extent of attrition that occurs in the current design. Clearly, it is beneficial to control the amount of fines in the feed and reduce feed system attrition. Results of additional simulations pertaining to the operation of the unit will be presented in another paper (12).

## CONCLUSIONS

A phenomenological code for predicting in-bed combustion performance of AFBC units has been developed and validated. It provides a measure of required in-bed heat transfer surface allocation. Work is in progress to develop a freeboard combustion model. Future goals are to incorporate the effect of recycle and model overbed-feed mode and sulfur capture. The code is being tested and refined constantly based on new information and data. Upon completion, FBOSIM will become a versatile tool for performance simulation and design of fluidized-bed coal combustors.

## ACKNOWLEDGMENT

This work was performed with the support of EPRI. We are thankful to N. Soltys and L. A. Oberjohn of B&W for their help in conducting the sensitivity analysis.

## REFERENCES

1. Chandran, R.R., Duqum, J.N., Perna, M.A., Jafari, H.C., Rowley, D.R., Petrill, E.M., and Hansen, W.A., "A New Method for AFBC Fuels Characterization", 1987 International Conference on Fluidized Bed Combustion, The American society of Mechanical Engineers, p. 292, 1987.
2. Chandran, R.R., Duqum, J.N., and Modrak, T.M., "Coal Classification for Fluidized Bed Combustion", International Symposium on Coal Combustion, Beijing, China, Sept. 1987 (to be published by Hemisphere Publ. Corp.)
3. Chandran, R.R., Duqum, J.N., and Petrill, E.M., "A Performance Code for AFBC Scaleup - Part I: In-Bed Combustion", 1987 International Conference on Fluidized Bed Combustion, The American Society of Mechanical Engineers, p. 300, 1987.
4. Bywater, R.J., "The Effects of Devolatilization Kinetics on the Injector Region of Fluidized Beds," 6th International Conference on FBC, Atlanta, GA, Conf. 800428, Vol. III, p. 1092, 1980.
5. Daw, C.S., "Tubular Flow Reactor Experiment - Task 13", Oak Ridge National Laboratory, Oak Ridge, TN, July 1985.
6. Burke, S.P. and Schumann, T.W.E., Ind. Eng. Chem., Vol 20, p. 998, 1928.
7. Levenspiel, O., Kunii, D., and Fitzgerald, T., Powder Technology, Vol. 2, p. 87, 1968/69.
8. Kunii, D. and Levenspiel, O., Fluidization Engineering, John Wiley & sons, Inc., New York, NY, 1969.
9. Overturf, B.W. and Kayihan, F., "Computations for Discrete Cut Particle Size Distributions in a Fluidized Bed Reactor", Powder Technology, Vol 23, p. 143, 1979.
10. D'Amore, M., Donsi, G., and Massimilla, L., "Bed Carbon Loading and Particle Size Distribution in Fluidized Combustion of Fuels of Various Reactivity," 6th International Conference on FBC, Atlanta, GA, Conf-800428, Vol. I, p. 675, 1980.



11. Beer, J.M., Massimilla, L., and Sarofim, A.F., Inst. Energy Symposium Series 4: Fluidized Combustion, Systems and Applications, p. IV.5.1, 1980.
12. Divilio, R. J., Towers, T.A., and Chandran, R.R., "Applications of FBCBAL and B&W Combustion Model to the EPRI AFBC Demonstration Programs", 1988 EPRI Seminar, Palo Alto, CA, May 3-5, 1988 (to be presented).

---



---

**TABLE 1. PERFORMANCE CODE INPUT DATA**

<u>Model Input Parameter</u>	<u>Description</u>	<u>Source</u>
Unit cell cross section	Operating conditions	Validation test conditions or design specifications
Feedpoint location		
Bed temperature		
Coal feed rate		
Bed height		
Transport air		
Primary air		
Bed material density		
Bed weight		
Freeboard cross section		
Bed material size distribution		
Coal size distribution at the hopper		
Coal composition	Coal properties	ASTM procedures
Coal density		
Higher heating value		
Coal attrition parameters	FSATT subroutine	Feed System attrition tests
Gas dispersion coefficient	Hydrodynamics module	Literature
Solids velocity		
Solids dispersion coefficient		
Entrainment rate coefficient		
Coal particle heatup time	Chemical kinetics module	Fixed bed reactor
Volatile yield		
Devolatilization rate constant		
Volatile composition		
Char fraction		
Char reactivity		
Char composition		
Swelling index	Chemical kinetics module	Bench-scale AFBC unit
Fragmentation index		
CEMA rate constant	Solids distribution module	Bench-scale AFBC unit
Weight fraction of flakes		

TABLE 2. SENSITIVITY ANALYSIS

Parameter	Type	Description	Sensitivity		
			1 x 1 B&W	20 MW <sub>0</sub> TVA	
DBED	Operational	Bed material mean size	Negl	Negl	
DHOP	Operational	Coal feed size distribution	High	High	
COFATT	Unit/Fuel	Feed system attrition coeff	Medium	High	
ATTEXP	Unit/Fuel	Feed system attrition exponent	Medium	High	
COFUSC	Hydrodynamic	Coarse particle velocity coeff	Medium	Medium	
COFDSC		Coarse particle dispersion coeff	Low	Medium	
COFDO		Gas dispersion coeff	Low	High	
COFUSF		Fines velocity coeff	Low	Low	
COFDSF		Fines dispersion coeff	Low	Low	
COFUOE		Entrainment rate coeff	High	Medium	
FRFLAK	Fuel	Weight fraction of CEMA flakes	Negl	Low	
KCAN		CEMA rate constant	Low	Low	
COFTAU		Coal particle heat-up time coeff	Negl	Medium	
VYULT		Ultimate volatile yield	High	Low	
COFFVY		Volatile yield coeff	Negl	Negl	
COFKV		Devolatilization rate coeff	Low	Medium	
KVEXP		Devolatilization rate exponent	Low	Low	
SIULT		Swelling index upper limit	Low	Low	
COFRCC/ RCCACT		Char reactivity (Pre-exponential factor/activation energy)	High	High	
E <sub>ibc</sub> Range (%)			68 - 91	63 - 85	

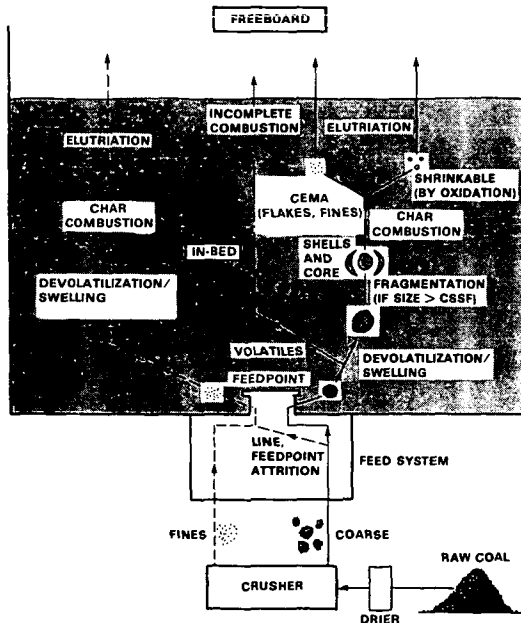


Figure 1. Coal combustion sequence for underbed feed.

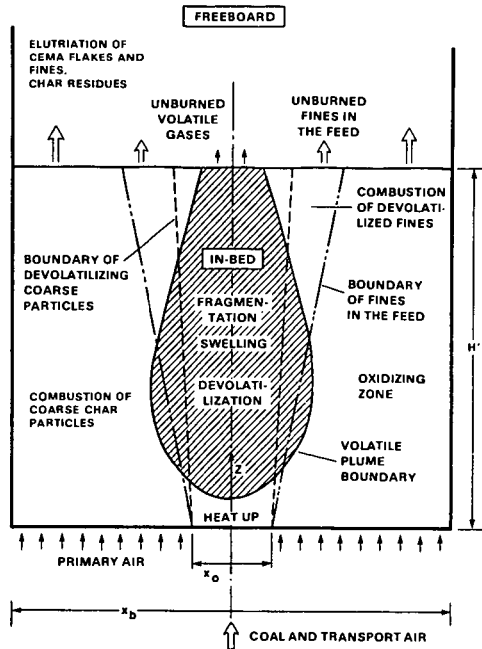


Figure 2. Conceptual model of in-bed combustion.

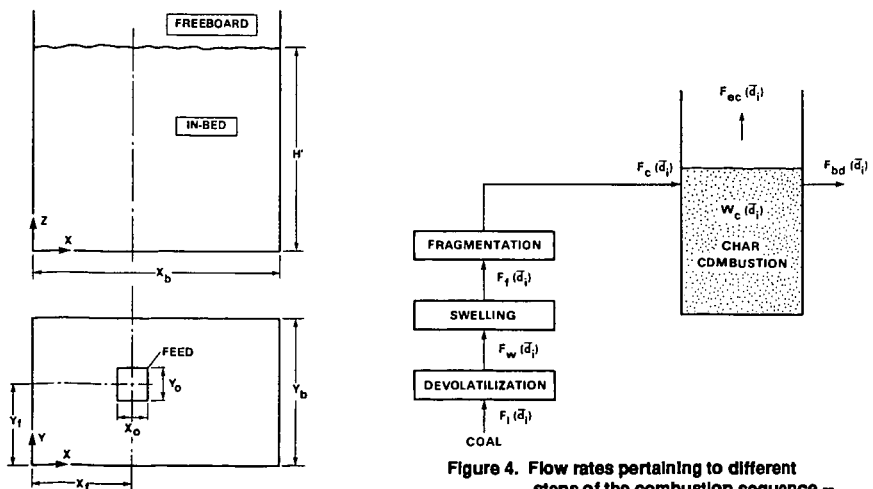


Figure 3. Unit cell coordinate geometry.

Figure 4. Flow rates pertaining to different steps of the combustion sequence - Region II model.

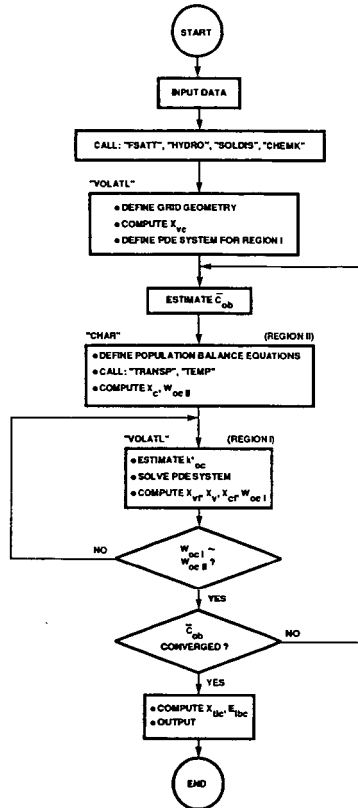


Figure 5. Performance code flowchart.

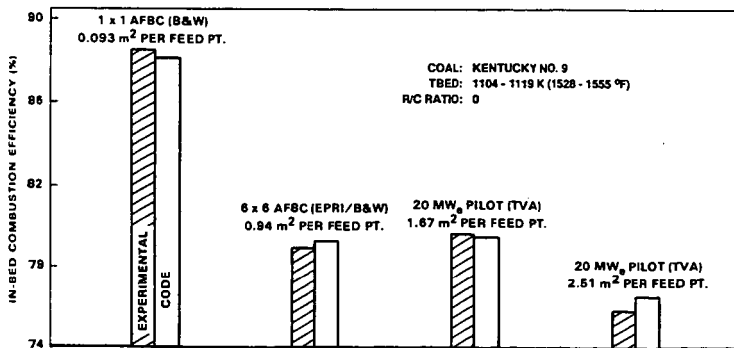


Figure 6. Comparison of performance code predictions with experimental data.

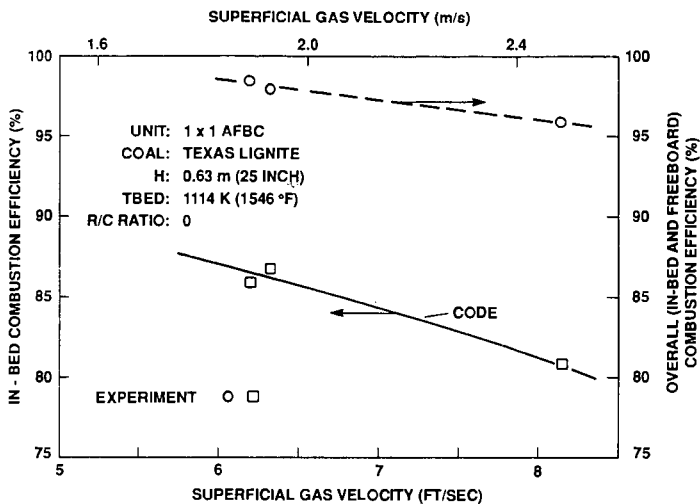


Figure 7. Comparison of code predictions with data.

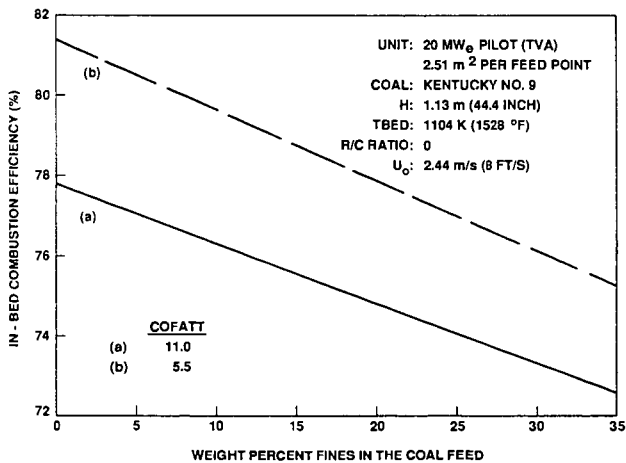


Figure 8. Simulation for coal hopper particle size distribution.

## CONTINUOUS KINETIC LUMPING FOR LIGNITE LIQUEFACTION

P. K. Moore and R. G. Anthony

Department of Chemical Engineering  
Texas A&M University, College Station, TX 77843

### INTRODUCTION

The need for an alternative energy source to counteract both short-term petroleum supply interruptions and the eventual depletion of petroleum reserves has resulted in an increased interest in the utilization of domestic coal. While coal can be utilized directly for energy applications such as electrical power generation, much of the petroleum demand is based in the liquid fuel and liquid feedstock areas. This potential demand for liquid fuel and feedstock has caused a renewed interest in coal liquefaction technology. However, the development of coal liquefaction technology to an industrially applicable level has been hindered by the lack of a suitable kinetic model. Current kinetic models are based upon simplified analytical techniques in which components are lumped into several solubility or volatility classes. These models must be used cautiously since compounds within the same solubility or volatility class do not necessarily undergo similar reactions. In addition, each kinetic model applies only to the particular coal studied. A critical need exists for a kinetic model based upon the actual chemical reactions occurring and which is applicable to a variety of coals. The development of such a kinetic model is the goal of the coal liquefaction studies at Texas A&M University.

The development of a kinetic model capable of describing a complex, many-component reaction, such as coal liquefaction, requires the investigation of several supporting areas: experimental reactions, analytical method, component lumping, reactor modeling, and parameter estimation. All of these areas depend on each other; hence, the resulting kinetic model is dependent on, and limited by, each area. Any attempt to improve the kinetic model must therefore effect an improvement in one or more of the supporting areas. The coal liquefaction research at Texas A&M University has resulted in significant advances in the areas of analytical technique, component lumping, and reactor modeling, thus providing the foundations for the development of a powerful new kinetic model.

The sections below describe the results which have been achieved and the course of the research now being followed in each of the supportive areas: experimental reactions, analytical method, component lumping, reactor modeling, and parameter estimation. In particular, several of the more significant developments are described and compared to the methods currently being used. These new developments include an improved analytical technique, the SEC-GC-MS method, based upon a combination of size-exclusion chromatography (SEC), gas-chromatography (GC), and mass spectroscopy (MS); an optimum component lumping technique developed by embedding the classical kinetic and equilibrium equations into the vector space of generalized functions; and a reactor model which incorporates an equation-of-state equilibrium calculation to predict the compositions of the reactants in both the liquid and vapor phases.

### EXPERIMENTAL REACTIONS

The commonly used types of coal liquefaction laboratory reactors have been discussed in detail by Shah (1). Continuous-flow reactors were not considered for this study due to the possibility of different residence times existing for each phase, a condition difficult to model, and due also to the difficulty in establishing a steady-state condition for the solid phase. The batch reactors commonly used in laboratory studies thus far are the batch autoclave, the rapid-injection autoclave, and the tubing-bomb microreactor. Of these three, the tubing-bomb microreactor was chosen for this kinetic study due to the reactor's low thermal inertia, good heat and mass transfer characteristics, and the small amount of reactor feed required (2).

The tubing-bomb reactors used at Texas A&M typically consist of a 6 inch long 3/4 inch o.d. stainless steel tube capped on each end. A thermocouple extends into the reactor via a 1/4 inch o.d. thermowell assembly. A 1/8 inch o.d. line to the reactor serves for gas charge and evacuation in addition to providing for pressure measurement during an experimental run. Various tubing-bomb reactors used at Texas A&M and the corresponding experimental procedures are described by Helton (3), Haley (4), Shumbera (5), and Koker (6).

## ANALYTICAL METHOD

The purpose of an analytical method, as applied to kinetic model development, is to provide a measure of the change which has occurred during the experimental reaction. This "measure of change" provided by the analytical method must 1) relate to the kinetic properties of the reaction mixture, so that the fundamental equations governing the chemical reactions may be easily applied, and 2) the properties relating to the uses of the reaction product, so that the resulting kinetic model may be used to optimize product yield and composition. When the reaction mixture is simple, consisting of relatively few components, the analytical technique provides an exact analysis; thus, both Criteria 1 and 2 above are readily satisfied. However, when the reaction mixture is complex, consisting of many components, an exact analysis is often impossible. An approximate analytical technique must then be used, and this approximate technique must attempt to satisfy the above criteria. Therein lies the failing of the approximate analytical techniques commonly used for coal liquefaction studies: solubility analysis and distillation analysis.

Solubility analysis consists of the separation of coal liquefaction products into portions which are soluble in a series of extraction solvents. A commonly used series of solvents consists of hexane, toluene, and tetrahydrofuran. Hexane solubles are designated as "oil," toluene solubles are designated as "asphaltenes," and tetrahydrofuran solubles are designated as "preasphaltenes." All of the material insoluble in tetrahydrofuran is considered to be unreacted coal, char, and ash. The solubility analysis method provides a rough picture of the changes occurring in the reaction mixture, and kinetic models have been developed using the component classes: oil, asphaltenes, preasphaltenes, and unreacted coal. However, the solubility analysis method fails to satisfactorily meet Criteria 1 and 2 mentioned above.

First, each component class, or lump, consists of a broad range of component types. The kinetic behavior of the component lump will, in general, depend in a complicated manner upon the components contained within the lump. Therefore, any information relating to actual molecular mechanism of coal liquefaction, which is formulated in terms of individual molecular types, will be difficult to incorporate into the overall kinetic model, which is formulated in terms of the lumped component classes. Furthermore, coal liquefaction is a multiphase process; the individual components within the reaction mixture are dispersed throughout the solid, liquid, and vapor phases. Since each phase may be expected to exhibit different reaction behavior, the distribution of each component in each phase may significantly affect the kinetic behavior of the reaction mixture. Hence, properties which describe the affinity of each component to a particular phase, such as volatility, should be included in the kinetic model. The solubility analysis method fails to provide such information, since each solubility lump may contain components with a broad range in volatility.

The solubility analysis also fails to satisfy the product criterion; the solubility lumps — oil, asphaltenes, and preasphaltenes — are difficult to relate to the end uses of the product. When the liquefaction products are to be used as chemical feedstock, the engineer is primarily interested in a particular component or group of components. The solubility lumps which contain the desirable group of components may also contain undesirable components. Hence, the liquefaction process cannot be easily optimized for the desired products. When the liquefaction products are to be used as fuel or fuel feedstock, volatility properties of the product become important; however, solubility lumps fail to incorporate such volatility information.

Distillation analysis also fails to satisfy the reaction and product criteria. Distillation

analysis separates the mixture into several volatility classes. However, these volatility classes contain several types of chemical components, with each component type exhibiting different kinetic behavior in the reaction mixture; hence, the volatility lumps, like the solubility lumps, are unable to provide a precise description of the reaction. Furthermore, a product description in terms of volatility lumps fails to provide chemical information about the product, which is often needed when the product is to be used as a chemical feedstock.

The failings of the traditional solubility and distillation analyses led to the development of the SEC-GC-MS analytical method at Texas A&M. In the SEC-GC-MS method, the tetrahydrofuran soluble portion of the liquefaction products is first separated into several fractions (usually 9) using size-exclusion chromatography (SEC) with tetrahydrofuran (THF) as the mobile phase. As shown by Anthony et al. (7), size-exclusion chromatography effects a separation of the mixture based upon molecular size and functionality, with alkanes eluting first, followed by phenols, and then aromatics. Each of the fractions obtained using size-exclusion chromatography is then analyzed using gas chromatography (GC), which effects a separation based upon volatility. A mass spectroscopic (MS) detector can be used with the GC to aid in peak identification. Details of the SEC-GC-MS method have been provided by Anthony et al. (8).

The SEC-GC-MS analytical method provides a distribution of the coal liquid sample with respect to the SEC retention index, which provides a measure of component functionality, and with respect to the GC retention index, which provides a measure of component volatility. This bivariate distribution (Figure 1) provided by the SEC-GC-MS method exhibits several advantages over the univariate distributions provided by the solubility and distillation methods. First, since the SEC-GC-MS method provides a separation of the mixture based on both volatility and component functionality, the bivariate distribution is easily related to both the kinetic properties of the reaction mixture and to the properties relevant to the desired uses of the product. Second, since all components eluting within a particular SEC-GC retention region can be expected to have similar chemical and volatility properties, lumping of neighboring components (components which elute with similar SEC and GC retention times) may be justified. Such lumping may be required when the chromatograms are poorly resolved, or lumping may be desirable to reduce the number of parameters within a kinetic model. Furthermore, all coals can be expected to yield the same types of components upon liquefaction, and these types of components should consistently elute with the same SEC and GC retention time, independent of the coal type being liquefied. This separation of the kinetic model from coal type was not possible with solubility analysis, since solubility lumps derived from different coals do not always contain the same amount of each component, or even the same components.

## CONTINUOUS LUMPING

The SEC-GC-MS analytical method yields an overwhelming amount of information. The method provides not only a good overall description of the mixture compositions, but also often provides detailed concentration information about individual components. However, such detail is often not necessary or desirable. The optimum kinetic model should provide the best possible mixture description using the fewest possible parameters. A kinetic model incorporating a large number of parameters is difficult to use; first, the presence of a large number of parameters makes parameter estimation difficult, and second, the large model becomes difficult to apply in subsequent design situations. Hence, a method was needed whereby the detailed SEC-GC-MS analysis could be parameterized using the fewest possible terms while retaining the bulk of the useful information from the SEC-GC-MS analysis. This parameterization procedure is referred to as "component lumping," or simply as "lumping."

The traditional form of lumping is pseudocomponent lumping, where groups of components are treated as individual components. However, we have developed (9) an alternate method, "continuous-lumping," which is particularly well-suited for calculations involving chromatographic data. Continuous-lumping can be considered a generalization, or reinterpretation, of



the theory of continuous mixtures, as described by Cotterman et al. (10) for thermodynamics and by Aris and Gavalas (11) for reaction kinetics. However, our developments have shown (9) that the continuous mixture hypothesis is not required for the method to be valid.

For continuous-lumping, the individual component properties — concentration, volatility, and reactivity — are considered to be functions of some suitable component index, such as molecular-weight or boiling-point. These component indices, in turn, can then be related to chromatographic retention-times. The classical description of the mixture composition (mole fractions) is then converted to a distribution function (similar to a chromatogram) written in terms of the component index. The classical relationships between the component properties (i.e., equilibrium relations, reaction-rate equations, etc.) are then converted to the functional form. The final step in the continuous-lumped method is the expansion of the functional equations in terms of generalized Fourier series to obtain an approximate set of algebraic equations — the continuous-lumped equations.

The bivariate distribution provided by the SEC-GC-MS analytical method is particularly well suited to the continuous lumping method, since the kinetic and volatility properties of the components vary gradually with the SEC and GC retention indices. In fact, the fundamental parameters of a kinetic model may be considered to be functions of the component indices instead of the usual interpretation, where the kinetic parameters are associated with the set of pseudo-components. Thus, the problem of kinetic model development becomes the determination of a kinetic parameter surface over the SEC-GC component index plane. This approach frees the model from the dependence on a particular choice of a pseudo-component lumping scheme, thus enabling comparison of data from two separate investigations in which different lumping schemes happened to be used. Furthermore, all of the components in a small neighborhood of a particular SEC-GC index pair can be expected to be chemically similar; therefore, a particular component from the neighborhood may be selected for a kinetic study. Such a "model compound" study possesses an advantage over a kinetic study of the complete coal liquid, since a particular kinetic parameter may often be determined with greater precision when the effects of the other kinetic parameters have been removed.

The detailed theory behind the continuous lumping method, as applied to vapor-liquid equilibrium calculations, has been developed by Anthony and Moore (9). The theory is presently being extended and fully developed to include reaction kinetics. The continuous lumping method will be incorporated in a reactor model (described in the next section) which will predict conversion and product distributions for the tubing-bomb reactor.

## REACTOR MODELING AND PARAMETER ESTIMATION

After the products of the experimental liquefaction reactions have been characterized using the SEC-GC-MS analytical method and the continuous lumping method, the resulting parameterized data, which describes the changes that occur during reaction, must be related to the fundamental kinetic model (in general unknown), which governs the changes that occur during reaction. When the assumed form of the kinetic model is simple, the kinetic and reactor model equations may be solved directly to obtain an analytical equation describing the reaction. The fundamental parameters within the kinetic model may then be estimated by fitting the analytical solution to the lumped data using a regression method. However, the assumed kinetic model and the reactor modeling equations often form a complex system, making an exact analytical solution difficult or impossible to obtain. The combined kinetic and reactor model equations, together with an assumed set of parameters, must then be solved using a numerical method to obtain predictions of reaction behavior. The combined kinetic and reactor model can then be incorporated into a parameter estimation routine, such as the Modified Marquart Method used by Tarng (12), in order to obtain optimum estimates of the kinetic parameters. This second approach, the reactor model — parameter estimation method, has been chosen to obtain estimates for the kinetic parameters, since the method is general and may therefore accommodate virtually any assumed form of the kinetic model.

Coal liquefaction is a complicated process involving reactions in and mass transfer between vapor, liquid, and solid phases; any theoretically based kinetic model must therefore account for the fundamentally different reactions and mechanisms in each phase. Heretofore, kinetic models have failed to incorporate this fact; the reaction mixture was treated as if it were one single phase, with any phase equilibrium effects being incorporated into the empirical kinetic model. Such a treatment is unacceptable, however, since different types of industrial reactors exhibit different types of phase equilibrium behavior. The kinetic model must, therefore, be based on the actual compositions in each phase, which must either be measured or predicted.

Measurements of phase compositions in a coal liquefaction reactor are always difficult and, in the case of the tubing-bomb reactor, may be impossible. However, as shown by Anthony et al. (13), an equation-of-state (EOS) vapor-liquid equilibrium calculation is capable of predicting the phase concentrations of key reactants, such as hydrogen, to a sufficient degree of accuracy. Figures 2 and 3 illustrate the prediction of VLE properties for a hydrogen-coal liquid mixture using an equation-of-state. Figure 2 shows an ASTM D-86 of a SRC-II coal liquid fraction. Bubble points for mixtures of this coal liquid with hydrogen were determined experimentally by Chao (14), as shown in Figure 3, where a VLE calculation using an equation-of-state is also shown. Note that the VLE calculation predicts the mole fraction of hydrogen in the liquid phase well. For this reason, plus the difficulty of sampling, an EOS vapor-liquid equilibrium calculation has been chosen to predict phase compositions in the reactor model. The incorporation of an EOS vapor-liquid equilibrium calculation into the reactor model has the disadvantage that the resulting kinetic model will depend on the particular EOS model chosen; however, the inaccuracies due to such a dependence are not likely to exceed the inaccuracies in the assumed form for the kinetic model. Furthermore, the EOS calculation may be used to find the conditions at which the phase compositions yield the optimum reaction behavior; this predictive function of the reactor model would not be easily available if the phase compositions were obtained by measurement. Hence, reactor conditions of particular interest, consisting of temperatures and pressures at which the liquid-phase reactions may be enhanced (such as the near-critical and supercritical regions), may be investigated.

## CONCLUSIONS

The key to an improved coal liquefaction kinetic model is the development of an analytical method capable of separating the reaction products into individual molecular components; The SEC-GC-MS analytical method satisfies this need by providing detailed compositional information, such as the chemical and volatility properties of each component. The tremendous detail provided by the SEC-GC-MS method can then be effectively parameterized using the continuous lumping method, which allows the detailed analytical results to be incorporated into complex kinetic and thermodynamic calculations, such as the equation-of-state VLE calculation described above. Thus, the SEC-GC-MS analytical method and the continuous lumping method, both developed at Texas A&M University, allow the application of advanced theory to the coal liquefaction process.

## ACKNOWLEDGEMENTS

The financial support of the U. S. Department of Energy (Project Number DE-AC18-83FC10601), the Texas A&M University Center for Energy and Mineral Resources, and the Texas A&M Engineering Experiment Station is gratefully acknowledged. The Energy Research Center at the University of North Dakota furnished samples for the study.

## REFERENCES

1. Shah, Y. T., *Reaction Engineering in Direct Coal Liquefaction*. Reading, Mass.: Addison Wesley, 1981.
2. Gallakota, S. V., and J. A. Guin, "Comparative Study of Gas-Liquid Mass Transfer Coefficients in Stirred Autoclaves, Tubing Bomb Microreactors, and Bubble Columns," *Ind. Eng. Chem. Process Design and Dev.*, vol. 23, pp. 52-59, 1984.
3. Helton, T. E., "A Solvent Study of the Direct Liquefaction of Big Brown Lignite," Thesis, Texas A&M University, Texas, 1986.
4. Haley, S. K., "A Kinetic Model for the Liquefaction of Texas Lignite," Thesis, Texas A&M University, Texas, 1980.
5. Shumbera, D. A., "Reaction Rate Kinetics for the Non-Catalytic Hydrogenation of Texas Lignite with Tetralin and Hydrogen Gas," Thesis, Texas A&M University, Texas, 1980.
6. Koker, A., "A Study of the Direct Liquefaction of Indian Head Lignite," Thesis, Texas A&M University, Texas, 1985.
7. Anthony, R. G., C. V. Philip, and P. K. Moore, "Kinetic Model Development for Low-Rank Coal Liquefaction," Quarterly Report: Jan. 1, 1986 - March 31, 1986; DOE/FC/10601-11.
8. Anthony, R. G., "Kinetic Model Development for Low-Rank Coal Liquefaction," Quarterly Report: Jan. 1, 1985 - March 31, 1985; DOE/FC/10601-7.
9. Anthony, R. G., and P. K. Moore, "Kinetic Model Development for Low-Rank Coal Liquefaction," Quarterly Report: April 1, 1986 - June 30, 1986; DOE/FC/10601-12.
10. Cotterman, R. L., R. Bender, and J. M. Prausnitz, "Phase Equilibria for Mixtures Containing Very Many Components. Development and Application of Continuous Thermodynamics for Chemical Process Design." *Ind. Eng. Chem. Process Design and Dev.*, vol. 24, pp. 194-203, 1985.
11. Aris, R., and G. R. Gavalas, "Theory of Reactions in Continuous Mixtures," *Phil. Trans. Roy. Soc. London*, vol. A260, pp. 351-393, 1966.
12. Tarng, Y. J., "A Reactor and Kinetic Model for Liquefaction of Lignite in an Upflow Tubular Reactor," Dissertation, Texas A&M University, Texas, 1985.
13. Anthony, R. G., A. Koker, P. K. Moore, Y. Tarng, "Kinetic Model Development for Low-Rank Coal Liquefaction," Quarterly Report: Oct. 1, 1983 - March 31, 1984; DOE/FC/10601-4.
14. Kim, H. Y., T. M. Guo, H. M. Linn, and K. C. Chao, "Equilibrium Vaporization of Coal Liquids," Paper No. 15 c, AIChE Annual Meeting, November 1983, Washington, D. C.



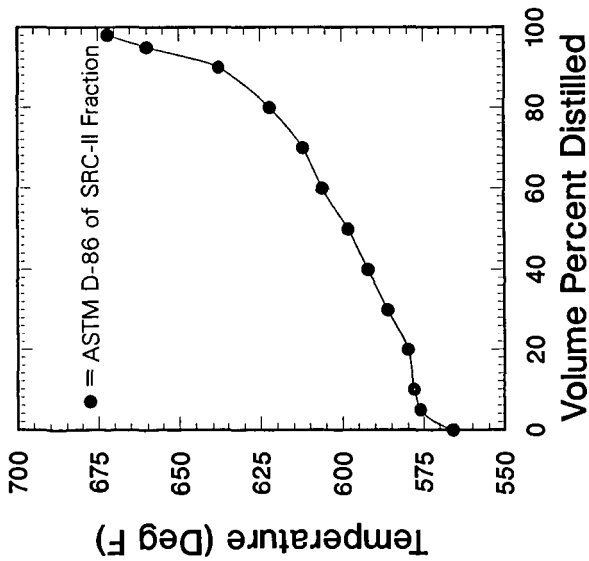


Figure 2 ~ ASTM D-86 of

SRC-II Coal Liquid Fraction.

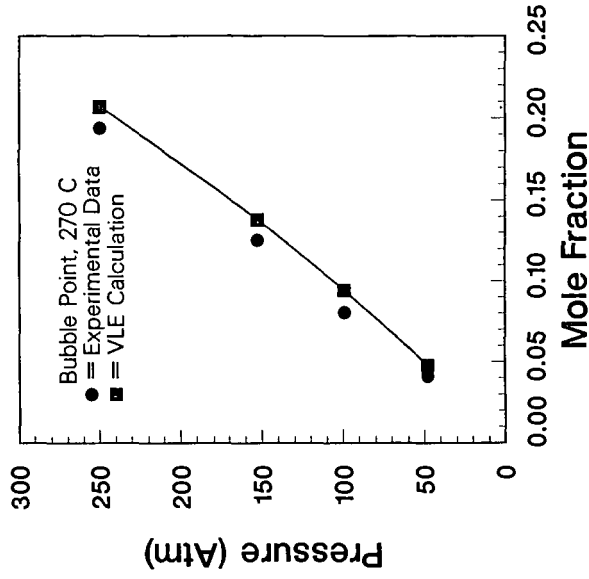


Figure 3 ~ Bubble Points of

Hydrogen / SRC-II Coal Liquid Mixture

# FUNDAMENTAL MODELLING OF PULVERIZED COAL AND COAL-WATER SLURRY COMBUSTION IN A GAS TURBINE COMBUSTOR

A. Chatwani, A. Turan and F. Hals

Avco Research Laboratory, Inc.  
2385 Revere Beach Parkway  
Everett, MA 02149

## INTRODUCTION

A large portion of world energy resources is in the form of low grade coal. There is need to utilize these resources in an efficient and environmentally clean way. The specific approach under development by us is direct combustion in a multistage slagging combustor, incorporating control of  $\text{NO}_x$ ,  $\text{SO}_x$ , and particulates. While experimental verification provides the ultimate proof of acceptability, there is an increasing realization that the detailed flow field computations of the combustion process can provide much of the necessary understanding and aid in the development process. A number of papers have dealt with the modelling of pulverized coal combustion in burners where flow field is predominantly two-dimensional (1-3). Many elements of this coal combustion model have been developed and validated under those conditions.

Our main interest is in the combustors where three-dimensional effects are of prime importance. An example of such a combustor is shown schematically in Fig. 1. The toroidal vortex combustor is currently under development through a DOE contract to Westinghouse and subcontract to ARL. This subscale, coal-fired, 6 MW combustor will be built and become operational in 1988. The coal fuel is mixed with preheated air, injected through a number of circumferentially-located jets oriented in the radius axis planes. The jets merge at the centerline, forming a vertically directed jet which curves around the combustor dome wall and gives rise to a toroidal shaped vortex. This vortex helps to push the particles radially outward, hit the walls through inertial separation and promote slagging. It also provides a high intensity flow mixing zone to enhance combustion product uniformity, and a primary mechanism for heat feed back to the incoming flow for flame stabilization.

Work describes the essential features of a coal combustion model which is incorporated into a three-dimensional, steady-state, two-phase, turbulent, reactive flow code. The code is a modified and advanced version of INTERN code originally developed at Imperial College which has gone through many stages of development and validation. Swithenbank et al<sup>(4-5)</sup> have reported spray combustion model results for an experimental can combustor. The code has since then been modified by and made public under a US Army program<sup>(6)</sup>. A number of code modifications and improvements have been made at ARL. The earlier version of code was written for a small CDC machine which relied on frequent disk/memory transfer and overlay features to carry the computations resulting in loss of computational speed. These limitations have now been removed. For spray applications, the fuel droplet vaporization generates gaseous fuel of uniform composition; hence the earlier formulation relied upon the use of conserved scalar approximation to reduce the number of species equations to be solved. In applications related to coal fuel, coal pyrolysis leads to the formation of at least two different gaseous fuels and a solid fuel of different composition. We have therefore removed the conserved scalar formulation for the sake of generality and easy adaptability to complex fuel situations.

### Pulverized Coal Combustion Model

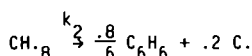
Combustion of pulverized coal particles is generally assumed to be a two-stage process consisting of devolatilization or pyrolysis of coal and heterogeneous char oxidation and gasification. The model adopted to describe pyrolysis is that of Kobayashi, et al.<sup>(7)</sup> This model proposes the use of two competing first order reactions to describe particle mass loss during pyrolysis. The process is described as



where  $V_1$  and  $V_2$  are volatiles of approximate elemental ratio  $C_6H_{12}$  and  $C_6H_6$ , and  $S_1$  and  $S_2$  are char residuals containing mostly C. Specifically for a dry ash free (daf) coal of the type CH<sub>8</sub>, these reactions can be expressed as



and



The rate of disappearance of daf coal is given by

$$-\frac{d}{dt} m_{\text{daf}} = (k_1 + k_2) m_{\text{daf}} \quad 3)$$

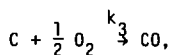
where  $m_{\text{daf}}$  is the mass of dry ash free coal,  $k_1$  and  $k_2$  are rate constants given by

$$\begin{aligned} k_1 &= 3.7 \times 10^5 \times \exp(-8860/T) \\ k_2 &= 1.46 \times 10^{13} \times \exp(-3017/T) \end{aligned} \quad 4)$$

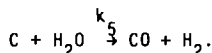
It should be noted that Equation 2 leads to volatiles yield of 0.43 and 0.81 for slow and very rapid heating respectively. It is relatively easy to modify composition of volatiles to fit the experimental data for different coal ranks including their oxygen, nitrogen, and organically bound sulfur content. The devolatilization of coal is assumed to take place without change in the particle radius and leaves behind a lighter porous particle.

### Char Oxidation and Gasification Model

Char gasification may be treated approximately as a three-stage process consisting of (i) diffusion of gaseous species to the surface, (ii) surface reaction, and (iii) diffusion of products to the bulk gas. Any of the processes may be a rate controlling step depending on the gas phase conditions, particle size and temperature, and particle pore structure. The model adopted is an extended version of Field<sup>(8)</sup> where surface diffusion and chemical reaction are taken into account. Three different surface reactions are included in the model, viz,



and



For the sake of simplicity, it is assumed that all three reactions proceed independent of each other so that the char consumption rate is sum of individual rates. Rate of  $O_2$  diffusion to the surface is given by

$$\frac{d}{dt} m_{O_2} = - k_D A_s (Y_{O_2}^\infty - Y_{O_2}^s) \quad 6)$$

and the rate of  $O_2$  consumption at the surface is given by

$$\frac{d}{dt} m_{O_2} = - k_r \cdot A_s \cdot Y_{O_2}^\infty \quad 7)$$

Under quasi-steady-state, the two rates from Equations 6 and 7 balance each other and unknown quantity  $Y_{O_2}$  can be eliminated to give

$$\frac{d}{dt} m_{O_2} = - k_{eff} \cdot A_s \cdot Y_{O_2}^\infty \quad 8)$$

where  $k_{eff} = k_r k_D / (k_r + k_D)$ . The diffusion rate  $k_D$  is related to the laminar diffusion coefficient, and the rate constants  $k_3 - k_5$ , taken from Stickler,(9) are given by

$$k_3 = 3.24 \times 10^{10} \times \exp(-14500/T),$$

$$k_4 = 5.75 \times 10^{13} \times \exp(-43200/T), \quad 9)$$

and

$$k_5 = 6.38 \times 10^{11} \times \exp(-30300/T).$$

Heterogeneous char combustion is assumed to take place at the outer surface resulting in the removal of material from the surface at the constant particle density.

Devolatilization or blowing out of gaseous products hinders the diffusion of gas phase species to the surface. It is assumed that char oxidation does not begin until the devolatilization is complete.

#### Coal Water Slurry Combustion Model

The presence of water in pulverized coal either as moisture or as a slurry forming medium further complicates the modelling of coal pyrolysis processes. In general, the size distribution of coal slurry droplets is governed by the injector performance, and a typical slurry droplet may consist of many parent coal particles. The slurry droplet may undergo many different processes depending on the history of heating rates to which a particle is



subjected; these may include swelling under simultaneous or sequential vaporization of water and coal gaseous products, shattering of droplet into parent coal particles or even smaller particles, or fusion of porous char and ash particles. The model adopted here is the most simplistic one, which will be replaced by a more realistic model in the future. We assume that water vapor and coal devolatilization occur in a sequential process, with each droplet consisting of a single coal particle and a corresponding mass of water. Hence the spray size distribution is dictated by the original coal particle size distribution assumed. The initial step in the heating of the droplet is to increase particle temperature to the saturation temperature of water. This is followed by the water vaporization at the constant particle temperature until the particle is dry. Once the particle is dried it behaves like a dry coal particle. The sequential vaporization model has been found to be adequate for the case of coal water slurry turbulent diffusion flames.<sup>(10)</sup>

#### Gaseous Combustion Model

The original version of INTERN incorporated a two step reaction scheme for which differential transport governing the evolution of the mixture fraction  $f$ , mass fraction of unburned fuel  $m_{fu}$ ; and mass fraction of CO,  $m_{CO}$ , were solved. Concentrations of other reactants including  $m_{O_2}$  as well as equilibrium combustion products ( $m_{CO_2}$ ,  $m_{H_2O}$ ,  $m_{N_2}$ , etc.) were obtained via algebraically formulated balance expressions.

To represent the combustion of two different kinds of volatiles and solids typical of coal combustion, the following global mechanisms are postulated. The volatiles are assumed to combust to yield products CO and  $H_2$  in the initial stage.



The initial breakdown to CO and  $H_2$  instead of  $CO_2$  and  $H_2O$  is chosen to represent the fuel rich combustion situation of interest here. Subsequent oxidation of CO and  $H_2$  are given by



Empirical rate constants  $k_6$  to  $k_9$  are required for finite rate kinetics. Reverse rate constants  $k_{8b}$  and  $k_{9b}$  are calculated from equilibrium considerations. For turbulent flows, the effective reaction rates are calculated from the eddy breakup model<sup>(11)</sup>. In the absence of rate constants, the assumption of fast chemistry is invoked and all rates are limited by the turbulent mixing rates.

## RESULTS AND DISCUSSION

A number of cases were computed for the toroidal vortex combustor geometry of interest. The combustor configuration, and the inlet air flow conditions have been kept constant throughout these computations. The initial conditions are summarized in Table 1. The composition and size distribution of fuel have been varied parametrically to examine its influence on the flow field. The range of variations for the variables are summarized in Table 2. In all the computations reported here, it is assumed that the tip of the coal injector is located at the center of the air jet and in the plane of the combustor wall. Coal particles are assumed to leave the injector at surrounding air velocity, but at room temperature, and the mass flux of carrier gas is assumed negligible compared to the coal mass flux.

The computations were performed on a grid of  $37 \times 16 \times 9$  nodes by finite difference algorithm of INTERN code. The iterations were carried out until the absolute sum of mass residuals was below a few percent. A typical set of velocity vector plots is shown in Fig. 2. The results for the injector plane ( $k = 5$ ) show the existence of the jet directed towards the centerline. This jet broadens as it approaches the centerline and changes into a wall directed jet which curves along the walls of the combustor dome and escapes the injector plane by flowing around the initial jet. A circular vortex is seen to exist in the left hand corner of the combustor in each plane.

The typical set of calculated trajectories for the pulverized coal particles are shown in Fig. 3. A total of eight different size groups were selected such that the mass fraction in each size group is uniform. The mass weighted mean diameter for the distribution is  $50 \mu\text{m}$  which roughly corresponds to 80 percent minus 200 mesh. In the computations, the particles are injected at the injector plane and their trajectories are followed until one of the three conditions is met: (i) particle combusts and is converted to an ash particle, at which time it is removed from further consideration, (ii) the particle hits the wall, or (iii) particle exits the combustor.

The fate of the particle hitting the wall depends on the wall boundary conditions. If walls are slagging then a particle is captured by the slag, follow the slag and in the process react through pyrolysis or a char burning mechanism. Since in the present work details of slag wall layer flow are not resolved, two limiting cases of particle wall interaction are considered. In the first case it is assumed that any particle hitting wall is completely lost from further consideration, while in the second case it is assumed that a particle hitting the wall is completely decomposed into gaseous fuel at the constant temperature. The latter process will be approached in the limit of extremely hot and sticky slag of negligible velocity, so that all volatilization will occur in the vicinity of the impact point. Since in most cases of practical interest, the design should ensure maximum burning in suspension, details of wall particle interaction may not be critical to combustion stability and flow field structure. However, wall reaction can contribute extensively to combustion of large coal particles. They ordinarily dominate residence time requirements for pure suspension combustion, and are most effectively combusted via wall reaction, which effectively provides extended residence time. In terms of fuel energy utilization, this mechanism is most attractive under reducing flow conditions.

In the case of dry pulverized coal (Case 1) with a mass mean particle diameter of  $50 \mu\text{m}$ , approximately 81 percent of the fuel is utilized before particles hit the wall. If the fuel is substituted with a coal water mixture containing 30 percent water (Case 2) but otherwise the same size distribution as the dry coal, the fraction of fuel utilized is slightly increased to 86 percent. The slight increase in the fuel utilization may possibly be due

to the increased contribution from the gasification rate. The overall characteristics of the flow are unchanged, and there is a slight decrease in the temperature levels. Particles up to  $23\text{ }\mu\text{m}$  are completely converted to ash in less than 34 ms, while larger particles only react partially before hitting the wall. The presence of water in coal alone does not adversely affect the combustion process, and there is slight evidence to suggest a beneficial effect possibly due to increased gasification of the char (see Equation 5).

The combustion process is more strongly dependent on the initial size distribution. Reducing the mass mean size from  $50\text{ }\mu\text{m}$  (80 percent minus 200 mesh) to  $33\text{ }\mu\text{m}$  (80 percent minus 325 mesh) results in increase of the fraction utilized from 86 percent to 94 percent (Case 3). In many coal water slurry applications, as discussed before, the size distribution of droplets is governed by the injector performance. If it is assumed that the injector produces practically monosized droplets of  $33\text{ }\mu\text{m}$  diameter (Case 4), then the fraction of fuel utilized is dramatically reduced to 58 percent. Thus, as is well known, size distribution plays an important role in the combustion process. In the presence of a typical broad size distribution, fine particles release energy to increase the temperature level so that a  $33\text{ }\mu\text{m}$  droplet is 70 percent utilized before it hits the wall, while in the presence of monosized droplets, a  $33\text{ }\mu\text{m}$  droplet is 56 percent utilized.

If one assumes that a droplet is utilized completely as it hits the wall (Case 5) then by definition fuel is completely converted to gaseous fuel. In all the cases examined here, the combustor is operated fuel rich and utilization of  $\text{O}_2$  is complete. Even when the fuel is not completely combusted, the combustor outflow is devoid of any oxygen. The volatiles released in the pyrolysis phase are of  $\text{C}_6\text{H}_{12}$  and  $\text{C}_6\text{H}_6$  type, and some uncombusted volatiles (up to 2 percent by weight) are predicted. The presence of uncombusted volatiles may be due to the incomplete turbulent mixing of the volatiles or due to the inadequacy of the model which lacks the kinetic route for the dissociation or gasification of gaseous fuel to CO and  $\text{H}_2$ .

The combustor exit conditions are relatively insensitive to the initial size distribution and composition of fuel. The detailed temperature and species distributions inside the combustor, however, are strongly sensitive to the size distribution. As an example the temperature and CO mass fraction contours in the injector plane are compared in Figs. 4 and 5, respectively.

The ability of the code to compute complex three-dimensional combustor flow fields has been demonstrated. The purpose of the model work was specifically as a design tool for exploration of combustor geometry, sizing, and fuel choices. It was successful and useful in that regard. The model has given reasonable qualitative prediction of the toroidal vortex flow field under cold flow conditions.<sup>(12)</sup> Also, as the test data become available from the combustor development program, quantitative comparisons will be made and the model revised to improve physical assumptions.

#### Acknowledgement

This work was performed under the Department of Energy Contract No. DE-AC21-86MC23167 to Westinghouse, Subcontract to ARL under Westinghouse Purchase Order No. 293602.

## References

- (1) Lockwood, F. C., Rizvi, S.M.A., Lee, G. K. and Whaley, H., Twentieth International Symposium on Combustion, pp 513-522, Combustion Institute, Pittsburgh, 1984.
- (2) Truelove, J. S., pp 523-530, *ibid*.
- (3) Smoot, L. D., and Smith, P. J., Coal Combustion and Gasification, Plenum Press, New York, 1985.
- (4) Swithenbank, J., Turan, A., Felton, P. G., and Spalding, D. B., AGARD Conference Proceeding No. 275 on Combustor Modelling, 1979.
- (5) Turan, A., A Three-Dimensional Mathematical Model for Gas Turbine Combustors, Ph.D. Thesis, University of Sheffield, 1978.
- (6) Bruce, T. W., Mongia, H. C., and Reynolds, R. S. Combustor Design Criteria Validation, Vol. III, USARTL-TR-78-55, AVRAD Com, Fort Eustis, Virginia, March 1979.
- (7) Kobayashi, H., Howard, J. B., and Sarofim, A. F., Eighteenth International Symposium on Combustion, p 411, The Combustion Institute, Pittsburgh, 1977.
- (8) Field, M. A., Combust Flame, 14 237 (1970).
- (9) Stickler, D. B., Becker, F. E., and Ubhayakar, S. K., AIAA Paper No. 79-0298.
- (10) Srinivasachar, S., Farmayan, W. F., and Beer, J. M., Second European Conference on Coal Liquid Mixtures, 16-18 Sept., 1985, London.
- (11) Magnussen, B.F., and Hertager, B. H., in Sixteenth International Symposium on Combustion, p 719, The Combustion Institute, Pittsburgh, 1977.
- (12) Chatwani, A.U., and Turan, A. Submitted to Western States Meeting of the Combustion Institute, Salt Lake City, Utah, March 1988.

TABLE 1  
COMBUSTOR CONFIGURATION AND INITIAL CONDITIONS

Combustor Diameter	0.35 m
Injector-Dome Length	0.43 m
No. of Injectors	4
Injection Angle	60
Air Flow Rate	0.37 kg/s
Air Injection Velocity	70 m/s
Air Injection Temp.	617 K
Air Pressure	6 atm

TABLE 2  
INITIAL CONDITIONS FOR FUEL COMPOSITION

	Case <u>1</u>	Case <u>2</u>	Case <u>3</u>	Case <u>4</u>	Case <u>5</u>
$\dot{m}_{fuel}$	0.051	0.073	0.073	0.073	0.073
$\dot{m}_{water}/\dot{m}_{fuel}$	0.0	0.3	0.3	0.3	0.3
$\dot{m}_{daf}/\dot{m}_{fuel}$	0.95	0.665	0.665	0.665	0.665
d	50 $\mu$	50 $\mu$	33 $\mu$	33 $\mu$	33 $\mu$
f(d)	exp ( d/d)	exp ( d/d)	exp ( d/d)	$\delta$ (d/d)	$\delta$ (d/d)
$\phi$	1.3	1.3	1.3	1.3	1.3
Particle/Wall Interaction Model	1	1	1	1	2

- (1) Particle Capture, no vaporization  
(2) Particle Capture, Complete vaporization

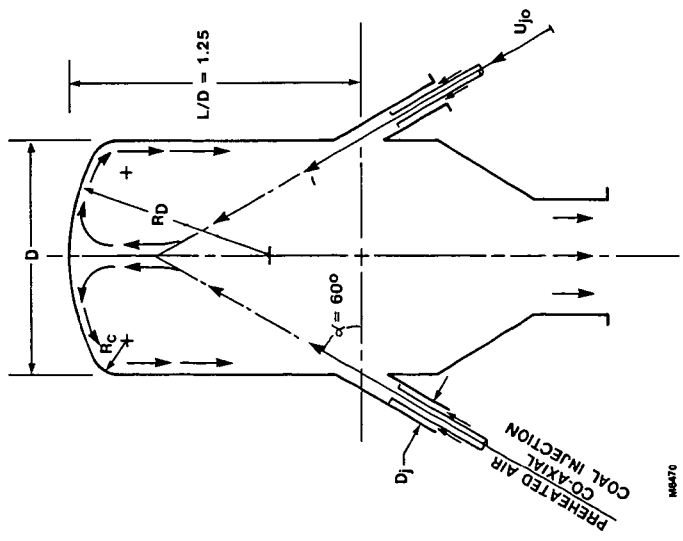


Figure 1 Schematic of Combustor Geometry

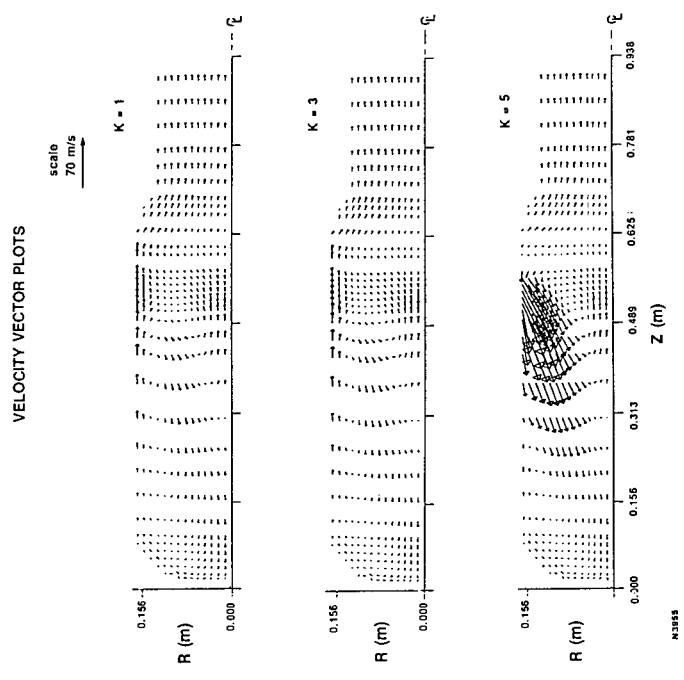
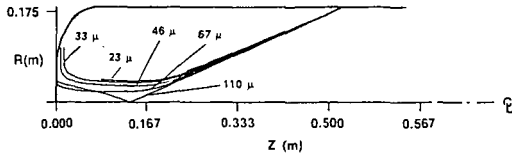


Figure 2 Typical velocity vector plots in  $r$ - $z$  Plane

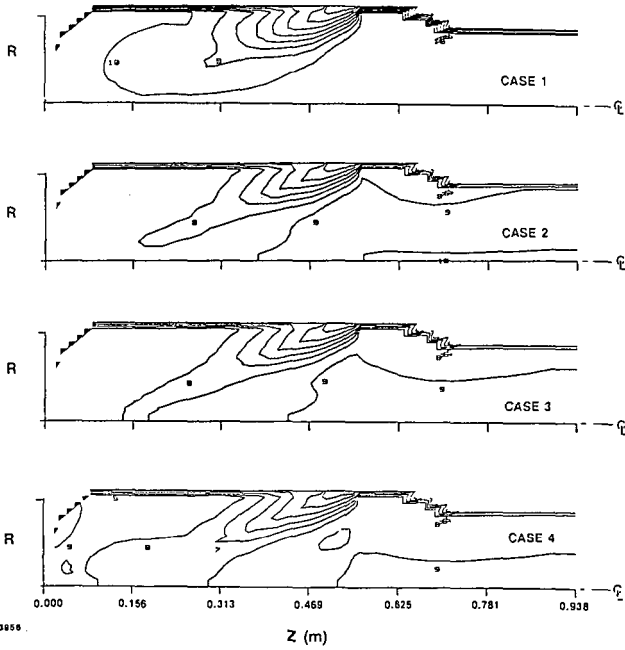
# PARTICLE TRAJECTORIES



N3657

Figure 3 Typical Particle Trajectories in r-z Plane

# TEMPERATURE CONTOURS



N3656

Figure 4 Computed Temperature Contour Plots.  
Contour 1 = 300K, Contour 11 = 2800K, increment = 250K

# CO MASS FRACTION CONTOURS

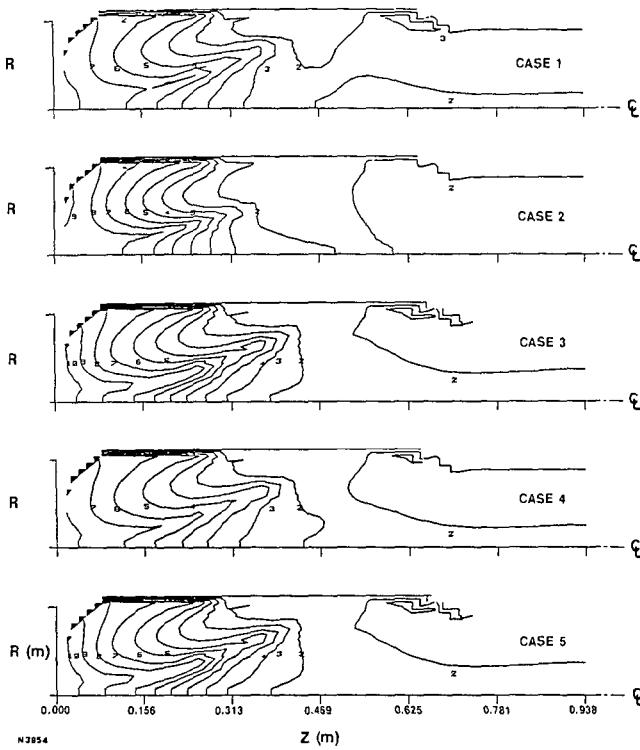


Figure 5 Computed CO Mass Fraction Contour Plots.  
Contour 1 = 0, Contour 11 = 0.4, increment = 0.04



## MODELING OF AGGLOMERATION IN A FLUIDIZED BED

A. Rehmat, C. Huang,\* R. Carty

Institute of Gas Technology  
Chicago, Illinois 60616

H. Hariri, H. Arastoopour

Illinois Institute of Technology  
Chicago, Illinois 60616

### ABSTRACT

A fluidized bed containing a central jet was operated with low-temperature melting materials to obtain the rate of agglomeration as well as to measure the temperature distribution within the fluidized bed. The rate of agglomeration was obtained as a function of operating parameters such as temperature and velocity. The agglomeration rate defined, as the rate of change in the number of particles of a particular size, was determined from the particle population balance using the experimental data.

The agglomeration model developed to predict the agglomeration rate constant based on the temperature distribution in the fluidized bed and the rate of entrainment of particles into the jet yielded values for the rate constants similar to the experimental values.

### INTRODUCTION

Fluidized-bed systems have been used in many coal conversion and other chemical processes. The fluidized beds are sometimes operated under agglomerating conditions to maximize coal utilization. The operating conditions in such cases are chosen to prevent the onset of sinters and defluidization (1,2,3,4). Under suitable operating conditions, ash agglomeration provides a very effective means of ash removal from a coal gasifier (5).

A distinguishing feature of an ash-agglomerating coal gasifier is a region where the temperature of the ash particles is high enough to make the surfaces sticky so that when they collide with each other, they adhere to each other to produce agglomerates. The rate of the formation of these agglomerates depends upon several factors such as the oxidant distribution within the bed, the overall fluidization velocity, and the ash properties. The oxidant distribution primarily influence the formation of the localized zone of high temperature within the fluidized bed, whereas the velocity influences the rate of particle collision as well as the particle entrainment within this zone. Based on these factors, a mathematical model for agglomeration has been developed to predict the rate of agglomeration in a fluidized bed containing a central jet. These rates are then compared with those obtained from the actual experiments.

### EXPERIMENTAL APPARATUS AND PROCEDURE

The apparatus consists of a 15.2-cm-ID glass fluidized-bed column, a metal section positioned beneath the glass column for temperature measurement and sampling, a gas distributor, a jet and fluidizing air heating system, temperature controlling and temperature measurement devices, and flow regulation and measurement systems (Figure 1). In the experiment, the jet and the fluidizing air temperatures

\*Dr. Huang is currently at Nalco Chemical, Naperville, Illinois.

were varied and the temperature distribution and the agglomeration of the particles in the bed were measured. Polyethylene and polyolefin particles were used as bed material. Two types of gas distributors were used: a flat porous plate with a central jet and a porous cone with a central jet.

The jet gas temperature was adjusted to a value above the melting temperature of the bed material. The fluidizing air (auxiliary air) temperature was generally maintained lower than the softening temperature of the bed material to avoid sinter formation on the distributor.

#### EXPERIMENTAL RESULTS

Figure 2 shows the effect of jet temperature on the agglomeration for a flat porous distributor with high-density polyethylene bed material. The measure of agglomeration is the weight percentage of particles greater than 850  $\mu\text{m}$ , which increased linearly with residence time at each temperature level. The percentage of agglomerates also increased linearly with the fluidizing gas and bed temperatures; however, the jet air temperature was found to have the most significant effect on the agglomeration rate.

Another important factor affecting the rate of agglomeration in fluidized beds is the rate of particle entrainment into the high-temperature jet region. The entrainment rate depends on the stress distribution among the particles in the vicinity of the jet region. The direction, magnitude, and component of the stress toward the jet region depends on the cone angle. Figure 3 compares the agglomeration obtained with gas distributors having half-cone angles of 30°, 45°, 60°, and 90° (flat) after 2, 4, 6, and 8 hours of steady-state operation. The agglomeration increased as the cone angle decreased up to 45°. However, when the cone angle was decreased to 30°, the agglomeration was found to be less than that with cone angle of 45°. This implies that, although the steeper inverted cone directed the stress on the particles in the cone section more effectively toward the jet zone, the amount of particles in the cone section decreased resulting in lower entrainment of the particles. Because of this competitive effect, there exists an optimum cone angle for the maximum rate of agglomeration. This half-cone angle is approximately 45°. The optimum angle can be a function of particle-size distribution, shape and surface roughness of the particles, and the jet and the fluidizing air velocities.

The temperature distribution inside the bed was plotted using temperature measurements at more than 50 locations inside the fluidized bed. A typical temperature distribution profile in the area near the porous cone distributor is illustrated in Figure 4. More data concerning other operating conditions are given elsewhere. (6).

#### DATA ANALYSIS

In a fluidized bed operated under agglomerating conditions, the rate of agglomeration between particles of two different sizes is proportional to the product of their concentrations. The proportionality constant is called the agglomeration rate constant.

To define the rate of agglomeration, we have adopted a definition that is analogous to the rate of chemical reaction. In a chemical reaction, the rate of reaction is defined in terms of the rate of change in the number of moles of a particular component in the reacting system due to its reaction. In the agglomeration process, what is changed during the process is the particle-size distribution. Therefore, it is appropriate to define the rate of agglomeration of particles of a particular size as the rate of change in the number of particles of that size. Due to the difficulty in measuring the number of particles of a particular size per unit volume of the fluidized bed, it has been found convenient

to express the rate of agglomeration of the particles in terms of its rate of change per unit mass of the bed material.

Since the overall rate of agglomeration is a measure of the rate of change in the number of particles of various sizes, the particle size is defined in a manner that is meaningful and facilitates the numerical computation in the particle population balance. It is assumed that all particles are made up of unit particles of mass  $m_0$  and diameter  $d_0$ . This assumption implies that particle size is discrete and each particle has a mass equal to an integer times the mass of a unit particle. The particle whose mass is  $I$  times the mass of a unit particle ( $I \times m_0$ ) is called particle size  $I$ .  $N(I)$  is defined as the number of particles of size  $I$  per unit mass of bed material and is called the mass number density of particles of size  $I$ . The rate of agglomeration of particles of size  $I$  can be expressed as:

$$R(I) = \frac{dN(I)}{dt} \quad 1)$$

The value of the rate of agglomeration  $R(I)$  is dependent upon operating variables, including the temperature distribution in the bed, velocity, and particle-size distribution.

If we assume the agglomeration process as involving the collision of a single particle of size  $I$  and a single particle of size  $J$ , then it is reasonable to assume that the generation rate of agglomerates ( $I + J$ ) forming from particles of size  $I$  and particles of size  $J$  is proportional to the collision frequency between these particles. As the number of collisions between particles of any two particular sizes is proportional to the product of their mass number densities, the rate of generation of agglomerates of size ( $I + J$ ) from particles of sizes  $I$  and  $J$  is:

$$R_{I,J} = K_{I,J} N(I) N(J) \quad 2)$$

Here,  $K_{I,J}$  is the agglomeration rate constant.

Particle Population Balance for Batch Process. In the population balance of the particles of a particular size  $I$ , all the possible combinations leading to the formation or consumption of size  $I$  particles are to be considered since particles of size  $I$  combines with other particles to form agglomerates of larger sizes; on the other hand, smaller particles may stick together and form agglomerates of size  $I$ . Using Equation 1, the rate of generation of agglomerates of size  $I$  from smaller particles is:

$$\frac{1}{2} \sum_{J=1}^I K_{I-J,J} N(J) N(I-J)$$

Similarly, the rate of consumption of particles of size  $I$  due to agglomeration is:

$$\sum_{J=1}^L K_{I,J} N(I) N(J)$$

where  $L$  is the size of the largest particles that exist in the bed. The population balance for particles of size  $I$  in batch process can thus be written as:

$$\frac{\partial N(I)}{\partial t} = \frac{1}{2} \sum_{J=1}^I K_{I-J,J} N(J) N(I-J) - \sum_{J=1}^L K_{I,J} N(I) N(J) \quad 3)$$

Computation of Agglomeration Rate Constant. For the computation of the agglomeration rate constant from the data, it is first expressed in terms of the operating variables and particle sizes. This approach facilitates in solving the rate constant integral equations. The agglomeration rate constant  $K_{I,J}$  can be

represented by the product of two functions; the first function,  $k_{op}$ , is dependent upon the operating conditions, and the other,  $k(d_I, d_J)$ , is size-dependent, as:

$$K_{I,J} = k_{op} k(d_I, d_J) \quad (4)$$

It is difficult to obtain an expression for  $k(d_I, d_J)$  from a theoretical standpoint. Based on the behavior of particles, one restriction that can be imposed on the functional form of  $k(d_I, d_J)$  is that it should be symmetric with respect to  $d_I$  and  $d_J$ . The ultimate functional form of  $k(d_I, d_J)$  must be determined with the aid of experimental data.

Even with the assumptions of Equation 4, there are still too many possible combinations of  $k_{op}$  and  $k(d_I, d_J)$  to be tested, and further simplification of the testing procedure is needed. To achieve this, the particle population balance Equation 3, for a specific operating condition, is rearranged as follows:

$$k_{op} = [MN(I)/Mt] / \left[ \frac{1}{2} \sum_{I=1}^I k(d_{I-J}, d_J) N(J) N(I-J) d_J - \sum_{I=1}^L k(d_I, d_J) N(I) N(J) d_J \right] \quad (5)$$

Thus, if the correct functional form of  $k(d_I, d_J)$  is used in Equation 5, the calculated  $k_{op}$  should have the same value for all of the particle sizes under specific operating conditions. This provides a means to test the functional form of  $k(d_I, d_J)$ . To find the correct functional form of  $k(d_I, d_J)$ , several symmetric functions with respect to  $d_I$  and  $d_J$  were substituted into Equation 5. Our studies showed that the functional form of

$$(d_I^4 + d_J^4) \left( \frac{1}{d_I^3} + \frac{1}{d_J^3} \right)$$

results in a nearly constant value of  $k_{op}$  over the whole particle size range at specific operating conditions. Therefore,  $K_{I,J}$  can be expressed as:

$$K_{I,J} = k_{op} (d_I^4 + d_J^4) \left( \frac{1}{d_I^3} + \frac{1}{d_J^3} \right) \quad (6)$$

The experimental data was used to calculate  $MN(I)/Mt$ ; then the agglomeration rate constant  $k_{op}$  was calculated using Equations 5 and 6. These values at different jet temperatures are shown in Table 1.

Table 1. THE CALCULATED VALUES OF  $k_{op}$  BY PARTICLE POPULATION BALANCE USING EXPERIMENTAL DATA

Jet Temp, °C	144.4	143.3	142.8	142.2
$k_{op}$	$1.78 \times 10^{-9}$	$1.20 \times 10^{-9}$	$0.9 \times 10^{-9}$	$0.45 \times 10^{-9}$

The value of  $k_{op}$  increases significantly with a slight increase in jet temperature (Table 1 and Figure 2).

#### AGGLOMERATION MODEL

As the hot jet gas stream is fed into the fluidized bed through the nozzle at a temperature substantially higher than the fluidizing gas temperature, a hot jet zone in the central portion of the bed is created. The concentration of solids in the jet zone is much lower than the solids concentration in the bulk of the bed. The solid particles enter the jet zone and exchange heat with the hot jet gas. The temperature of the particles in the jet zone increases; for some particles, this

results in partial melting. Upon the collision of two sticky particles, agglomeration may occur. Whether agglomeration takes place or not depends on several particle characteristics, including the relative velocity of the colliding particles, the thickness of the molten layer, and the viscosity of the molten material.

In the area near the jet, the particles are assumed to travel horizontally as they are entrained into the jet until they reach the jet boundary where particles enter into the jet zone and travel upward and finally exit from the top of the jet.

The entrainment of gas into a free jet has been given by Ricou and Spalding (7) as:

$$\frac{M_g}{M_{go}} = 0.32 \left( \frac{x}{d_n} \right) \left( \frac{\rho_{g1}}{\rho_{go}} \right)^{1/2} \quad (7)$$

where —

$M_{go}$  = mass flow rate of initial jet gas, kg/h

$M_g$  = mass flow rate of initial and entrained gas, kg/h

$x$  = distance from nozzle exit, m

$d_n$  = nozzle diameter, m

$\rho_{g1}$  = density of entrained gas, kg/m<sup>3</sup>

$\rho_{go}$  = density of gas exiting nozzle, kg/m<sup>3</sup>

The presence of particles may affect the entrainment of gas into the jet stream. However, this effect was found to be negligible for the particle-size range (mean particle diameter = 350  $\mu$ m) used in this study (8). The particles are entrained near the jet by the entrained gas; then they change direction and move upward due to momentum exchange with the jet gas. In this study, the flow of gas entrained to the jet is negligible in comparison with the jet gas flow rate. However, the rate of gas entrainment has been used to estimate the particle entrainment into the jet. As the particles enter into the jet, they travel upward due to the jet gas momentum. The following momentum balance was used to calculate the particle velocity in the jet zone.

$$\epsilon_p \rho_p v_p \frac{dv_p}{dx} = \frac{3}{4} C_D \frac{\rho_g (v_g - v_p)^2}{g_c d_p} (1 - \epsilon_p)^{-2.6} - (\rho_p - \rho_g)g \quad (8)$$

where  $x = 0$  defines the location where the particles enter the jet zone.  $v_p$  and  $v_g$  are particle and gas velocities, respectively,  $\epsilon_p$  is the particles void fraction, and  $C_D$  is the drag coefficient.

With the assumption that heat transfer to a particle is via heat exchange with its surrounding gas stream, the heat balance on a single particle in the region near and in the jet is expressed as:

$$\frac{\partial T_p}{\partial t} = \alpha \left[ -\frac{1}{r} \frac{\partial}{\partial r} \left( r^2 \frac{\partial T_p}{\partial r} \right) \right] \quad (9)$$

where  $\alpha$  is the particle thermal diffusivity.

$$\text{at } t = 0, T_p = T_B \quad (10)$$

where  $T_B$  is the bed temperature

$$\text{at } r = 0, \frac{\partial T_p}{\partial r} = 0 \quad (11)$$

and

$$\text{at } r = R, K_S \frac{\partial T_p}{\partial r} = \begin{cases} h(T_v - T_p) & \text{near the jet} \\ h(T_j - T_p) & \text{at the jet zone} \end{cases} \quad (12)$$

where  $K_S$  is the thermal conductivity of particles,  $T_j$  is jet temperature, and  $T_v$  is the temperature in the region near the jet. (Both temperatures are measured experimentally.) The heat transfer coefficient  $h$  is computed using the following expression (9):

$$\frac{hd_p}{k_g} = 2.0 + 0.6 \left( \frac{d_p \rho_g (v_g - v_p)}{\mu_g} \right)^{1/2} \left( \frac{c_p \mu_g}{k_g} \right)^{1/3} \quad (13)$$

where  $k_g$  is the gas thermal conductivity,  $v_g$  is the gas stream velocity,  $v_p$  is the particle velocity,  $d_p$  is the diameter of the particle,  $\mu_g$  is gas viscosity, and  $c_p$  is the specific heat.

Using the above heat and momentum equations, the temperature of a single particle  $T_p$  at any location near and in the jet can be calculated.

If the calculated temperature of the particles,  $T_p$ , in the jet zone reaches the melting temperature, the outer layer of the particles melt, and the particles may agglomerate upon collision. For each collision, there is only a finite probability of  $P^*$  leading to successful agglomeration.

The probability  $P^*$  is the fraction of all the collisions, which meet the following agglomeration criteria:

$$\begin{array}{l} \text{Relative Kinetic Energy} \\ \text{of Colliding Particles} \end{array} < \begin{array}{l} \text{Potential for Dissipation of the} \\ \text{Kinetic Energy due to Agglomeration} \end{array} \quad (14)$$

The relative kinetic energy of two colliding particles may be calculated from their velocities as -

$$\frac{1}{2} \frac{m_1 m_2}{m_1 + m_2} (v_1 - v_2)^2$$

where  $m_1$  and  $m_2$  are the masses of two particles with velocities  $v_1$  and  $v_2$ , respectively. (See the Appendix.) To calculate the potential of two particles for energy dissipation, the thickness of the molten layer (i.e., the layer with temperature higher than melting point) is denoted as  $\delta$  and may be calculated from the temperature distribution inside a particle at any location in the jet. We may write:

$$\text{Potential for Energy Dissipation} = 3\pi\mu_k |v_1 - v_2| \left( \frac{\delta_1 + \delta_2}{2} \right)^2 \quad (15)$$

where  $\mu_k$  is the viscosity of the molten layer and  $\delta_1$  and  $\delta_2$  are the thicknesses of molten layers on the surface of the two particles. (See the Appendix.) The criterion for agglomeration thus becomes:

$$\frac{1}{2} \frac{m_1 m_2}{m_1 + m_2} |v_1 - v_2| < 3\pi\mu_k \left( \frac{\delta_1 + \delta_2}{2} \right)^2 \quad (16)$$

Agglomeration Kinetics. In our agglomeration model, all particles are assumed to be spherical and have the same density. Agglomerates are formed by the collision of a pair of sticky particles. The volume number density  $n(I)$ , is defined as the number of size I particles per unit volume. The collision frequency between two particles of sizes I and J is proportional to their volume number densities and may be written as:

$$\left( \begin{array}{c} \text{Frequency of Collision} \\ \text{Between Particle Sizes I and J} \end{array} \right) = \beta_{I,J} n(I) n(J) \quad (17)$$

where  $\beta$  is the collision frequency constant. The agglomeration rate between size I particles and size J particles is expressed as:

$$R_{I,J} = P^* \beta_{I,J} n(I) n(J) \quad (18)$$

The volume number densities  $n(I)$  and  $n(J)$  may be expressed as:

$$n(I) = E_I N(I) \quad (19)$$

$$n(J) = E_J N(J) \quad (20)$$

where  $E_I$  and  $E_J$  are the coefficients of entrainment of particle sizes I and J into the jet. It is assumed that the size distribution of particles in the jet dilute phase remains the same as that in the fluidized bed. Therefore, the coefficients of entrainment for all particle sizes into the jet should be equal, as:

$$E_I = E_J = E \quad (21)$$

The agglomeration rate  $R_{I,J}$  may be written as:

$$R_{I,J} = P^* \beta_{I,J} E^2 N(I)N(J) \quad (22)$$

Comparing Equation 22 with Equation 2, the agglomeration rate constant may be written as:

$$K_{I,J} = P^* \beta_{I,J} E^2 \quad (23)$$

As previously mentioned,  $K_{I,J}$  can be represented by a multiple of two functions; one dependent on operating conditions and the other on size:

$$K_{I,J} = k_{op} (d_I^4 + d_J^4) \left( \frac{1}{d_I^3} + \frac{1}{d_J^3} \right) \quad (24)$$

The value of collision frequency constant  $\beta$  depends on the size of the colliding particles. If  $\beta$  dependency on particle size can be expressed with the same function as that for the agglomeration rate constant,

$$\beta_{I,J} = \beta' (d_I^4 + d_J^4) \left( \frac{1}{d_I^3} + \frac{1}{d_J^3} \right) \quad (25)$$

and we may then write:

$$k_{op} = P^* \beta' E^2 \quad (26)$$

The probability  $P^*$  in Equation 26 is the fraction of all the collisions that meet the agglomeration criteria in Equation 14. This probability is calculated by defining  $\xi$  as follows:

$$\xi = \begin{cases} 1 & \text{if two particles of size I and J meet the agglomeration criteria} \\ 0 & \text{if two particles of size I and J do not meet the agglomeration criteria} \end{cases}$$

The value of  $P^*$  is calculated as the number of collisions for which  $\xi = 1$  divided by the total number of collisions.

$\beta^2 E^2$  depends mainly on the gas and solid flow behavior in the fluidized bed. Our studies indicate that, for the runs with the same jet nozzle diameter and jet air velocity and approximately the same particle-size distribution,  $\beta^2 E^2$  has approximately the same value.

**Results and Discussion.** The values of  $k_{op}$  were calculated for different jet and fluidizing air temperatures at constant jet nozzle diameter, jet and fluidizing air velocities, and feed particle-size distribution using Equation 26 with the value of  $\beta^2 E^2$  set equal to  $1.35 \times 10^{-5}$ . This value of  $\beta^2 E^2$  was chosen so that the value of  $k_{op}$  evaluated from experimental data agreed with that calculated from the model, for the run conducted at the jet air temperature of  $144.4^\circ\text{C}$  and fluidizing air temperature of  $115.7^\circ\text{C}$ . The values of  $k_{op}$  calculated for other jet temperatures are shown in Table 2 which agree well with the values from the experimental data. The predicted values of  $k_{op}$  for different fluidizing air temperatures while maintaining constant jet temperature compare reasonably well with the experimental values (Table 3).

Table 2. THE PREDICTED VALUES OF  $k_{op}$  AT DIFFERENT JET TEMPERATURES AND A FLUIDIZING AIR TEMPERATURE OF  $115.7^\circ\text{C}$

Jet Temp, $^\circ\text{C}$	144.4	143.3	142.8	142.2
$k_{op}$ From Model	$1.78 \times 10^{-9}$	$1.20 \times 10^{-9}$	$0.89 \times 10^{-9}$	$0.63 \times 10^{-9}$
$k_{op}$ From Experiment	$1.78 \times 10^{-9}$	$1.20 \times 10^{-9}$	$0.90 \times 10^{-9}$	$0.45 \times 10^{-9}$

Table 3. THE PREDICTED VALUES OF  $k_{op}$  AT DIFFERENT FLUIDIZING AIR TEMPERATURES AND A JET TEMPERATURE OF  $144.4^\circ\text{C}$

Fluidizing Air Temp, $^\circ\text{C}$	115.7	104.6	93.5	82.3
$k_{op}$ From Model	$1.78 \times 10^{-9}$	$1.15 \times 10^{-9}$	$0.68 \times 10^{-9}$	$0.54 \times 10^{-9}$
$k_{op}$ From Experiment	$1.78 \times 10^{-9}$	$1.05 \times 10^{-9}$	$0.84 \times 10^{-9}$	$0.66 \times 10^{-9}$

#### REFERENCES

1. Arastoopour, H., Huang, C. S. and Weil, S. A., "Fluidization Behavior of Sticky Particles," Journal of Fine Particle Society (1986).
2. Arastoopour, H., Gu, A. Z. and Weil, S. A., "The Effect of Gas Distributors on the Agglomeration Process in Fluidized Beds," in the Proceedings of the 4th International Symposium on Agglomeration, 443-450, 1985.



3. Arastoopour, H., Weil, S. A., Huang, C. S. and Gu, A. Z., "A Fundamental Study in Support of the Understanding of the Agglomeration of Coal in Coal Gasifiers," in the Proceedings of the 20th Intersociety Energy Conversion Engineering Conference, Vol. 1, 1625-1630, 1985.
4. Gluckman, M. J., Yerushalmi, J. and Squire, A. M., "Defluidization Characteristics of Sticky or Agglomerating Beds," Fluidization Technology, Keairns, D., Ed., 2, 395 (1976).
5. Vora, M. K., Sandstrom, W. A. and Rehmat, A. G., "Ash Agglomeration in the Fluidized Bed." Paper presented at the Sixth National Conference on Energy and the Environment, Pittsburgh, May 21-24, 1979.
6. Hariri, H., Rehmat, A. and Arastoopour, H., "Temperature Distribution in a Fluidized Bed With a Central Jet." Paper presented at the A.I.Ch.E. Annual Meeting, New York, November 15-20, 1987.
7. Ricou, F. P. and Spalding, D. B., "Measurement of Entrainment by Axisymmetrical Turbulent Jets," Journal of Fluid Mechanics 11, 21-32 (1961).
8. Tatterson, D. C., Marker, T. L. and Forgacs, J. M., "Particle Effects on Free Jet Entrainment," The Canadian Journal of Chemical Engineering, 65:361-365 (1987).
9. Bird, R. B., Stewart, W. E. and Lightfoot, E. N., Transport Phenomena. New York: John Wiley & Sons, 1960.

#### APPENDIX

##### Relative Kinetic Energy of Colliding Particles

The compression action between the two collinear-colliding particles will keep on until the relative velocity between these two particles is zero. At this point, the deformation is at the maximum, as is the contact area between the two particles. However, the sum of the kinetic energies of the two particles reaches a minimum. This can be proved using the momentum balances for the collinear-colliding particles. The difference between the sum of the kinetic energies of the two particles before collision and that of the two particles at maximum deformation can be derived using the following assumptions. Assume that the velocities of two particles before collision with mass  $m_1$  and  $m_2$  are  $v_1$  and  $v_2$ , respectively. ( $v_1$  and  $v_2$  are collinear.) If the maximum deformation is achieved, these two particles will have the same velocity,  $v'$ . The momentum balance may be written as:

$$m_1 v_1 + m_2 v_2 = (m_1 + m_2) v'$$

The difference of the kinetic energies in these two states is:

$$\begin{aligned} & \frac{1}{2} m_1 v_1^2 + \frac{1}{2} m_2 v_2^2 - \frac{1}{2} (m_1 + m_2) v'^2 = \frac{1}{2} m_1 v_1^2 \\ & + \frac{1}{2} m_2 v_2^2 - \frac{1}{2} (m_1 + m_2) \left( \frac{m_1 v_1 + m_2 v_2}{m_1 + m_2} \right)^2 = \frac{1}{2} \frac{m_1 m_2}{m_1 + m_2} (v_1 - v_2)^2 > 0 \end{aligned}$$

##### Potential For Energy Dissipation in Particles

The potential dissipation capability is associated with the viscous dissipation of molten material on the surfaces of the colliding particles. The molten material is caused to flow relative to the surface mainly by the sudden particle velocity change and the compression action between particles during collision and, to a much

smaller degree, by the action of surface tension. As a first estimate, the flow of the molten layer is approximated by the viscous fluid (the creeping flow) over the spherical particles. Thus, the drag force exerted on the particles is calculated from the following equations (9).

$$F_n = \int_0^{2\pi} \int_0^\theta \left( \frac{3}{2} \frac{\mu_\ell v}{R} \cos^2 \theta' \right) R^2 \sin \theta' d\theta' d\phi = \pi \mu_\ell v R (1 - \cos^3 \theta)$$

$$F_t = \int_0^{2\pi} \int_0^\theta \left( \frac{3}{2} \frac{\mu_\ell v}{R} \sin^2 \theta' \right) R^2 \sin \theta' d\theta' d\phi = \pi \mu_\ell v R (2 - 3 \cos \theta + \cos^3 \theta)$$

where  $F_n$  and  $F_t$  are the summations of the projections of normal and tangential forces exerting on hard-core surface in the direction opposite to the particle flow direction.  $v$  is the characteristic velocity of the melted layer relative to the particle hard core.  $\mu_\ell$  is the viscosity of the melted material.

$$F_n + F_t = 3\pi \mu_\ell v R (1 - \cos \theta) = 3\pi \mu_\ell v R \frac{(\delta_1 + \delta_2)}{2R} = 3\pi \mu_\ell v \left( \frac{\delta_1 + \delta_2}{2} \right)$$

If the thicknesses of the melted layers are  $\delta_1$  and  $\delta_2$ , respectively, the energy dissipated due to viscous flow can be approximated as the product of force exerted on the particle hard core and the relative distance traveled between them.

$$\text{Potential Dissipation Capability} = (F_n + F_t) \times (\delta_1 + \delta_2) = 6\pi \mu_\ell v \left( \frac{\delta_1 + \delta_2}{2} \right)^2$$

It is further assumed that  $v$  is equal to the half of the relative velocity  $|v_1 - v_2|$  before particle collision; thus:

$$\text{Potential Dissipation Capability} = 3\pi \mu_\ell |v_1 - v_2| \left( \frac{\delta_1 + \delta_2}{2} \right)^2$$

#### ACKNOWLEDGMENT

This work was sponsored by the U.S. Department of Energy under Contract No. DE-AC21-87MC23283.

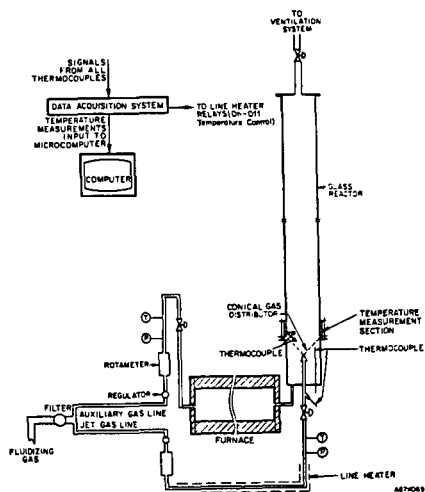


Figure 1. SCHEMATIC DIAGRAM OF THE EXPERIMENTAL SETUP

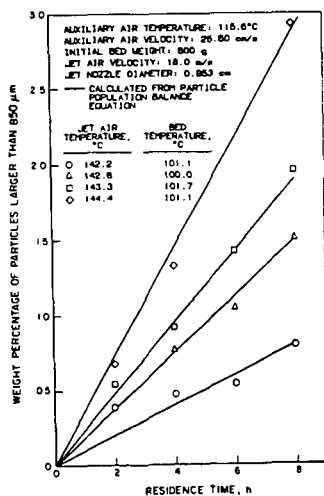


Figure 2. COMPARISON OF WEIGHT PERCENTAGES OF PARTICLES LARGER THAN 850  $\mu\text{m}$  CALCULATED FROM THE PARTICLES' POPULATION BALANCE EQUATION AND EXPERIMENTAL DATA AT FOUR DIFFERENT JET AIR TEMPERATURES

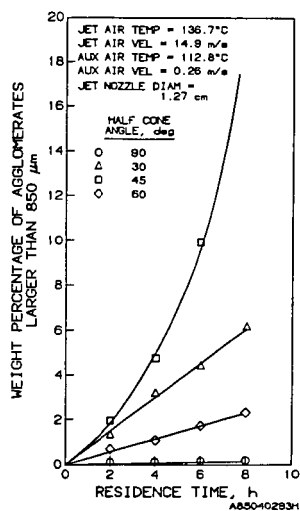


Figure 3. COMPARISON OF WEIGHT PERCENTAGES OF AGGLOMERATES WITH FOUR DIFFERENT CONE ANGLE GAS DISTRIBUTORS

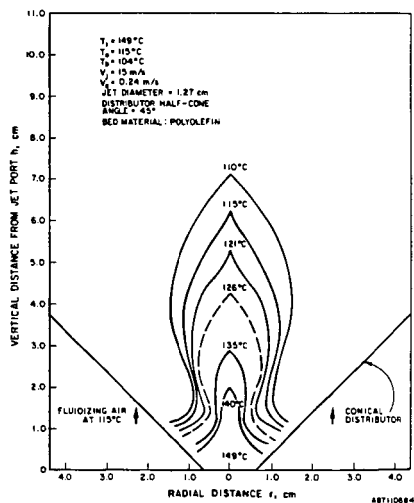


Figure 4. JET ZONE ISOTHERMS IN A FLUIDIZED BED AT A JET AIR TEMPERATURE OF 149°C AND A FLUIDIZING AIR TEMPERATURE OF 115°C

## Numerical Study of Coal Dust Explosions in Spherical Vessels

G. Continillo\*

School of Engineering  
University of California, Irvine  
Irvine, California 92717

The unsteady flame propagation through a coal dust-air suspension in a spherical enclosure is studied by means of a one-dimensional, spherically-symmetric mathematical model. An Eulerian formulation is adopted for the gas phase mass continuity, species and energy balance equations, while a Lagrangian formulation is employed for the mass, energy and momentum balance equations for the particles. The pressure is assumed to be uniform in space (low Mach number) but varies in time. Preliminary calculations have been performed with a very simple coal particle submodel, in which a single-step devolatilization reaction with Arrhenius-type kinetics and quasi-steady heat, mass and momentum transfer to/from the particles is considered. Coal dust-air flame propagation could be predicted on the basis of devolatilization and homogeneous combustion reaction only. The model can represent a useful framework for the development and validation of particle-scale models, to be implemented in more complex coal combustion situations.

### INTRODUCTION

The occurrence of dust explosions can be reconducted to the ability of a dust suspension to be ignited and to sustain a flame front propagating through it. To study the behavior of such systems is a difficult task due to the complex chemical and transport phenomena involved both in accidental explosions and in the controlled combustion of pulverized fuels. A look at the literature on dust explosions reveals substantial disagreement between the experimental results of the various authors, as pointed out by Hertzberg et al. (1). No comprehensive theory is available to explain the phenomenon and arguments are still being made about which is the dominant mechanism. In fact, the flame propagation through a flammable dust cloud can be predicted on the basis of different and even mutually excluding simplified models. For example, Essenhigh and Csaba (2) presented a model of coal dust flame propagation based on the incoming radiating heat from the walls to the particles, neglecting any other form of heat transfer and even the contribution of the combustion reaction. On the other hand, Smoot (3) proposed a coal dust flame model in which the conductive heat transfer is assumed to be the dominant mechanism. However, the experimental situations are still too complicated to be modelled in full detail, thus making quantitative comparison between experiment and theory almost impossible. The ignition and flame propagation in a cold dust suspension requires heat to be transferred from the burning mixture to the neighboring fresh mixture. Mitsui and Tanaka (4) modelled the propagation of a flame in an idealized cloud of particles. The ignition of a particle was assumed to take place at the surface, by heterogeneous combustion, as in Cassel and Liebman (5). Once ignited, an envelope flame was assumed to establish, due to the devolatilization, at a certain somewhat arbitrary distance from the surface and with a certain assigned flame temperature; then the unsteady spherically symmetric heat conduction equation was solved to calculate the temperature in the gas phase surrounding the burning particle. Flame propagation was stated to be possible when the temperature at the location of the adjacent particle reached the ignition temperature before than the envelope flame

\* On leave from: Istituto Ricerche sulla Combustione, Consiglio Nazionale delle Ricerche, Naples, Italy

extinguished for the volatile fuel consumption of the first particle. This idealized situation is still amenable of analytical treatment; particle-air relative motion, density and pressure variation, unsteady particle heat up and pyrolysis cannot be introduced without making the analytical solution impossible.

When a numerical solution is considered, the model can be complicated almost unlimitedly. The literature shows that the tendency has been either to refine the model for a single particle, with a very idealized environmental situation (for example Kansa and Perlee (6)) or to study very complicated flow situations like industrial burners, as in the works reviewed by Smoot (7). Both these approaches do not offer a direct contribution to the understanding of the dominant mechanisms of flame propagation in dust explosions, the first because of the poor or non-existing consideration of the particle-gas and particle-particle interactions, the second because of the impossibility of giving a close description of the particle scale phenomena at the same time of describing large scale, complicated flow and heat transfer patterns.

Aim of the present work is to identify a model problem in which the parameters are not too many, and fairly controllable, with a simple geometry and flow field, so that more computational efforts can be devoted to the microscale phenomena. The problem is meant to be still representative of a conceivable practical situation, like the deflagration in a spherical enclosure. The framework is presented in this paper, and preliminary calculations, with the inclusion of a simplified model for the unsteady particle heat-up and pyrolysis, are performed. Some of the results are shown and discussed, and further developments are indicated in the foregoing.

#### MATHEMATICAL FORMULATION

**Gas Phase Model.** The gas phase model is essentially that of Reference (8), in which liquid spray flames were investigated. The following main assumptions are made. The flow is one-dimensional, unsteady, laminar, spherically symmetric. The viscous dissipation rate is negligible and the pressure is constant along the space coordinate (low Mach number), but varies in time due to the confinement in the vessel. The gas mixture is thermally perfect. Binary diffusion coefficients for each pair of species are taken to be equal, thermal mass diffusion is neglected. Mass diffusion and heat conduction are governed by Fick's and Fourier's law, respectively. The diffusion coefficient is assumed to vary with temperature and pressure ( $\rho D = \mu_0 = \text{constant}$ ). The Lewis number is unity. Radiative heat transfer is neglected. The combustion chemistry is described by means of a single-step, irreversible reaction of the volatiles with the oxygen; Arrhenius-type kinetics with non-unity exponents for fuel and oxygen concentrations, as proposed by Westbrook and Dryer (9), is included. The equations include coupling terms accounting for mass, momentum and energy exchanges between the two phases.

The dimensional unknown quantities and the variable physical parameters are nondimensionalized with respect to their initial values, except that for the velocity. The following reference quantities are defined:  $r_c = R$ ;  $t_c = R^2/D_0$ ;  $u_c = D_0/R$ , where  $r$  is the space coordinate,  $R$  is the radius of the enclosure,  $t$  is the time coordinate,  $D_0$  is the diffusion coefficient at a reference temperature,  $u$  is the gas velocity; furthermore, the nondimensional number density of the  $(k)$ th particle group  $n_k = n_k^0 R^3$ , the nondimensional heat of combustion  $Q = Q^0/C_p T_0$  and mass production rate for the  $(i)$ th species  $\dot{w}_i = \dot{w}_i^0 (R^3/\rho_0 D_0)$  are defined, where  $\rho_0$  is the gas density evaluated at the initial temperature and pressure, and the following nondimensional equations are derived.

Continuity:

$$\frac{\partial \rho}{\partial t} + \frac{1}{r^2} \frac{\partial}{\partial r} (r^2 \rho u) = - \sum_{k=1}^N n_k \dot{m}_k \quad 1)$$

where  $\dot{m}_k$  is the mass devolatilization rate of the (k)th particle group, N is the total number of particle groups.

Species:

$$\rho \frac{\partial Y_j}{\partial t} + \rho u \frac{\partial Y_j}{\partial r} - \frac{1}{r^2} \frac{\partial}{\partial r} (r^2 \frac{\partial Y_j}{\partial r}) = (\delta_{jF} - Y_j) \sum_{k=1}^N n_k \dot{m}_k + \dot{w}_j \quad 2)$$

where  $Y_j$  is the (j)th species mass fraction,  $\delta$  is the Kroneker delta, and the subscript F stays for "vapor fuel."

Energy:

$$\rho \frac{\partial \phi}{\partial t} + \rho u \frac{\partial \phi}{\partial r} - \frac{1}{r^2} \frac{\partial}{\partial r} (r^2 \frac{\partial \phi}{\partial r}) = - \frac{p}{C_p} \left( \frac{C_p T}{C_{p0} T_0} \right) \sum_{k=1}^N n_k \dot{q}_k + Q \dot{w}_F \quad 3)$$

with

$$\phi = T p^{\frac{1-\gamma}{\gamma}} = T p^{\Gamma}$$

where p is the pressure,  $C_p$  is the specific heat at constant pressure, T is the temperature, the subscript p stays for "particle", and  $\dot{q}_k$  is the heat flux coming from one particle belonging to the (k)th group (usually negative), whose expression will be given later.

Ideal gas state equation:

$$p = \rho T \quad 4)$$

Velocity (integrating Eq. 1 over  $r^2 dr$ ) is given by:

$$u = \frac{1}{r^2} \int_0^r \left( \sum_{k=1}^N n_k \dot{m}_k - \frac{\partial \rho}{\partial t} \right) r^2 dr \quad 5)$$

Pressure (integrating Eq. 1 over  $r^2 dr$  between 0 and R) is given by:

$$\left[ \int_0^1 \frac{r^2 dr}{T} \right] \frac{dp}{dt} + \left[ \frac{\partial}{\partial t} \int_0^1 \frac{r^2 dr}{T} \right] p = \int_0^1 \sum_{k=1}^N n_k \dot{m}_k r^2 dr \quad 6)$$

The initial and boundary conditions for the gas phase are:

$$Y_j(r, 0) = Y_{j0} ; \quad u(r, 0) = 0 ; \quad \phi(r, 0) = 1 ; \quad p(0) = 1 \quad 7)$$

$$\left. \frac{\partial Y_j}{\partial r} \right|_{r=0} = 0 ; \quad \left. \frac{\partial Y_j}{\partial r} \right|_{r=1} = 0 ; \quad \left. \frac{\partial T}{\partial r} \right|_{r=0} = 0 ; \quad \left. \frac{\partial T}{\partial r} \right|_{r=1} = 0 \quad 8)$$

$$u(0, t) = u(1, t) = 0$$

**Particle Model.** In the calculations presented in this paper, the transient behavior of a particle is described by means of an extremely simplified model. The coal particle is represented by a sphere of solid material (ashes and fixed carbon) and volatiles in a specified initial partition. The particle is

considered to remain spherical and conserve its volume. The temperature is considered uniform in the particle and on the particle surface. Following Hubbard et al. (10), the transport processes next to the particle (in the "film") are assumed to be quasi-steady, and the thermophysical properties of the air-fuel vapor mixture are assumed uniform and evaluated at a conveniently averaged value of the temperature in the film. The fuel vapor production rate is assumed to depend on the particle temperature and global composition only. During the particle heat-up, the volatiles are released according to a simple one-step Arrhenius pyrolysis reaction, as in (6). The surface oxidation reaction is not considered, due to the highly transient character of the particle history in this kind of phenomena. This eliminates the need for considering the mass transfer processes in the film: all of the volatiles released by the particle are immediately available in the gas phase. The model accounts for the effects of the convective transport caused by the gas-particle relative motion by means of correction factors to the spherically symmetric stagnant film situation.

The non-dimensional equations for each particle group are:

Volatiles:

$$\frac{dm_v}{dt} = -A_v \exp(-T_v/T_p) m_v \quad (9)$$

where  $m_v$  is the mass of volatiles,  $A_v = A'_v R^2/D_0$  is a non dimensional preexponential factor,  $T_v$  is a non dimensional activation temperature.

Momentum:

$$\frac{dv}{dt} = \frac{N_1}{8} \text{Re} C_D (u - v) \frac{\rho_\infty}{\rho_p} \quad (10)$$

$$\text{with } N_1 = \frac{3}{2} \frac{R^2}{a^2} \quad \text{and (11): } C_D = \frac{24}{\text{Re}} \left(1 + \frac{1}{6} \text{Re}^{2/3}\right) \quad (11)$$

where  $v$  is the particle velocity,  $\text{Re}$  is the Reynolds number, the subscript  $\infty$  stays for "free stream conditions" referring to a particle,  $a$  is the radius of the particle.

Energy:

$$\frac{dT_p}{dt} = N_1 \frac{C_p}{C_{pp}} \text{Nu} (T_\infty - T_p) \frac{\rho_\infty}{\rho_p} \quad (12)$$

$$\text{with (12)} \quad \text{Nu} = 2 + 0.6 \text{Re}^{1/2} \text{Pr}^{1/3} \quad (13)$$

where  $\text{Pr}$  is the Prandtl number. The instantaneous position of particle group  $k$  is given by

$$\frac{dr_k}{dt} = v_k \quad (14)$$

The free-stream values of temperature and velocity are those of the gas phase model equations, evaluated at the current particle location. Finally, for the source terms in Eqs. 1, 2, and 3, we have:

$$\dot{m}_k = -\left(\frac{dm_v}{dt}\right)_k \quad (15)$$

$$\dot{q}_k = \frac{C_{po}}{C_{pp}} \left[ 3 \frac{\rho_o}{\rho_{po}} \frac{R^2}{a^2} \text{Nu} + \beta_{v,k} \dot{m}_k C_p \right] (T_{pk} - T) \quad (16)$$



where  $\rho_{po}$  is the initial density of the particle, and  $\beta_v = \rho_{vo}/\rho_{po}$  is the initial mass fraction of volatiles in the particles.

For the numerical solution, gas phase and particle calculations are time-split. The source terms provided by the particle calculations for the (n)th time level are used in the (n + 1)th time level of the gas phase calculations, after proper interpolation, and so forth. Explicit finite difference schemes are employed to discretize the PDEs of the gas phase model - except that for the chemical production terms, for which a degree of implicitness is introduced - since they have been proved to be the most effective in such two-phase problems (13). A non-uniform spatial grid is used, with the finest mesh size next to the wall. The time step is dynamically changed in order to describe the evolution of the system according to the current time scale. Due to the coupling of the equations, the calculations are iterated within each time step until the desired level of convergence is achieved. Then the integration in time is continued until desired.

## RESULTS AND DISCUSSION

Ignition is achieved by means of a heat source in the energy equation, in a spherical region for a limited time and an assigned intensity. The model predicts the particle heat-up, the devolatilization and the ignition of the volatiles in the gas phase, and the flame propagates through all the volume. The values of the parameters used for the base case are listed in Table I.

Table I.

Values and Expressions Used for the Most Important Physical Parameters in the Base Case

a	- $2.5 \times 10^{-5} \text{ m}$	R	- $5 \times 10^{-2} \text{ m}$
$A_v$	- $1. \times 10^7 \text{ s}^{-1}$	$T_o$	- $3 \times 10^2 \text{ K}$
$C_p$	- $1.01 \times 10^3 + 1.95 \times 10^{-1} (T' - 300) \text{ J/KgK}$	$T_v$	- $15000/R \text{ K}$
$m_{vo}/m_{po}$	- 0.25	$\gamma$	- $C_p/(C_p - R)$
$P_o$	- $1 \times 10^5 \text{ Pa}$	$\mu_o$	- $1.845 \times 10^{-5} \text{ Kg/ms}$
Q	- $4.421 \times 10^7 \text{ J/Kg}$	$\rho_{po}$	- $1.36 \times 10^3 \text{ Kg/m}^3$

Figure 1 shows the computed pressure-time patterns for different particle diameters. The predicted final pressure, close to the maximum theoretical adiabatic pressure achievable, is much higher than that found in the experiments. The reasons are that the model does not account for heat losses, nor for the endothermic dissociation in the burned mixture. A slight decrease is observed after the maximum, and this accounts for the cooling effect due to the residual solid particles. During the combustion, the rate of pressure rise is always increasing: this is in agreement with predictions of lumped parameter models and with results of the experiments for the part in which the heat losses are negligible (14). In fact, it has been shown by means of a two-zone, thin flame model (14) that the rate of pressure rise can be expressed as

$$\frac{dp}{dt} = \frac{3\gamma p}{R} \frac{Q_R}{C_v T_u} \left( \frac{r_f}{R} \right)^2 s_u \quad (17)$$

where  $Q_R$  is the heat of reaction per unit mass of gas,  $C_v$  is the specific heat at constant volume,  $T_u$  is the temperature of the unburned mixture,  $r_f$  is the current radial location of the flame, and  $S_u$  is a flame speed with respect to the unburned mixture. For Equation 17 all the information connected with the flame structure is included (and hidden) in the parameter  $S_u$ , like the transport phenomena, the combustion reaction rate, the particle-gas interactions (relative motion, thermal inertia of the condensed phase), the rate of pyrolysis. A distributed-parameters model like that of the present work is capable of resolving the flame structure, therefore it allows for an appreciation of the different behavior of dust suspensions for what all of the parameters in Eq. 17 are equal, except  $S_u$ . For example, the influence of the particle size is clearly seen in Fig. 1, where finer particles are shown to give rise to faster flame propagation. Figure 2 illustrates the influence of another parameter, namely the oxygen content of the suspending atmosphere; the initial solid concentration is chosen accordingly to be slightly more than stoichiometric, in order to avoid the presence of oxygen in the residual gases together with the residual solid particles, which would require the consideration of the solid-gas surface oxidation reaction, not included in the model at present. The maximum pressure obviously decreases with the content of reactants, since the total amount of heat released by the combustion reaction is lower; the duration of the explosion increases, the system showing a lower overall reactivity, as expected.

Figure 3 represents the spatial profiles of the main variables at successive times for the base case. Each circle represents one particle group, whose particles are distributed on a spherical surface: the abscissa of each one represents the current radial location, while the ordinate corresponds to the particle temperature, in the same scale as that of the gas temperature. The radius of the internal filled circle is proportional to the remaining fraction of volatiles. The ignition zone is rapidly heated to about 1500 K, while the particles remain at a temperature close to the initial. The heat provided by the ignition source is conducted towards the outer region, and to the particles in the ignition region, until they begin to pyrolyze. Note that the particles have a tendency to spread out, due to the motion impressed by the expanding gas during the ignition energy supply. This causes a local decrease of the volumetric concentration of dust, but the gas concentration has, of course, become even lower due to thermal expansion, therefore the overall effect is that of the generation of a locally fuel-rich region. When the vapor fuel released is sufficient, individual flames set up at the location of the particles, where the oxygen is seen to be consumed, and peaks in the temperature profiles appear. During the propagation of the flame, it is seen that the vapor fuel is present in the burned region only, meaning that it reacts as soon as it is generated. In fact the gas temperature is much higher than that of the particles when they begin to pyrolyze, up to the point that the combustion reaction is much faster than the pyrolysis, notwithstanding the much higher activation energy and the low concentration of the fuel vapor. Therefore, the limiting stage is the pyrolysis in this case. The relative motion of the two phases generates a deviation from the initially uniform, slightly richer than stoichiometric, equivalence ratio. More precisely, at the beginning the gas velocity is mainly directed towards the wall, and the particles, due to their kinematic inertia, do not follow the gas with the same velocity, thus creating a locally richer mixture in the center. The system is closed, thus a locally lean mixture is being generated in the zones encountered by the flame going towards the wall. When the flame approaches the wall, the gas velocity is mainly directed towards the center, while the particles are still moving towards the wall, and this generates a locally rich mixture next to the wall. As a result of the phenomenon, an uneven residual fuel vapor distribution is found at the end of the propagation.

## CONCLUSIONS

A model problem for ignition and unsteady flame propagation in a coal dust-air suspension has been identified. The simple geometry and flow field allow for

more details to be included in the modelling of the microscale phenomena. The problem can be considered still representative of a practical situation like a deflagration in a spherical enclosure. Results obtained with the inclusion of a simplified model for the unsteady particle heat-up and pyrolysis have been presented and discussed, and qualitative agreement with experimental evidence and simpler theoretical approaches has been found. Coal dust-air flame propagation has been predicted on the basis of devolatilization and homogeneous combustion reaction only, although the range of variation of some parameters is currently limited by the approximations made in the simplified coal particle model. It has been demonstrated that the model can represent a useful framework for the development and validation of much more detailed particle-scale models, to be implemented in more complex coal combustion situations.

#### Acknowledgments

This work has been partly supported by the Consiglio Nazionale delle Ricerche, Italy, with a NATO-CNR scholarship for exchange visitors granted to the author. Professor William A. Sirignano is gratefully acknowledged for his kind hospitality, support and advice.

#### References

1. Hertzberg, M., Cashdollar, K.L., Opferman, J.J., "The Flammability of Coal Dust - Air Mixtures," Bureau of Mines, RI 8360 (1979).
2. Essenhigh, R.H., Csaba, J., Ninth Symp. (Int.) on Combustion, p. 111, The Combustion Institute, Pittsburgh, 1963.
3. Smoot, L.D., Horton, M.D., Prog. Energy Combust. Sci. 3, 235 (1977).
4. Mitsui, R., Tanaka, T., Ind. Chem. Eng. Process Des. Develop. 12, 384 (1973).
5. Cassel, M., Liebman, I., Combust. Flame, 3, 467 (1959).
6. Kansa, E.J., Perlee, H.E., Combust. Flame 38, 17 (1980).
7. Smoot, L.D., Prog. Energy Combust. Sci. 10, 229 (1984).
8. Continillo, G. and Sirignano, W.A., submitted to the Twenty-Second International Symposium on Combustion, Seattle, 1988.
9. Westbrook, C.K., Dryer, F.L., Prog. Energy Combust. Sci. 10, 1 (1984).
10. Hubbard, G.L., Denny, V.E., Mills, A.F., Int. J. Heat Mass Transfer 18, 1003 (1975).
11. Faeth, G.M., Prog. Energy Combust. Sci. 3, 191 (1977).
12. Ranz, W.E., Marshall, W.R., Jr., Chem. Eng. Prog. 48, 141 (1952).
13. Aggarwal, S.K., Fix, G.F., Lee, D.N., Sirignano, W.A., J. Comput. Phys. 35, 229 (1983).
14. Continillo, G., Study on Coal Dust Explosibility in Spherical Vessels, Doctoral Thesis, University of Naples, Naples, Italy, 1987 (in Italian).

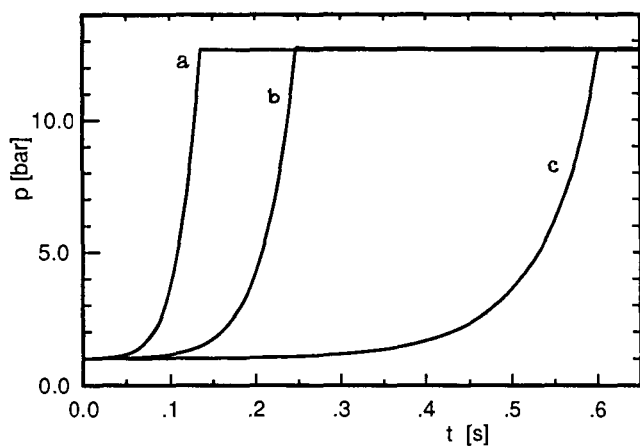


Figure 1. Pressure-time patterns at various particle diameters:  
a) 30  $\mu\text{m}$ ; b) 50  $\mu\text{m}$  (base case); c) 100  $\mu\text{m}$ ;

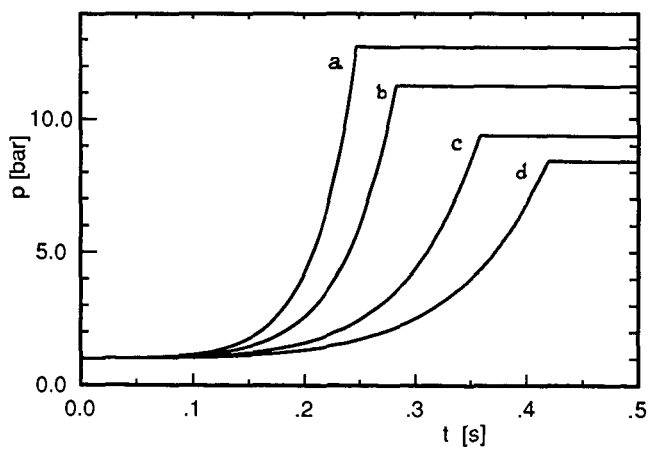


Figure 2. Pressure-time patterns at various oxygen mass fractions in the suspending atmosphere: a) 23.2% (base case); b) 20%; c) 16%, d) 14%

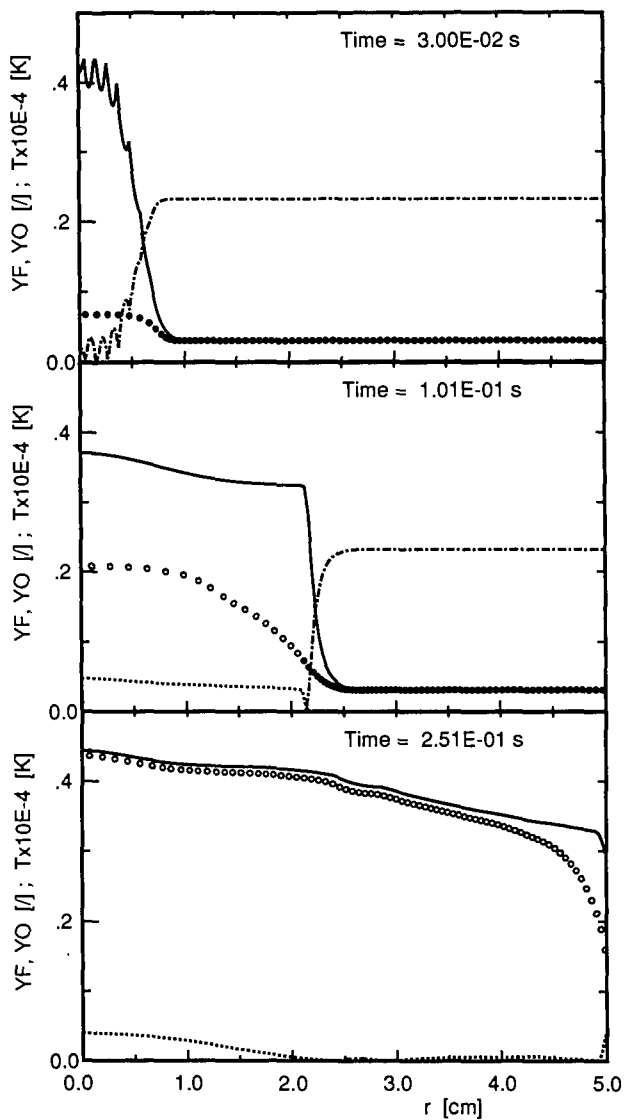


Figure 3. Radial profiles of fuel ( $Y_F$ , dashed) and oxygen ( $Y_O$ , dot and dash) mass fractions, and of temperature ( $T$ , solid line) at successive times.

# AN EQUILIBRIUM-THERMODYNAMIC ANALYSIS OF SULFUR RELEASE AND CAPTURE IN A GASIFICATION/COMBUSTION ENVIRONMENT

R. Nagarajan

Department of Mechanical and Aerospace Engineering  
West Virginia University, Morgantown, West Virginia 26506-6101

and

M.R. Khan, H.N. Pham, R.J. Anderson, and L.C. Headley  
U.S. Department of Energy-Morgantown Energy Technology Center  
Morgantown, West Virginia 26507-0880

## ABSTRACT

Coal and coal-derived liquids and gases constitute an economically attractive alternative energy source to liquid petroleum fuels. Ongoing research programs at DOE-METC are currently examining the potential of inexpensive production of clean liquid and solid fuels from coal by mild gasification, and of gaseous fuels by countercurrent pressurized fixed-bed gasification. The simultaneous release of gaseous sulfur species ( $H_2S$ ,  $COS$ ,  $SO_2$ ,  $SO_3$ ) is an inherent environmental limitation to a large-scale practical application of these processes. A computational technique to estimate the release of sulfur from coal and subsequent capture by calcium-based sorbents is presented here, where both processes are assumed to proceed to equilibrium under devolatilization, gasification (reducing), and combustion (oxidizing) conditions. A free-energy minimization computer program (PACKAGE) is used here to simulate local thermochemical equilibria in these reactive atmospheres. Predicted partial pressures of sulfur species are compared with experimental data on sulfur release and sorption, and conclusions are drawn regarding the usefulness and limitations of an equilibrium approach to modeling these processes.

## 1. INTRODUCTION

Coal use for electric power generation has increased in the past decade, and coal use for propulsion is a distinct possibility in the near future; however, the economic conversion of coal to clean fuels still remains a considerable technological challenge. Coal pyrolysis is perhaps the oldest technique for the derivation of hydrocarbon fuels from coal. In all coal conversion and utilization processes (including gasification, combustion, and liquefaction), some form of coal pyrolysis occurs. Gasification is closely related to pyrolysis in that when coal is gasified by reacting it at high temperature with steam and air, pyrolysis is the first stage of the reaction as the coal is heated to reaction temperature. Similarly, pyrolysis occurs at the first stage of combustion and in liquefaction because of the high temperatures employed when solvents are reacted with the coal.

### 1.1 Coal Devolatilization: Current Status of Modeling Efforts

The need to understand devolatilization reaction chemistry is obvious from the above discussion. Khan (1) has described the experimental procedure used to generate coal pyrolysis liquids, gases, and solids in the METC Slow Heating Rate Organic Devolatilization Reactor (SHRODR). This unit simulates, to an extent, the heating rates and residence times of the devolatilization zone of a fixed-bed gasifier. In this 500 ml fixed-bed reactor, 100 grams of coal (particle size -8 by +100 mesh) were heated to 500°C in 40 minutes and maintained at that temperature for 1 hour. Two high-volatile coals, Pittsburgh No. 8 (containing 2 weight percent sulfur) and Illinois No. 6, were tested. A sulfur sorbent,  $CaO$ , was added to the coals by direct mixing of the components. Product gases were collected and analyzed using gas chromatographs. Results demonstrated that the presence of lime significantly reduced the yield of  $H_2S$ . Total gas yield remained almost unchanged, and the yield of ( $C_1$ - $C_8$ ) hydrocarbon

gases and hydrogen increased significantly. Greater sulfur capture was seen with smaller CaO particles and at higher pyrolysis temperatures.

Typically, correlation techniques (e.g. [2,3]) are utilized to predict product yield and composition during coal devolatilization. Kinetic schemes proposed to represent the mechanism of coal pyrolysis range from two independent parallel reactions (4) to 42 reactions of 14 different functional groups in coal (5). Scaroni, et al. (6), have presented a compromise based on a hierarchy of bond energies in the coal structure. Serio, et al. (7), have reviewed available models to describe the kinetics of volatile product evolution in coal pyrolysis. All these approaches suffer to varying extents from empiricism. The degree of coal devolatilization depends on several parameters, such as coal type, heating rate, temperature, pressure, residence time at pyrolysis temperature, etc. The extent of sulfur release depends on several additional variables, such as the form of sulfur in the coal (inorganic, organic), sulfur trapped in the pyrolysis liquid, intimacy of contact between CaO and the primary products of devolatilization, etc. Given the uncertainties that unfortunately detract from any effort to describe the kinetics of these individual processes, an alternative systematic yet tractable predictive procedure to assess the products of the basic devolatilization reaction would be of immediate use.

### 1.2 Coal Gasification: Current Status of Modeling Efforts

The attractiveness of such an interim approach is reinforced by the accumulating sulfur-sorption data from the METC fixed-bed gasifier, which still await fundamental analysis. A countercurrent fixed-bed gasifier consists of four overlapping zones ([3]; Figure 1). At the top of the gasifier, the coal is dried and preheated by the exiting hot product gases. In the second zone, the coal is devolatilized and gases and tars are released. In the gasification zone, endothermic reactions occur forming carbon monoxide, carbon dioxide, water, hydrogen, and methane. Combustion of coal and oxygen occurs in the combustion zone, releasing heat to support the gasification reactions. Dry or molten ash will form in this zone depending on the maximum combustion temperature. The effects of pressure, calcium/sulfur ratio, and coal and limestone feedstock on sulfur removal efficiency have been investigated in a series of runs on the METC fixed-bed gasifier. Preliminary results indicate that sulfur capture decreases as pressure increases, and that recycle of regeneration gases to the gasifier may be required to obtain significant sulfur capture at higher pressures.

Several computer models (e.g. [3,8,9,10,11]) have been developed to simulate the chemical and physical processes that occur during steady-state gasification and hot gas cleanup. In these models, typically, carbon outlet flow and outlet gas composition and flow rate are predicted, but sulfur chemistry and the effects of additives are not included in the calculations. In addition, the finite chemical kinetic rate expressions used by these models require a knowledge of the appropriate activation energies and rate constant coefficients for various coal types. To obtain a sufficiently comprehensive reliable data base is thus a Herculean task. This problem can be circumvented to a certain extent by assuming that all chemical reactions proceed to equilibrium, but this would still require that the individual equilibrium rate constants be specified. The free-energy minimization procedure developed by White, et al. (12), is a numerically attractive alternative since it specifies no reaction paths and has been used to perform the equilibrium thermodynamic calculations presented in this report.

### 1.3 Modeling Sulfur-Lime Reaction Kinetics: Uncertain Effect of Pore Structure

The equilibrium approach is also necessitated by the lack (particularly in a fixed-bed environment) of a systematic procedure for the description of the high-pressure sorptive capacity for SO<sub>2</sub> (or H<sub>2</sub>S) removal of a given limestone (or dolomite) starting from basic physical principles and experimental information. The effect of the initial pore structure of the sorbent, structural changes during the calcination

process, accumulation of a surface char layer on the sorbent particles in their transit through the (low-temperature) devolatilization and gasification zones in a gasifier column are among the phenomena that few of the presently available kinetic models incorporate. Ideally, presently available kinetic codes (13,14) should be developed to the point where they can describe these phenomena quantitatively; but in view of the time and effort that would involve, an interim procedure that is insensitive to these microscopic-level details constitutes a feasible alternative.

These considerations have led to the conclusion that a systematic approach to describing sulfur release and sorption processes in coal conversion applications is needed at this stage, even if the approach can only yield (infinite-rate) "limiting" information on sulfur release, sulfur removal, and lime utilization. While the usefulness of the present local thermodynamic equilibrium approach would doubtless be enhanced by interfacing it with the overall material balance for any specific coal conversion application, the advancement of understanding attained with the present preliminary scheme is still considerable. In subsequent sections the fundamentals of the chemical-equilibrium algorithm used here are described, its ability to deal with the complex chemistry of coal conversion product mixtures demonstrated, and its validity evaluated by comparing predicted and measured gas/solid/liquid phase compositions in lime-treated coal process streams.

## 2. THE COMPLEX CHEMICAL EQUILIBRIUM APPROACH: METHODOLOGY

Product gas, liquid, and solid phase compositions are estimated here using an equilibrium-thermodynamic computer program on the premise that the species distribution predicted by a free-energy minimization algorithm is the one likely to prevail. Stinnett, et al. (15), have previously applied the principle of thermodynamic free-energy minimization to fossil fuel gasification processes to predict the effect of operating variables on the composition of the product gas (in the absence of a sulfur sorbent). This approach enables the estimation of the partial-pressure distribution of all sulfur-bearing species in the gas, as well as the mole fractions of the sulfur-containing species in the solid and liquid phases; the analysis is thus not limited to a few user-specified reactions and products. The utility of this method is limited only by the available thermodynamic data base and its assumption of ideal solution phases. Due to the demonstrable efficiency of the PACKAGE computer code (16) in modeling complex phase equilibria in coal conversion gas streams and cleanup devices, the PACKAGE program has been used to perform the equilibrium thermodynamic computations presented here. Input to this program consists of elemental compositions of the reactant streams, relative mass flow rates of the reactant streams (e.g., the fuel/air ratio in a combustion case,  $[\text{coal} + \text{lime}]/[\text{air} + \text{steam}]$  in a gasification situation), pressures, and temperatures of interest. In the case of coal devolatilization, coal composition, devolatilization temperature, and pressure would constitute the input parameters. Output from the PACKAGE program typically consists of phase fractions and species mole fractions within each phase as a function of temperature. The results of exercising the PACKAGE programs under conditions representative of coal devolatilization, gasification and combustion are presented in the next section.

## 3. THE COMPLEX CHEMICAL EQUILIBRIUM APPROACH: FEASIBILITY

In order to demonstrate the suitability of an equilibrium approach to characterizing coal conversion product streams, illustrative calculations have been performed over a wide range of operating conditions simulating coal devolatilization, gasification, and combustion environments. The parametric studies presented in this section are meant to constitute the operating "envelope" for these systems. The results presented here are mostly qualitative and are intended only to show the feasibility of the approach without reference to quantitative accuracy; the latter aspect will be taken up in the next section.



### 3.1 Devolatilization Products Composition Calculations

The atmospheric pressure devolatilization calculations presented here pertain to slow-heating pyrolysis of Pittsburgh No. 8 coal over a temperature range 600-1200 K. In Figures 2 and 3 the effects of temperature on sulfur release and capture during coal devolatilization are examined. Figure 2 corresponds to untreated coal, whereas Figure 3 displays calculations made for the lime-added case. Under these (fuel-rich) conditions,  $H_2S$  is the dominant sulfur-containing vapor species, with the  $CO_2$  concentration being at least an order of magnitude smaller. Both figures show increasing sulfur capture with temperature. Calcium and iron originally in the coal can capture sulfur to a limited extent, forming  $CaS$  and  $FeS$ , respectively. Sulfur sorption by iron oxide is predicted to be possible at lower temperatures than sorption by  $CaO$ , due to the fact that the calcination temperature for  $CaCO_3$  is relatively high at atmospheric pressure. Iron and calcium in the coal can recapture close to 30 percent of the released sulfur at temperatures in excess of 900 K. The effect of varying levels of added lime on  $H_2S$  mole fraction in the gas phase is shown in Figure 3 on a semi-logarithmic scale. Clearly, under devolatilization conditions, calcium oxide is potentially a very effective sorbent for  $H_2S$ ; indeed, the present equilibrium approach can, at best, indicate the maximum sorption potential of any additive and enable the evaluation of different sorbents on that basis.

### 3.2 Gasification and Combustion Products Composition Calculations

Figures 4-6 represent equilibrium-thermodynamic calculations performed under gasification conditions. These results simulate the products obtained by reacting together varying amounts of coal and moist air at atmospheric pressure, over a temperature range 500-1500 K. The liquid and solid phase fractions in the reaction product mixture are plotted as a function of temperature and coal/air flow rate ratio in Figures 4 and 5, respectively. Sulfur elemental concentration in the product gases is plotted against these variables in Figure 6; no distinction has been made in this representation of gas-phase sulfur between various sulfur-bearing vapor species (such as  $H_2S$ ,  $SO_2$ ,  $SO_3$ , etc.). With increasing temperature the liquids and solids fractions show a non-monotonic behavior for all fuel/air ratios, while the trend for sulfur elemental concentration is very sensitive to the fuel/air parameter. The condensed phases comprise principally mineral phases at higher temperatures, and sulfates and sulfides at lower temperatures. The program cannot simulate the formation of (thermodynamically unstable) liquid hydrocarbons ("tars"). In the fuel-rich case, (S) in the gas decreases slightly with temperature, as in the case of devolatilization; in the fuel-lean case,  $CaSO_4(s)$  will form at temperatures below 700 K, providing a significant "sink" for gas-phase sulfur.

The ability of the PACKAGE program to compute chemical equilibrium compositions under coal combustion conditions has been demonstrated in previous work. In the analysis of ash deposition on coal-fired gas turbine blades, the prediction of condensed liquid ("glue") phase fraction and composition constitutes the first step (17,18). In Figures 7 and 8, respectively, PACKAGE-predicted effects of added calcium on gaseous  $SO_2$  and  $SO_3$  are presented. For temperatures greater than about 1300 K (depending on the calcium level), added calcium gets bound up in high molecular weight vapor and condensed species (e.g.,  $CaAl_2Si_2O_8[s]$ ), and is thus not free to react with all the sulfur present. Unbound calcium is still sufficient, however, to absorb nearly all of the  $SO_3$ .

In this section, it has been shown that the PACKAGE equilibrium-thermodynamic computer program can estimate the product stream composition in a variety of coal conversion applications. It remains to be seen whether any of these equilibrium predictions has a basis in reality or is strictly of academic value. This concern will be addressed in the remainder of this paper.

#### 4. THE COMPLEX CHEMICAL EQUILIBRIUM APPROACH: VALIDITY

##### 4.1 Coal Devolatilization Applications

In order to assess the applicability of an equilibrium-thermodynamic procedure to estimate the coal-devolatilization product gas composition, PACKAGE predictions have been compared against in-house SHRODR measurements. Computed and detected molar concentrations of the major vapor species released during atmospheric-pressure slow-heating pyrolysis of Pittsburgh No. 8 coal are presented in Tables 1 and 2. Predicted and observed effects of CaO addition on the composition of devolatilization products are shown in Table 1. Results demonstrate that the presence of CaO during coal devolatilization significantly reduces the yield of  $H_2S$ . For example, for this Pittsburgh seam high-volatile coal, the  $H_2S$  yield was observed to be reduced from 3.7 volume percent to 0.05 volume percent when 21 weight percent of CaO (Ca:S = 6:1) was added to the coal. The equilibrium code overestimates sulfur sorption in the no-lime added case, but otherwise predicts the extent of sulfur capture with reasonable accuracy, especially when smaller lime particles are added. This accuracy is, at first, surprising because the PACKAGE program does a relatively poor job of predicting the partial pressures of the major C-H-O species. The code underestimates gas-phase hydrocarbons ( $CH_4$ ,  $C_2H_4$ ,  $C_2H_6$ , etc.) by a factor of 2-5 and CO by a factor of 2-5 (at 500°C); it overestimates  $CO_2$  by a factor of 1.5-5,  $H_2$  by a factor of about 3, and  $H_2O$  by an order of magnitude. The code also, in general, underpredicts COS formation.

These gross errors in vapor-phase representation by the PACKAGE computer program would appear to be consequences of an inadequate thermodynamic data base, as well as an inherent failure of the approach itself to model essentially non-equilibrium processes, such as tar cracking. Cracking of tar liquids (phenolic compounds in particular) to lighter products is a primary cause of increased  $CH_4$  and hydrocarbon gases ( $C_1$ - $C_8$ ) formation (1). The composition of low-temperature (< 700°C) coal tars is very complex and strongly dependent on the conditions at which pyrolysis occurs. Until a comprehensive library of the thermodynamic properties of complex tar liquid mixtures is developed, and utilized along with the equilibrium code, discrepancies between observed and predicted devolatilization product composition are bound to exist. However, the relatively error-free estimation of  $H_2S(v)$  concentration in the presence of added lime suggests that the equilibrium approach can serve as a tractable preliminary scheme for the analysis of sulfur chemistry even in the less reactive atmosphere of low-temperature devolatilization.

This tentative conclusion is strengthened by additional comparisons between predicted and observed effects of variations in coal and lime particle size, the devolatilization temperature, and the sulfur sorbent employed. Data obtained with smaller coal particles and smaller CaO particles (< 10 micrometers) reveal improved agreement between predicted and measured sulfur capture (Table 1). This suggests that a better mixture of coal and CaO components (and, hence, greater contact between CaO and devolatilized sulfur products) is possible when the smaller size fraction is utilized. This increased intimacy of contact also implies closer approach to equilibrium; indeed, near-equilibrium sulfur capture may be obtained when hydrated lime is introduced as a "mist" spray. To investigate the influence of pyrolysis temperature on product yield and composition, experiments and computations have been performed at 649°C with and without the presence of calcium compounds. The predicted and observed percentage of sulfur content ( $H_2S$  and COS) in the product gases is slightly reduced at 649°C compared to that at 500°C (Table 1). The increased levels of CO and  $H_2$  and the reduction in CO at higher temperature are also simulated by the equilibrium code. At both temperatures the influence of CaO addition on sulfur products is seen to be qualitatively similar, as predicted.

The equilibrium model cannot simulate differences in the performance of the same sorbent (e.g., CaO) prepared from different sources (e.g.,  $CaCO_3$ ,  $Ca(OH)_2$ , dolomite,

calcined dolomite, hydrated calcined dolomite), since these differences are caused largely by the varying pore structures of the sorbent. Differentiation of additives generated from various parent compounds and at different treatment conditions necessarily involves kinetic modeling; however, the present equilibrium-rate chemistry model can still be used to compare the maximum reactivity of the CaO additive with that of other low-cost inorganics (e.g.,  $\text{CaCO}_3$ ,  $\text{Fe}_2\text{O}_3$ ,  $\text{MgO}$ ,  $\text{SiO}_2$ ). These observed and predicted effects on the SHRODR products are listed in Table 2. Adding 35 weight percent  $\text{CaCO}_3$  (Ca/S of about 6) to the Pittsburgh coal at 500°C is observed to reduce  $\text{H}_2\text{S}$  from 3.7 volume percent to only about 2.3 volume percent, whereas the PACKAGE code predicted a greater reduction. This is perhaps a consequence of previously reported (19) kinetic limitations to the calcination process below 600°C. A 21 weight percent  $\text{Fe}_2\text{O}_3$  significantly reduces the yield of  $\text{H}_2\text{S}$  and COS; this reduction is accompanied by the formation of FeS (troilite, identified by X-ray diffraction). These observed effects of  $\text{Fe}_2\text{O}_3$  addition are also predicted theoretically. SHRODR experiments and simulations were also performed with MgO and  $\text{SiO}_2$  additives. However, the presence of these inorganics has very little influence on devolatilized product yield and composition, as predicted by the PACKAGE computer program.

#### 4.2 Coal Gasification Applications

In view of the long residence times (2-3 hours) associated with fixed-bed gasifiers, the use of an equilibrium approach is well-suited to this environment. Comparisons between PACKAGE predictions and experimental gas-phase sulfur data obtained under gasification conditions in the presence of sorbents are presented in Table 3. The  $\text{H}_2\text{S}$  concentrations reported here were obtained by on-line laboratory analyses of gases generated during a series of METC fixed-bed gasifier runs. Since water was removed from all samples subjected to on-line analyses, results are reported on a dry gas basis; computer predictions are reproduced in Tables 3 and 4 on the same dry basis. The single-temperature, single gas/solid ratio analysis presented here is based upon the hypothesis that sulfur sorption in the gasifier column is controlled by fast chemical reactions that occur in a narrow section of the column, just above the combustion zone (see Figure 1). Further up in the column, calcination of the limestone additive is not thermodynamically feasible, implying severely reduced sulfur uptake by limestone; whereas, below this critical section, the lime is either saturated (due to absorption of recycle sulfur dioxide) or bound up in the form of silicates, aluminosilicates, etc., resulting from ash interactions under oxidizing conditions.

The calculations shown in Table 3 have been performed at a temperature of about 1000 K, and the gas/solids flow rate ratio (approximately 5) consistent with that temperature in the gasifier. The gas/solids ratio represents the distribution of the components of the reactive mixture in the two phases, and the temperature has been chosen on the basis of maximum availability of calcium to react; any temperature in the "temperature window" of 900-1100 K would have served equally well. These attempts to predict the observed sulfur capture by means of a simple equilibrium thermodynamic approach are no more than a prelude to the combined dynamic-thermodynamic-kinetic analysis planned for the future; yet even these preliminary equilibrium calculations show good agreement with experimental measurements for all gas species concentrations, including the hydrocarbons,  $\text{CO}_2$ ,  $\text{CO}$ ,  $\text{H}_2$  (Table 4), as well as  $\text{H}_2\text{S}$  (Table 3). In the case of the C-H-O species, the higher temperatures involved, the relative insignificance of tar-char chemistry, and the close approach to equilibrium of the water-gas shift reaction, apparently bring about a better match between theory and practice.

The PACKAGE code is equally effective in simulating the effect of changes in operating variables on sulfur uptake. At higher pressures (200 psig), calcination is delayed to higher temperatures, occurring further down in the gasifier column. In the absence of excess (recycled) sulfur, lime, once it forms, immediately reacts with the ash mineral constituents and is thus not available to react with the sulfur.

When sulfur is added in the form of a recycle  $\text{SO}_2$  stream, equilibrium favors the formation of  $\text{CaS}$  and  $\text{CaSO}_4$  over calcium silicates and aluminosilicates; this results in increased sulfur capture efficiency and increased sorbent utilization. Thus, in high-pressure runs with no  $\text{SO}_2$  recycle,  $\text{H}_2\text{S}$  volume percent in the gas is high and insensitive to  $\text{Ca/S}$  ratio (calculated with respect to the coal), but low and very responsive to the same parameter when some sulfur is fed back in. These predicted trends are consistent with observed gasifier performance. Some observations, such as the difference in effectiveness of the Germany Valley and Lowellville limestones, are beyond the capability of this approach to rationalize, but the present methodology is still of value in evaluating the limits of performance of gasifiers and sorbents.

#### 4.3 Coal Combustion Applications

The equilibrium-thermodynamic approach has also been used to analyze the effect on combustion gas-phase sulfur concentration of adding calcium to a coal-water fuel. Conditions used in the calculations simulated those occurring in a recent GE LM500 Turbine Simulator run which indicated high sulfur capture (at the cost of increased deposition). In this experimental study, calcium hydroxide was integrated into coal-water mixtures and injected in a combustion system which simulates the thermodynamic and aerodynamic environment of a gas turbine. Sulfur capture was determined by analysis of extracted gas and solid samples. The PACKAGE computer program predicts 80 percent sulfur capture for calcium-to-sulfur ( $\text{Ca/S}$ ) atomic ratio of 1.5, fuel-to-air ratio of 0.07,  $1100^\circ\text{C}$ , and 10 atmospheres. This compares well with the reported GE data of 60-70 percent capture (20) for hydrated sorbents. It is intriguing that even short residence time conditions such as these do not necessarily invalidate equilibrium modeling. Even though sorbent utilization is certainly lime-dependent, the assumption of instantaneous reaction is probably not farfetched in the highly reactive, high-temperature combustion environment.

#### 5. CONCLUSIONS AND RECOMMENDATIONS

An attempt has been made in this paper to illustrate and justify the use of an equilibrium-thermodynamic approach to modeling the distribution of sulfur species in the product streams of coal conversion processes. It has been demonstrated that equilibrium calculations simulate the qualitative effects of various sulfur sorbents and gas cleanup conditions (temperature, pressure, sorbent-to-sulfur ratio) with good accuracy, especially in reactor configurations that ensure close mixing of the components. The extent to which equilibrium estimates of sulfur capture and sorbent utilization are quantitatively realistic has been evaluated on the basis of comparisons with data obtained under coal devolatilization (in the METC SHRODR), gasification (in the METC fixed-bed gasifier), and combustion (in the GE turbine simulator) conditions. Preliminary indications are that equilibrium composition predictions are in surprisingly good quantitative agreement with measured data for all species included in the extensive thermodynamic data base employed. This tentative conclusion will be verified by repeated comparisons of model predictions with other sulfur-removal data as it becomes available. The unexpected success of the present preliminary computational model for sulfur sorption bodes well for the more comprehensive theoretical analyses planned for the future. The anticipated failure of this simple algorithm to simulate transport and kinetic limitations to the sulfur-lime reaction notwithstanding, the most attractive features of the equilibrium approach remain the elimination of the uncertainties surrounding more detailed gas/solid interfacial kinetic models, and the relative ease and convenience of its application.

## 6. REFERENCES

- (1) Khan, M.R., Fuel Sci. Technol. Intl., 5, 185-231, 1987.
- (2) Landers, W.S., et al., U.S. Bureau of Mines, Report of Investigation No. 5904, 1961.
- (3) Wen, C.Y., Chen H., and Onozaki, M., Final Report, DOE/MC/16474-1390 (DE83009533), January 1982.
- (4) Nsakala, N.Y., Essenhigh, R.H., and Walker, Jr., P.L., Combustion Sci. Technol., 16, 153, 1977.
- (5) Anthony, D.B., and Howard, J.B., AIChE J., 22, 625, 1976.
- (6) Scaroni, A.W., Khan, M.R., Eser, S., and Radovic, L.B., in Ullmann's Encyclopedia of Industrial Chemistry, 5th Edition, Vol. A7, 245-280, 1986.
- (7) Serio, M.A., Hamblen, D.G., Markham, J.R., and Solomon, P.R., Energy Fuels J., 1, 138-152, 1987.
- (8) Yoon, H., Wei, J., and Denn, M., Electric Power Research Institute Report AF-590, Vol. 1, 1977, Vol. 2, 1978.
- (9) Denn, M., Wei, J., Yu, W.-C., and Cwiklinski, R., Final Report prepared for Electric Power Research Institute (EPRI AP-2576), September 1982.
- (10) TRW Systems and Energy Group; Report prepared jointly with Morgantown Energy Technology Center, October 1978.
- (11) Joseph, B., Bhattacharya, A., Salam, L. and Dudukovic, M.P.; Final Report to U.S. DOE-METC, January 1984.
- (12) White, W.B., Johnson, W.M. and Dantzig, G.B.; J. Chem. Phys., 28, 751, 1958.
- (13) Simons, G.A., Garman, A.R., and Boni, A.A.; AIChE J., 33, 211-217, 1987.
- (14) Sotirchos, S.V., in press, Chem. Eng. Sci., 1987.
- (15) Stinnett, S.J., Harrison, D.P., and Pike, R.W., Environ. Sci. Technol., 8, 441-444, 1974.
- (16) Yousefian, V., Weinberg, M.H., and Haines, R., Aerodyne Research, Inc., Report No. ARI-RR-177, 1980.
- (17) Ross, J.S., Anderson, R.J., and Nagarajan, R., in press, Energy Fuels J., March 1988.
- (18) Nagarajan, R., and Anderson, R.J., to be presented at the Intl. Gas Turb. Aeroeng. Congr. Expo., 33rd, Amsterdam, The Netherlands, June 5-9, 1988.
- (19) Franklin, H.D., Ph.D. Thesis, Massachusetts Institute of Technology, 1980.
- (20) Slaughter, D., Spiro, C., Lavigne, R., and Kimura, G., to be presented at the EPA/EPRI Comb. FGD and Dry SO<sub>2</sub> Control Symp., St. Louis, Missouri, October 25-28, 1988.

Table 1. Products of Atmospheric-Pressure Slow-Heating Devolatilization of Pittsburgh No. 8 Coal in the SHRODR

Species	No Added Lime		Volume Percent In Gas		+ 10 Weight Percent CaO		+ 21 Weight Percent CaO	
	Experimental	Predicted	Experimental	Predicted	Experimental	Predicted	Experimental	Predicted
CH <sub>4</sub>	49.80	25.36	Temperature = 500°C	30.74	53.70	39.76	53.70	39.76
CO	0.39	1.31						
CO <sub>2</sub>	0.39	0.0044						
H <sub>2</sub>	5.40	7.01						
H <sub>2</sub> O	11.60	32.61						
H <sub>2</sub>	3.70	2.26	Temperature = 640°C	(0.61)*	0.00	0.004	(0.0)*	0.004
H <sub>2</sub> S	(3.20)*	2.88						
CH <sub>4</sub>	49.80	8.85	Temperature = 640°C		46.66	12.93		
CO	0.39	12.895						
CO <sub>2</sub>	0.39	0.0044						
H <sub>2</sub>	5.40	5.17						
H <sub>2</sub> O	20.00	61.50						
H <sub>2</sub>	3.70	12.96						
H <sub>2</sub> S		2.18						

(\* Data with < 10 µm CaO Pellets)

T86-0869-1 BP5

Table 3. Effect of Operating Variables on Sulfur Concentration in the Product (Raw) Gases of the METC Fixed-Bed Gasifier

Pressure (psig)	Recycle SO <sub>2</sub> (lb/hr)	Calcium-to-Sulfur Ratio, Ca/S		Volume Percent of H <sub>2</sub> S in the Gas	
		Experimental	Predicted	Experimental	Predicted
200	0	Baseline	0.32	0.42	
		2	0.32	0.41	
		1*	0.30	0.40	
			0.31	0.33	
100	80	1	†	0.67	
		2	†	0.53	
	100	1	†	1.14	
		2	†	0.93	
100	0	2	0.29	0.22	
		1	0.46	0.34	
	100	2†††	1.55	0.84	
		2††††	0.64	0.98	

\* Fe/Ca/S = 0.5/1/1  
† Data Under Analysis

†† Lowville Limestone  
††† Germany Valley Limestone

T86-0869-3 BP5

Table 2. Products of Atmospheric-Pressure Slow-Heating Devolatilization of Pittsburgh No. 8 Coal at 500°C in the SHRODR: Effect of Inorganic Additives on Sulfur

Species	+ 21 Weight Percent CaCO <sub>3</sub>		+ 35 Weight Percent CaCO <sub>3</sub>		+ 21 Weight Percent Fe <sub>2</sub> O <sub>3</sub>	
	Experimental	Predicted	Experimental	Predicted	Experimental	Predicted
CH <sub>4</sub>	48.90	24.60	47.90	17.48	45.90	24.81
CO	—	1.78	4.50	2.53	2.90	1.83
CO <sub>2</sub>	—	—	—	—	—	—
H <sub>2</sub>	6.10	8.03	7.90	15.93	8.35	9.20
H <sub>2</sub> O	33.10	33.10	9.80	27.90	16.10	33.20
H <sub>2</sub>	—	—	—	—	—	—
H <sub>2</sub> S	3.30	1.40	2.30	0.26	0.1	0.04
CH <sub>4</sub>	+ 21 Weight Percent MgO	25.33	48.90	25.33	+ 21 Weight Percent SiO <sub>2</sub>	
	+ 21 Weight Percent MgO	1.87	3.90	0.005	+ 21 Weight Percent Fe <sub>2</sub> O <sub>3</sub>	
CO	+ 21 Weight Percent MgO	6.93	5.50	6.93	+ 21 Weight Percent Fe <sub>2</sub> O <sub>3</sub>	
	+ 21 Weight Percent MgO	33.58	10.80	33.58	+ 21 Weight Percent Fe <sub>2</sub> O <sub>3</sub>	
H <sub>2</sub>	+ 21 Weight Percent MgO	2.00	3.40	3.40	+ 21 Weight Percent Fe <sub>2</sub> O <sub>3</sub>	
	+ 21 Weight Percent MgO	10.80	3.40	3.40	+ 21 Weight Percent Fe <sub>2</sub> O <sub>3</sub>	
H <sub>2</sub> S	+ 21 Weight Percent MgO	3.00	3.40	3.40	+ 21 Weight Percent Fe <sub>2</sub> O <sub>3</sub>	
	+ 21 Weight Percent MgO	10.80	3.40	3.40	+ 21 Weight Percent Fe <sub>2</sub> O <sub>3</sub>	

T86-0869-2 BP5

Table 4. Pittsburgh No. 8 Coal Gasification Product Gas Composition: P = 100 psig, SO<sub>2</sub> Recycle = 70 lb/h, Ca/S = 2

Species	Volume Percent In Gas	
	Experimental	Predicted
Ar	0.57	0.53
CH <sub>4</sub>	2.89	1.47
CO	12.47	12.47
CO <sub>2</sub>	15.22	15.42
H <sub>2</sub>	20.11	24.46
H <sub>2</sub> O	46.34	46.34
H <sub>2</sub> S	0.48	0.34
COS		0.005
Total (S)	0.48	0.35

T86-0869-4 BP5

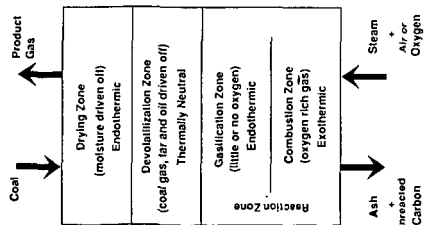


Figure 1. Schematic of Fixed-Bed Gasifier (3)

CS-862-B BP4

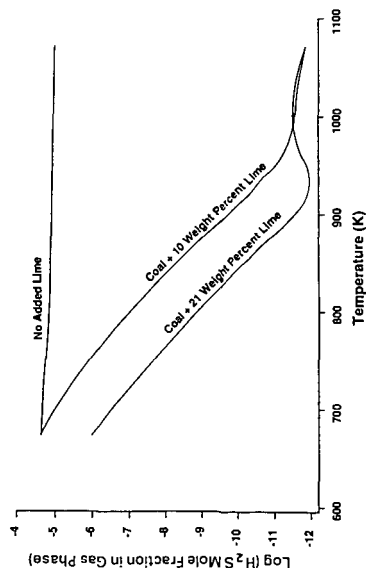


Figure 3. Effect of Added Lime on Gas-Phase Sulfur in Atmospheric-Pressure Devolatilization of Pittsburgh No. 8 Coal

CS-862-B BP4

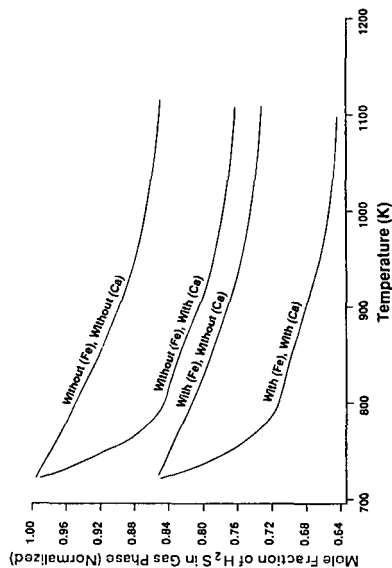


Figure 2. Effect of Iron and Calcium in Pittsburgh No. 8 Coal on Sulfur in the Atmospheric-Pressure Devolatilization Product Gases

CS-862-A BP4

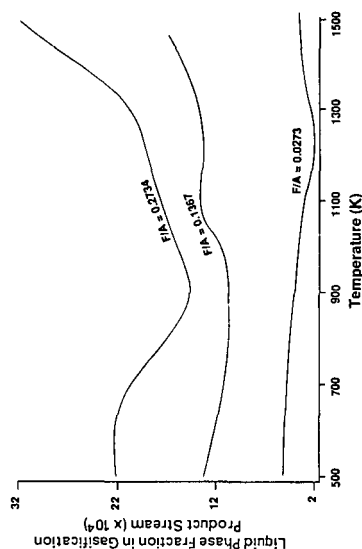


Figure 4. Temperature- and Fuel-to-Air Mass Flow Rate Ratio (F/A) Dependence of Liquids Fraction in the Product Mixture of Atmospheric-Pressure Gasification of Pittsburgh No. 8 Coal

CS-862-C BP4

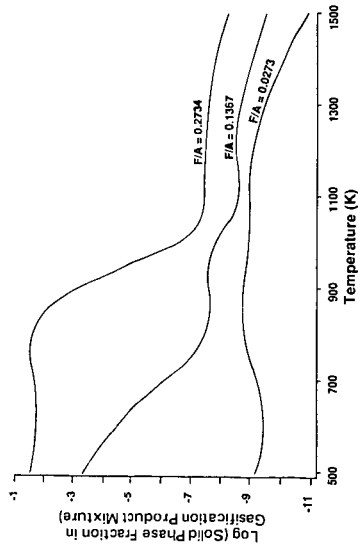


Figure 5. Temperature- and Fuel-to-Air Mass Flow Rate Ratio (F/A) Dependence of Solids Fraction in the Product Mixture of Atmospheric-Pressure Gasification of Pittsburgh No. 8 Coal

MS-525-C BP3

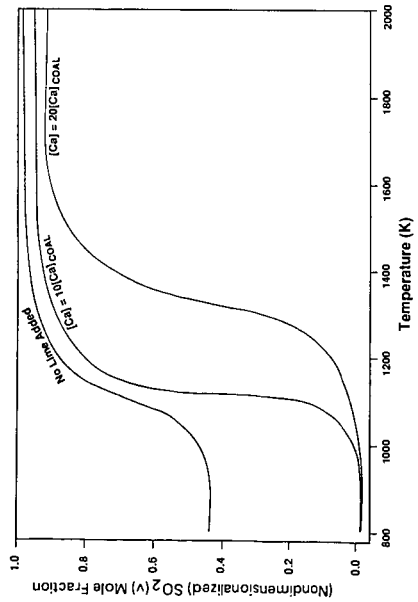


Figure 7. Effect of Temperature and Added Lime on Sulfur Dioxide Concentration in the Product Gases of Atmospheric-Pressure Combustion of Pittsburgh No. 8 Coal

MS-525-C BP3

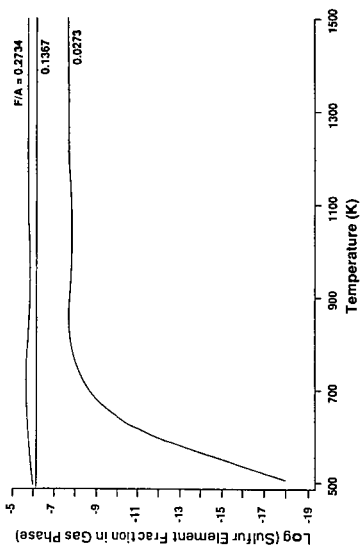


Figure 6. Temperature- and Fuel-to-Air Mass Flow Rate Ratio (F/A) Dependence of Total Sulfur Concentration in the Product Gases of Atmospheric-Pressure Gasification of Pittsburgh No. 8 Coal

MS-463-E BP4

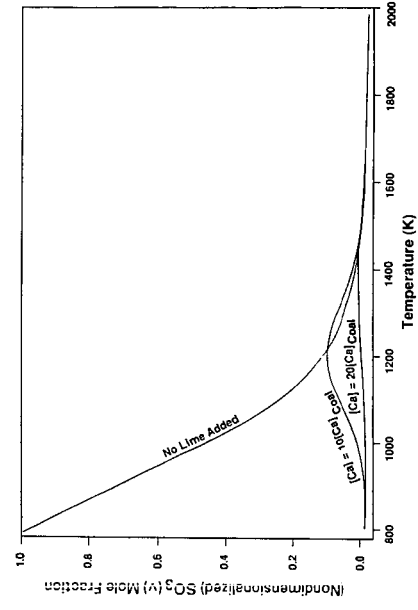


Figure 8. Effect of Temperature and Added Lime on Sulfur Trioxide Concentration in the Product Gases of Atmospheric-Pressure Combustion of Pittsburgh No. 8 Coal

MS-525-B BP3



## MODEL OF ASH SIZE DISTRIBUTIONS FROM COAL CHAR OXIDATION

Boyd F. Edwards and Anjan K. Ghosal

Department of Physics, West Virginia University  
Morgantown, WV 26506

### 1. Abstract

A flexible model of final ash size distributions resulting from coal char oxidation under varying conditions is presented. To include the important effects of fragmentation during char oxidation, we have modeled three-dimensional char particles as porous spatially random "percolation" clusters on a cubic bond lattice. Random walkers represent oxygen diffusion to the surface of the char particles. A reaction probability  $r$  governs whether a random walker reaching the surface will react with a unit mass of char. Thus, values of  $r$  from near zero to unity take the model from a chemical-reaction-limited to a diffusion-limited regime. Fragmentation events occur when reactions break the connectivity of the clusters, leading to a distribution of ash particle sizes after burnout. In the chemistry-limited regime, penetration of the random walkers into the pores of the cluster results in major fragmentation events and a correspondingly large number of ash particles. In the diffusion-limited regime, the lack of such penetration results in fewer ash particles with a larger maximum size. Model parameters are related to experimental conditions such as temperature, particle diameter, char porosity, and ash content. Results are compared with experiments.

### 2. Introduction

Coals typically contain about 10% incombustible mineral matter mainly in small separate inclusions in the coal. During combustion these particles can be released into the furnace gases as fly ash and may range from a hundredth of a micron to up to a 100 microns in diameter. These ash particles clog heat transfer equipment, corrode boiler tubes and create environmental hazards. To fully address these problems, it is important to understand the mechanism of ash formation. In this paper, we present a model of coal char oxidation designed to supply this understanding. Our objective is to numerically simulate the effect of coal morphology, burning rate, and initial ash content on the final ash size distribution.

Recent measurements of burning-rate time histories for single char particles in a fluidized bed (1) offer new insights into the dynamics of the combustion process. Of particular interest are successive sharp increases in the burning rate interrupting the overall downward trend. These sharp increases were interpreted as the fragmentation of char particles or subparticles into two or more pieces, and were not observable in previous time-averaged or ensemble-averaged measurements.

Though useful in characterizing various oxidation regimes, standard models of char oxidation deemphasize fragmentation by treating char particles as uniform spheres (2,3), thereby simplifying the problem of oxygen diffusion to the surface. Subsequent models allow for fragmentation effects by treating char particles as random porous shapes. Reyes and Jensen (4,5) modeled char oxidation on a Bethe (tree-like) lattice by randomly removing bonds (unit line segments) from anywhere on the lattice. More realistically, Kerstein and Bug (6) randomly removed an initial fraction of bonds from the Bethe lattice to represent the porosity of the unburned char particle, and randomly removed only surface bonds to simulate oxidation. To account for loop effects (which are absent on the Bethe lattice), Sahimi and Tsotsis (7) studied surface bond removal on a porous three-dimensional site lattice in the chemistry limited regime (Zone I). A Zone III (diffusion-limited) model (8) accounted for the sharp increases in the burning-rate measurements, ascribing them to a higher burning rate per unit surface area of char fragments than their parent char particles. These models demonstrated the utility of modeling char particles as random "percolation" clusters on a three-dimensional cubic lattice.

Models of char oxidation and fragmentation to date neglect ash formation and force all particles into a particular regime (Zone I or Zone III) regardless of size. In contrast, the smallest particles in real combustion systems might be in Zone I (because of their higher surface oxygen concentration) while the larger particles are simultaneously in Zone III (2). The present model incorporates both regimes

along with the intermediate regime (Zone II), as well as incorporating ash formation.

Further measurements on a finely graded Montana lignite (9,10) with mass averaged mineral inclusion size of 2 microns indicate strong dependencies of the final ash size distribution on temperature, initial particle size, and oxygen concentration. In this paper, we directly compare the predictions of the model with these experiments.

### 3. Model

The distribution of ash particle sizes after complete burnout depends on the competition between several mechanisms. Mineral inclusions melt and can coalesce as the surface of the char particle recedes, leading to large ash particles. Small protrusions in the irregular char surface can be liberated as the surface recedes, producing small ash particles. In the chemistry-limited regime, oxygen diffusion and oxidation in the pores can lead to separation of char particles into particles of comparable size, leading to ash particles more evenly distributed in size. Finally, mineral vaporization at the surface and subsequent condensation can lead to very small ash particles (11). Since they solidify from liquid mineral droplets, ash particles are typically spherical or near spherical.

To incorporate the most important mechanisms of ash production into our model in a straightforward way, we employ a representation of char particles on a cubic lattice similar to one used in a previous model (8), except that here we include mineral matter in the representation. The lattice representation employs the site percolation concept; each site on a cubic lattice has probability  $p = 0.3117$  of being "occupied". Groups of adjacent occupied sites are termed site clusters. This value of  $p$  is the "percolation threshold" value above which a cluster spanning the cubic site lattice is guaranteed to exist. All unit line segments, or "bonds", within a radius  $R$  of occupied sites are designated as solid. The resulting bond cluster represents a porous char particle whose compactness is governed by  $R$ . A fraction of the bonds in the cluster are assigned masses of mineral material to simulate mineral inclusions. Note that a bond is a line segment between nearest neighbor sites on a lattice, representing a mass of combustible and mineral material, and does not represent a chemical bond.

Char oxidation is modeled by introducing random walkers representing oxygen. Each time a random walker encounters a solid bond, that is, each time it crosses a solid bond, it has a probability  $r$  of reacting with the bond. A reaction is defined as the annihilation of both the walker and the combustible content of the bond. If an encounter does not lead to reaction, the walk continues from the point where it entered the solid. In this way, small values of  $r$  lead to many encounters before reaction occurs, allowing walkers to deeply penetrate the pores before reacting. A reaction that breaks the connectedness of a cluster is deemed a fragmentation event. After such an event, the random walkers ignore all solid bonds except those pertaining to a single fragment to simulate physically separated particles produced by fragmentation events, each with a separate supply of oxygen. The fragments are oxidized one at a time in this manner until all have been oxidized. The site lattice oxidation model by Sahimi and Tsosis (7,12) apparently ignores this physical separation. Extension of the model to give the time-dependent char fragment size distribution during oxidation is in progress.

Two limiting behaviors for reallocating the mineral mass of a reacted bond are simulated as follows. Limit I: For strong cohesion between adjacent melted mineral inclusions, the mineral mass of a reacted bond is given to the adjacent solid bond with the largest mineral mass, giving strong coalescence of mineral matter. Limit II: In the opposite case of weak mineral cohesion and relatively strong adhesion between melted mineral inclusions and char material, the mineral mass of a reacted bond is equally divided among its adjacent solid bonds, giving weak coalescence. When the last solid bond of a cluster reacts, its mineral mass is deemed the mass of an ash particle. When all solid bonds have reacted, the ash mass distribution is complete. The corresponding ash size distribution follows from the sphericity of the ash particles. In this way, the model captures the effects on the ash distribution of surface coalescence, liberation of surface protrusions, and pore diffusion during oxidation. Although the model does not account for mineral vaporization (11), the very small submicron ash particles created by this mechanism are negligible in the final mass-weighted size distribution. We assume that the adhesion between melted mineral inclusions of different chemical compositions, if such differences occur in the coal being considered, can be treated as identical to the cohesion of inclusions of the same composition.

The advantage of using a bond lattice rather than a site lattice is the absence of unphysical spurious

multiple fragmentation events. Removing a single site from a cubic site lattice can result in up to 6 fragments, whereas removing a single bond from a cubic bond lattice results in no more than two fragments.

The reaction probability  $r$  depends on the particle diameter  $d$  through the oxygen diffusion rate  $K_d$  (see Section 4 below). Thus, it is necessary to define the diameter of a cluster on the cubic bond lattice which can be related to the actual particle diameter  $d$ . This "lattice diameter"  $d_l$  is defined as the average of the cluster dimensions in the three cartesian directions;  $d_l = (x_{\max} - x_{\min} + y_{\max} - y_{\min} + z_{\max} - z_{\min}) / 3$ , measured in units of the lattice spacing. The lattice spacing in microns, which remains fixed during the simulation, is determined initially by equating the initial particle diameter  $d$  (in microns) to the diameter  $d_l$  of the cluster used to simulate it (in lattice spacings). The diameter and the corresponding reaction probability  $r$  of a particular particle decrease monotonically from an initial value during oxidation, taking it into the chemistry-limited regime as it decreases in size. Cluster diameters and corresponding reaction probabilities are accordingly updated after each bond reacts.

Random walkers are introduced at random locations on a box with linear dimensions a factor of 1.4 larger than the dimensions of the box of dimensions  $x_{\max} - x_{\min}$ ,  $y_{\max} - y_{\min}$ , and  $z_{\max} - z_{\min}$ . Tests to be described elsewhere indicate that this method of introducing random walkers yields probabilities of contacting particular solid bonds that are within 4% of the probabilities obtained by introducing the walkers an infinite distance from the cluster.

#### 4. Relation of the reaction probability $r$ to physical quantities

For a first-order reaction, the rate of consumption  $Q$  of carbon at the surface of a char particle of diameter  $d$  is proportional to the partial pressure  $C_s$  of oxygen at the surface through the relation  $Q = K_c C_s$ , where  $K_c = A \exp(-E/RT_s)$  is the chemical reaction rate characterizing the chemisorption process. This oxygen at the surface arrives by diffusion across the relatively stagnant gas film between the bulk gas stream and the solid surface. The corresponding alternative relation  $Q = K_d (C_b - C_s)$  involves the oxygen diffusion rate  $K_d = B T_s^{0.75} / d$  (Refs. 13, 14). Since the bulk oxygen partial pressure  $C_b$  is the measurable quantity, a third relation  $Q = K C_b$  defines the overall reaction rate  $K$ , which is simply related to its constituent rates as  $K^{-1} = K_d^{-1} + K_c^{-1}$  by combining the three forms for  $Q$ . For very small surface temperatures  $T_s$ ,  $K = K_c$  and a small oxygen flux to the surface is sufficient to sustain the slow chemical reactions both at the external surface of the solid and deep within its pores (Zone I). At higher temperatures, oxygen is unable to diffuse into the pores fast enough to completely support the faster chemical reactions, but is plentiful at the external surface (Zone II). At yet higher temperatures,  $K = K_d$  and oxygen diffusion is unable to completely support the chemical reactions even at the external surface (Zone III).

The foregoing assumes an order of reaction equal to unity. CO is typically the primary oxidation product in char combustion (2), but converts to CO<sub>2</sub> a distance from the particle. Experimental evidence that CO<sub>2</sub> is the combustion product most relevant to diffusion to and from char particles, and that the order of reaction is consequently close to unity, is given by Field (15) for pulverized chars with  $0.05 \text{ atm} < C_b < 0.20 \text{ atm}$ , and by Smith (13). Accordingly, we take  $A = 8710 \text{ g cm}^{-2}\text{s}^{-1}\text{atm}^{-1}$ ,  $E = 35700 \text{ cal/mole}$ , and  $R = 1.986 \text{ cal mole}^{-1} \text{K}^{-1}$  (3), which apparently apply generally, to within the accuracy of our simulations, to coals excluding pyrolytic graphites and anthracites. The value  $B = 5.62 \times 10^{-6} \text{ g cm}^{-2}\text{s}^{-1}\text{atm}^{-1}$  based on the external surface area (mass removed per unit external surface area per atmosphere of O<sub>2</sub> per unit time) follows from the corresponding mass-based coefficient given by Smith (13), which depends on the diffusivity of O<sub>2</sub> in air. More specific values of  $E$ ,  $R$ , and  $A$  for various coal types are given by Wall and Gururajan (16).

The reaction probability  $r$  of the simulations follows simply from the overall reaction rate  $K$ . For  $r$  near zero, random walkers encounter the solid many times before reacting with it, allowing the walkers to deeply penetrate pores before reacting, corresponding to chemistry-limited conditions and a slow reaction rate  $K$ . For  $r$  near unity, an encounter almost always leads to reaction and only the most exposed parts of the cluster are consumed, corresponding to diffusion-limited oxidation and a high reaction rate  $K_d$ . In this way, the reaction probability is just the overall reaction rate normalized to unity;  $r = K/K_d = K_c/(K_c + K_d)$ .

## 5. Model tuning

The model is tuned by comparing with data from combustion of a finely graded (38-45 micron diameter with median diameter 39 microns) lightly swelling Montana lignite studied experimentally by Sarofim (9). Their microscopic examination of these particles indicates that the mineral matter is distributed as separate inclusions comprising about 8% of the coal with a maximum weight fraction at a diameter of 2 microns. Lacking detailed information about the small amount of swelling during devolatilization, we simply use the initial coal particle diameter as the diameter relevant to char oxidation. Particle surface temperatures  $T_s$  typically exceed bulk gas temperatures  $T_b$  by about 200 K (2).

To facilitate careful comparison with the experiments, the mineral masses assigned to bonds in the cluster are chosen to obey the distribution of the mineral inclusions measured in the experiments, which is apparently independent of coal particle size over the relevant range of particle sizes. In particular, the number of required inclusions in each of six bins of width 0.5 microns is determined from Figure 6 of Sarofim (9) based on the overall diameter  $d$  of the assumed spherical coal particle, the mineral fraction (8%), and the approximately equal density  $3.5 \text{ g cm}^{-3}$  of char and mineral matter. The mass of the assumed spherical inclusions in each bin follows from the mean bin diameter. The  $N$  mineral inclusions required by the procedure are then randomly assigned to  $N$  bonds in the cluster ( $N = 1749$  for  $d = 39$  microns), and the remaining bonds in the cluster are assigned zero mineral mass. Our clusters typically contain from  $N$  to  $1.1 N$  bonds. The largest simulated particle diameter was 44 microns.

We use the conditions  $d = 39$  microns and  $T_s = 2000 \text{ K}$  to tune the cluster compactness and the method of mineral matter reallocation during combustion. For unit compactness ( $R = 1$ ) and for weak mineral cohesion (limit II), we obtain a distribution with a narrow peak in the ash mass fraction per micron at about 2.5 microns compared with a corresponding median diameter of 9 microns for comparable conditions in the experiments [Figure 14 of Ref. (9),  $T_b = 1830 \text{ K}$ ]. For higher compactness ( $R = 2$ ) and for strong mineral cohesion (limit I), the median diameter rises to about 4.4 microns (Figure 1) and the width of the distribution is comparable to that of the experiments. For  $R = 3$  and strong mineral cohesion, we obtain a very broad distribution centered very roughly at 8 microns. To better facilitate the study of the shifts in median diameter with temperature and particle diameter, we henceforth employ the more sharply peaked intermediate compactness  $R = 2$  in the strong mineral cohesion limit. Our choice of compactness may correspond more closely to more porous chars, such as bituminous chars, than to the lignite of the experiments. We believe however that the directions and relative magnitudes of the shifts in the median diameter due to changing temperature and particle diameter should be applicable to a wide range of porosities including the lignite of the experiments, since these shifts arise from different oxidation regimes applied to the same types of particles. Our choice of strong mineral cohesion seems consistent with current understanding of the process of mineral coalescence.

## 6. Predictions and comparisons with experiments

To illustrate the dependence of the ash particle size distribution on temperature, Figure 1 shows our simulated mass-weighted ash size distributions for  $d = 39$  microns at  $T_s = 1500, 2000$ , and  $2500 \text{ K}$ . The data points are the output of the simulations; the solid traces are fifth-order polynomial fits to the data. The cluster used in all three simulations had 1781 bonds including 1749 mineral inclusions. The data show a systematic shift toward larger ash particles with increasing temperature (Figure 1); median diameters deduced from the fits are 3.7, 4.4, and 4.8 microns. A significant decrease in the overall number of ash particles from 171 at  $T_s = 1500 \text{ K}$  to 115 at  $T_s = 2500 \text{ K}$  (Table 1) accompanies the shift toward larger ash particles. Physically, the larger ash particles result from a decrease in pore wall oxidation and a corresponding decrease in fragmentation as the oxidation approaches the diffusion-limited regime with increasing temperature. The experimental data of Sarofim et al. (9) do not show an clear shift toward larger ash particles for increasing temperatures. Even so, for the case of  $d = 39$  microns, the experimental ratio 0.86 between median ash particle diameters at bulk gas temperatures  $T_b = 1830 \text{ K}$  and  $T_b = 1250 \text{ K}$  [deduced from Figure 14 of Ref. (9)] compares well with our ratio 0.84 deduced from the median diameters at the corresponding surface temperatures  $T_s = 2000 \text{ K}$  and  $T_s =$

1500 K. The experimental overall number of ash particles 160 at  $T_s = 2000$  K [estimated from data for  $d = 53$ -63 and 75-90 microns and bulk temperatures  $T_b = 1750$  K, Ref. (10)] is comparable to our value of 121 (Table 1).

To determine the dependence of the ash particle size distribution on initial particle diameter, Figure 2 shows our simulated ash size distributions for  $d = 34, 39$ , and  $44$  microns at  $T_s = 2000$  K. The corresponding clusters have 1162 (1152), 1781 (1749), and 2665 (2509) bonds, where parentheses enclose the numbers of bonds assigned mineral inclusions. Over this range of diameters, no clear trend in the ash particle size distribution is discernible (Figure 2). The increase with diameter of the overall number of ash fragments (Table 1) reflects the larger number of mineral inclusions in particles of larger diameter. The initial values of the reaction probability for these particles are 0.58, 0.61, and 0.64, respectively.

## 7. Conclusions

This paper presents, to our knowledge, the first model predicting ash distributions resulting from char oxidation and fragmentation incorporating the three regimes of oxidation. The model yields overall numbers of ash particles and shifts in ash particle distributions which agree with experiments on a Montana lignite. Since the sparse cluster morphologies studied in this paper underestimate the experimental median ash particle size, these morphologies may correspond best to more porous bituminous chars. Over the range of particle diameters studied (34-44 microns), the model predicts no variation in the median ash diameter with initial particle size. Further simulations of denser cluster morphologies and over larger diameter ranges are underway.

Experiments on the process of molten mineral matter reallocation during combustion would be very useful in connection with our ongoing simulations. Additionally, since significant swelling and morphological changes may occur during devolatilization, experiments on combustion of well-characterized chars (including sizes, porosities, and mineral matter distributions) would be useful.

The model provides a flexible and powerful framework in which to study the separate and combined effects of initial mineral content and distribution, coal type and morphology, oxygen concentration, temperature, and particle size on the final ash size distribution. It can be used to compare and correlate experimental data, as well as to study parameter sensitivities that are difficult to explore experimentally.

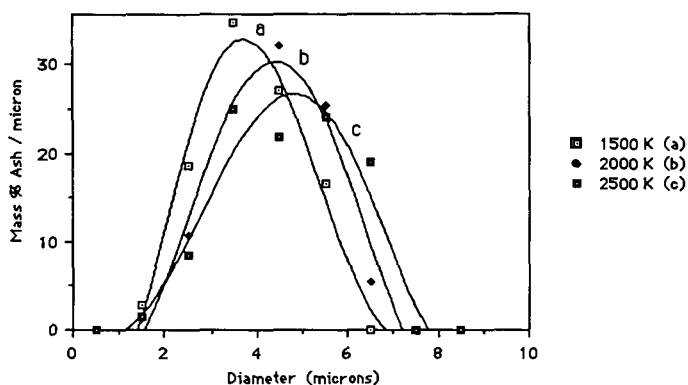


Figure 1. Mass-weighted ash size distribution for simulated coal particle diameter 39 microns and surface temperatures 1500, 2000, and 2500 K.

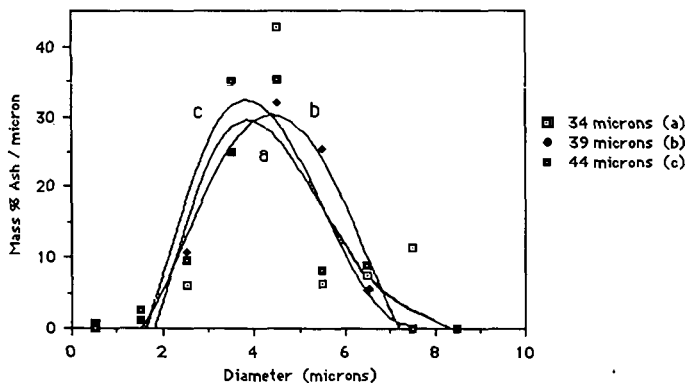


Figure 2. Mass-weighted ash size distribution for simulated coal particle diameters 34, 39, and 44 microns at surface temperature 2000 K.

		Ash particle size range (microns)										
d (μm)	T <sub>s</sub> (K)	0-1	1-2	2-3	3-4	4-5	5-6	6-7	7-8	8-9	total	
39	1500	25	34	53	39	15	5				171	
39	2000	24	17	30	26	16	17	1			121	
39	2500	27	18	23	26	11	7	3			115	
34	2000	12	12	11	17	16	1	1	1		71	
44	2000	45	48	36	54	14		2			216	

Table 1. Numbers of ash particles of different sizes ranges for simulated coal particles of diameter d and surface temperature T<sub>s</sub>.

## 8. References

- (1) Sundback, C. A., Beer, J. M., and Sarofim, A. F., 1985, Fragmentation Behavior of Single Coal Particles in a Fluidized Bed, *Twentieth Symposium (International) on Combustion*. The Combustion Institute, Pittsburgh, 1495-1504.
- (2) Mitchell, R. E. and McLean, W. J., 1982, On the Temperature and Reaction Rate of Burning Pulverized Fuels. *Nineteenth Symposium (International) on Combustion*. The Combustion Institute, Pittsburgh, 1113-1122.
- (3) Field, M. A., Gill, D. W., Morgan, B. B., and Hawksley, P. G. W., 1967, *Combustion of Pulverized Coal*, BCURA, Chap. 6 186-195.
- (4) Reyes, S. and Jensen, K. F., 1986a, Percolation Concepts in Modelling of Gas-solid Reactions I. Application to Char Gasification in the Kinetic Regime. *Chem. Eng. Sci.* **41**, 333-343.
- (5) Reyes, S. and Jensen, K. F., 1986b, Percolation Concepts in Modelling of Gas-solid Reactions I. Application to Char Gasification in the Diffusion Regime. *Chem. Eng. Sci.* **41**, 345-354.
- (6) Kerstein, A. R. and Bug, A. L. R., 1986, Scaling Theory of Pore Growth in a Reactive Solid, *Phys. Rev. B* **34**, 1754-1761.
- (7) Sahimi, M., and Tsotsis, T. T., 1988, Statistical Modeling of Gas-solid Reaction with Pore Volume Growth: Kinetic Regime. *Chem. Eng. Sci.*, **43**, 113-121.
- (8) Kerstein, A. R. and Edwards, B. F., 1986, Percolation Model for Simulation of Char Oxidation and Fragmentation Time-Histories, *Chem. Eng. Sci.*, **42**, 1629-1634.
- (9) Sarofim, A. F., Howard, J. B., and Padia, A. S., 1977, The Physical Transformation of the Mineral Matter in Pulverized Coal Under Simulated Combustion Conditions, *Combustion Science & Technology*, **16**, 187-204.
- (10) Helble, J. J. and Sarofim, A. F., 1987, Influence of Char Fragmentation on Ash Particle Size Distribution, preprint.
- (11) Holve, D. J., 1986, In Situ Measurement of Flyash Formation from Pulverized Coal, *Combustion Science & Technology*, **44**, 269-287.
- (12) Sahimi, M., and Tsotsis, T. T., 1987, Dynamic Scaling for the Fragmentation of Reactive Porous Media, *Phys. Rev. Lett.*, **59**, 888-891.
- (13) Smith, I. W., 1971, The Kinetics of Combustion of Size Graded Pulverized Fuels in the Temperature Range 1200-2700 K, *Combustion & Flame*, **17**, 304-313.
- (14) Walker, P. L., Ruskino, F., Austin, L. G., 1967, Gas Reactions of Carbon, *Advances in Catalysis*, **11**, 133-221.
- (15) Field, M. A., 1970, Measurements of the Effect of Rank on Combustion Rates of Pulverised Coal, *Combustion & Flame*, **14**, 237-248.
- (16) Wall, T. F., Gururajan, V. S., 1986, Combustion Kinetics and the Heterogeneous Ignition of Pulverized Coal, *Combustion & Flame*, **66**, 151-157.

# Flowfield Simulations in Industrial Furnace Configurations

Paul A. Gillis and Philip J. Smith

Combustion Computations Laboratory  
75 CTB, Brigham Young University  
Provo, Utah 84604

## 1 Introduction

A fundamental element of comprehensive pulverized-fuel combustion modelling is the description of the turbulent gaseous flow field within the furnace. As part of a program to develop a three-dimensional coal combustion code, a non-reacting gas flow dynamics model has been developed. This flow model, GAS3D, has been demonstrated in a variety of industrial configurations including corner-fired, cross-fired, and wall-fired furnace geometries. This paper discusses the components and capabilities of the model and presents comparisons between experimental data and model predictions for a wall-fired furnace.

The emphasis of this paper is on evaluating model performance. Experimental data has been obtained from Consolidation Coal Company for a wall-fired furnace. This configuration has been simulated with GAS3D using three different turbulence models. A description of the flow patterns predicted within the furnace are given. Comparisons are made between the predictions and experimental data and between the different turbulence models.

## 2 Solution Method

Steps common to all finite difference numerical techniques are the formulation of the equations, discretization of these equations, and the solution of the resulting coefficient matrices. GAS3D couples the momentum and continuity equations with the SIMPLE algorithm (1), utilizes a first-order hybrid upwind and central differencing scheme, and iteratively solves the difference coefficient matrices by approximating them as tridiagonal systems, which are solved with the Thomas algorithm.

The SIMPLE (Semi-Implicit Method for solving Pressure Linked Equations) algorithm is a technique for solving the equations of motion and continuity in a decoupled fashion. It requires a initial guess of the pressure field which is then updated through the calculation of a pressure correction. This method of solving the pressure field can require hundreds of iterations and alternative numerical techniques are being investigated. These alternatives include solving the equations in a coupled manner, similar to Vanka's BLIMM method (2) and the use of multigrid algorithms (3).

Finite difference coefficient matrices are often very sparse and the direct inversion of these matrices is rarely practical. Due to the first-order differencing of convection terms employed in GAS3D, the matrices formed are heptadiagonal. Each matrix is first approximated as a series of three tridiagonal matrices. These tridiagonal matrices are then solved individually with the Thomas algorithm and the solution procedure is repeated several times to resolve the coupling in the three coordinate directions. This matrix solver was initially observed to account for up to 65% of the overall run time on a CONVEX C-1 computer. Reordering the inner loops of the Thomas algorithm eliminated recursion and allowed for vectorization of the solver. This resulted in a significant reduction in matrix solution (~ 80 %) and overall computational (~ 40 %) time.



### 3 Model Capabilities

The model allows for simulations to be made in either the Cartesian or polar coordinate system. Initial validation of the model was made through comparisons with the predictions from an extensively evaluated axisymmetric gas dynamics code (4). A case was first run and documented with the axisymmetric model. This axisymmetric geometry was input and flow was simulated with the three-dimensional model for both coordinate systems. Predictions from the 3-D polar case were indistinguishable from the axisymmetric run. Cartesian predictions were similarly validated through comparison.

GAS3D has been written in a modular manner to aid understanding and ease modification. The model consists of a main driver and forty-four subroutines, each made up of an average of 134 lines of FORTRAN coding. All boundary conditions are controlled by a single three-dimensional array which specifies each cell (computational node) as being part of an inlet, flow field, or a wall (intrusion). Complex geometries can be easily simulated by input to this geometry array. Thus, a preprocessor can prepare this array for model input. Inlet velocity profiles, including swirling burners, can also be input directly to the code. Inlets and outlets on all six faces of the computational domain are possible through the same array. There is no limitation to the number of inlets or outlets on any one face, nor the number of faces having inlets, outlets, or both. However, if an outlet is located within a recirculation zone, an overall mass balance cannot be adequately closed and the code will not fully converge. The model will also handle structural intrusions at any point in the flow field. Intrusions are needed to model such important features as inlet quarls, ash bins, tube banks, clipped corners, and the furnace nose. Test cases have been successfully converged which included constricted exits, flow around successive baffles, and bluff bodies surrounded on all six sides by the flow field.

### 4 Turbulence Models

The differential equation set employed in the model was derived from the vector forms of the conservation equations for mass and momentum (5). The equations were manipulated into a standard steady-state form to ease differencing. The instantaneous form of the expanded conservation equations were Favre averaged to allow for a computationally feasible length scales:

$$\bar{\phi} \equiv \frac{\overline{\rho\phi}}{\bar{\rho}} \quad (1)$$

The Reynold's stresses,  $\rho\overline{u_i u_j}$ , where  $u_i$  is the fluctuating component of velocity in the  $i$ th direction, are modelled with the Boussinesq hypotheses:

$$-\overline{u_i u_j} = -\mu_t \nabla \bar{u} \quad (2)$$

The time averaged differential equations can be manipulated to resemble the instantaneous form of the equations by combining the molecular viscosity,  $\mu_t$ , with the eddy diffusivity. This differential equation set, for both the Cartesian and cylindrical coordinate systems, is presented in its Favre averaged form in Table 1.

Turbulence closure models have been developed for varying levels of sophistication. The most basic models, such as the constant eddy diffusivity model and Prandtl's mixing length model, contain simplifications which normally restrict their application. The most commonly used turbulence model is the two-equation  $k-\epsilon$  model. Its popularity is due in part to the disadvantages of its more sophisticated alternatives, namely, second-order closure models and large-eddy simulations. These alternatives are hindered by the enormous increase in computational resources

needed to either solve the Reynolds stress transport equations in second-order closures or resolve the fine time and spacial scales required for large-eddy simulations.

The simplest turbulence assumption is that of constant eddy diffusivity. Because turbulence is normally generated due to shear forces in the gases, this assumption is rarely true. The a priori determination of an average eddy diffusivity is difficult. A slightly more sophisticated closure scheme is the Prandtl's mixing length model. This model, given by Equation 3, relates the eddy diffusivity to the mean velocity gradient.

$$\mu_t = \rho l_m^2 |\nabla \bar{u}| \quad 3)$$

The main drawback with this model is the determination of the mixing length,  $l_m$ , for complex flows. The value for  $l_m$  has been empirically determined for a number of simple jets and flows but a value of  $l_m$  for recirculating and three-dimensional flows is difficult to determine.

The k- $\epsilon$  turbulence model was introduced to provide a means of modeling the transport of k, the turbulent kinetic energy, and  $\epsilon$ , the dissipation of turbulent kinetic energy. Transport equations are devised for both k and  $\epsilon$  that include terms to model convection, diffusion, production, and dissipation of these quantities. The differential equations for k and  $\epsilon$ , including the generation term, G, used in the model are given in Table 1. These equations are solved for each gas phase iteration. After obtaining local values for k and  $\epsilon$ , the local eddy diffusivity is calculated from the Prandtl-Kolmogorov relationship:

$$\mu_t = \frac{C_\mu \rho k^2}{\epsilon}, C_\mu = 0.09 \quad 4)$$

GAS3D currently contains options for the use of a constant eddy diffusivity, the Prandtl's mixing length turbulence model, or the standard k- $\epsilon$  model.

## 5 Reactor Flow Patterns

The pilot scale furnace simulated in this paper is operated by Consolidation Coal Corporation in Liberty, Pennsylvania. The furnace is approximately  $\frac{1}{10}$  scale of a full utility boiler and is fired from four swirled burners. The burners are located on a single wall in a diamond configuration and are all swirled in the same direction. The outlet is located above the burners on the east wall. Details about the furnace configuration can be seen in Figures 1 and 2. The furnace geometry is similar in design to large industrial boilers and contains an ash bin, furnace nose, and several clipped corners. This geometry was modelled with a grid that contained 35 points in the x or depth direction, 45 points in the y or width direction, and 65 points in the z or height direction. Converged results for this 102375 node case were obtained using the three turbulence models described previously. Each turbulence model produced significantly differing results.

The constant eddy diffusivity model produced the simplest flow field. This flow field contained only two large scale vortices. The largest vortex was predominantly visible in the x planes, flowed in the clockwise direction, and extended over the entire length of the reactor. No large recirculation zones were predicted in the z planes, but burner centerline recirculation was present. Figure 1A illustrates flow patterns at a normalized width of 0.5. This figure shows a strong vortex centered below the burners that extends approximately half way up the reactor. The shaded areas in these figures represent reactor walls and the arrows signify velocity vectors constructed from the two components of velocity parallel to the designated plane. The length and direction of each vector represents predicted velocity for the location specified by the vector tail. In order to reduce congestion, less than one half of the computational nodes are represented with vectors. There are

two sizes of unfilled arrowheads and their ratio along with the scale for the small vectors is given in Figures 1 and 2.

Figure 1B provides the flow field prediction for the center y plane using a mixing length turbulence model. This figure shows a highly viscous type flow, especially in the near-burner region and the absent of major vortices in this plane. The viscous flow is generated because the mixing length model produces high eddy diffusivity values in the high velocity gradient regions around the burners. The x plane predictions show high velocities along the north wall which decrease to near stagnation along the south wall. Strong counter-clockwise swirling vortices are found in all the z planes starting in the ash bin and extending beyond the furnace nose.

The  $k-\epsilon$  turbulence model yielded the most complex flow field prediction. Figure 1C reveals numerous swirling patterns in this single plane. Separate vortices in the ash bin, above the burners, and behind each burner, as well as strong burner centerline recirculations are all predicted. Clockwise swirling vortices are observed in nearly all the z planes. Numerous localized vortices can be found in the predicted x planes. The  $k-\epsilon$  turbulence model predicted a central recirculation zone with gases flowing downward in the center of the reactor, but flowing upward near the east, west, north and south walls. Figure 1 illustrates the vast differences in both magnitude and direction of the velocities predicted by the three turbulence models.

## 6 Data Comparisons

Velocity measurements in the Consol furnace were made with a  $\frac{1}{4}$  inch pitot tube connected to an electro-manometer. The y component of velocity was not included in these measurements. Experimental velocity data were obtained for 50 points all above the burners. The filled arrowheads in Figures 1 and 2 represent these data points. In Figure 2, all 50 data points are shown with the  $k-\epsilon$  predictions. It should be noted in Figure 2 that the data points are for the vertical component of velocity only.

The predictions in Figure 1C agree significantly better than the predictions of Figures 1A or 1C. The agreement between predictions and data in Figures 1A and 1B is poor. For example, the  $k-\epsilon$  simulation is the only model that predicted downward flow in the reactor center and higher velocities on east wall than on the west wall. The majority of experimental vectors in Figure 1C agree with the predictions in both direction and magnitude. The obvious exceptions are the center data vectors at a normalized height of 0.58 and 0.70. There are several possible reasons for these discrepancies. The most probable cause is that the central recirculation zone is being overpredicted by the  $k-\epsilon$  model. An earlier study on two-dimensional swirling flows faulted the  $k-\epsilon$  model with overpredicting the length of recirculation zones (6). The transient nature of turbulence could create difficulties in correcting determining direction and magnitude of gas velocity in a recirculation zone. The steady-state velocity predicted by GAS3D could be difficult to verify in a region where turbulent eddies are constantly passing. More precise inlet conditions could also aid isolated the cause of these discrepancies.

Figure 2 shows predicted flowfields at three different depths: Figure 2A represents a x plane near the burners and east wall; Figure 2B represents a x plane at a normalized depth of 0.5; and Figure 2C is near the west wall. The swirl in the secondary of the burners drives the lower clockwise vortices found in Figures 2A and 2B. A counter clockwise swirling pattern can also be found in outlet in the upper part of Figures 2A and 2B. Although not always exact in magnitude, the  $k-\epsilon$  model appears to predict the trends shown by the data. In Figure 2A, the model predicted the change from higher north wall velocities to higher south wall velocities as the gases flowed upward. The two data points in direct directional disagreement with predictions seen in Figure 1C can also be found in Figure 2B. It is probable that if the central recirculation zone length

could be better simulated the agreement in the top data plane (height = 0.70) would improve. The general agreement illustrated in Figures 1C, 2A, 2B, and 2C is reasonable considering the complexity of the flow.

The presence of a fine vortex structure in the  $k-\epsilon$  predictions presents some interesting questions. Additional work is needed to determine the dependence of vortex structure on coarseness of the grid. Additional vortex structure could be revealed by converging this case with finer grid sizing. Previous investigators have found that the inlet conditions are vital to correctly simulating turbulent flow. Further investigation is warranted into determining the sensitivity of solutions to such parameters as swirl number and inlet velocity profile.

## 7 Conclusion

A three-dimensional flow model has been developed and validated for simulating complex enclosed flow. The selection of turbulence model has been shown to greatly affect flow predictions. The  $k-\epsilon$  model appeared to represent significant predictive improvement over the simpler turbulence models. Although the  $k-\epsilon$  model appeared to overpredict the size of some recirculation zones, it yielded predictions in general agreement with experimental data. Further study is warranted to determine the applicability of other turbulence models and the effect of grid resolution and inlet conditions on predictions.

## 8 Acknowledgements

We wish to thank Consolidation Coal Corporation for providing the experimental data used in this paper. Additional support for this research was provided by the following organizations: Advanced Fuel Resources, Inc., Babcock and Wilcox, Combustion Engineering, Inc., Consolidation Coal Company, Electric Power Research Institute, Empire State Electric Energy Research Co., Foster Wheeler Development Co., Tennessee Valley Authority, U.S. Department of Energy - METC, U.S. Department of Energy - PETC, and Utah Power and Light Co.

## 9 References

1. Patankar, S.V., Numerical Heat Transfer and Fluid Flow, McGraw-Hill Book Company, New York (1980).
2. Vanka, S.P., "Block-Implicit Multigrid Solution of Navier-Stokes Equations in Primitive Variables," Journal of Computational Physics, Vol. 65, 138-158 (1986).
3. Brandt, A., Multigrid Techniques: 1984 Guide with Applications to Fluid Dynamics, GMD-Studien Nr. 85, Schloss Birlinghoven, West Germany (1984).
4. Smoot, L.D. and Smith, P.J., Coal Combustion and Gasification, Plenum Press, New York (1985).
5. Bird, R.B., Stewart, W.E., and Lightfoot, E.N., Transport Phenomena, John Wiley & Sons, New York (1960).
6. Sloan, D.G., Smith, P.J., and Smoot, L.D., "Modeling of Swirl in Turbulent Flow Systems," Prog. Energy Combust. Sci., Vol. 12, 163-250 (1986).

Table 1. Differential Equation Set for GAS3D

Part A. Cartesian Coordinate System

$$\frac{\partial(\bar{\rho}\tilde{u}\phi)}{\partial x} + \frac{\partial(\bar{\rho}\tilde{v}\phi)}{\partial y} + \frac{\partial(\bar{\rho}\tilde{w}\phi)}{\partial z} - \frac{\partial}{\partial x} \left( \Gamma_{\phi} \frac{\partial\phi}{\partial x} \right) - \frac{\partial}{\partial y} \left( \Gamma_{\phi} \frac{\partial\phi}{\partial y} \right) - \frac{\partial}{\partial z} \left( \Gamma_{\phi} \frac{\partial\phi}{\partial z} \right) = S_{\phi}$$

Equation	$\phi$	$\Gamma_{\phi}$	$S_{\phi}$
Continuity	1	0	0
X Momentum	$\tilde{u}$	$\mu_e$	$-\frac{\partial P}{\partial x} + \frac{\partial}{\partial x} \left( \mu_e \frac{\partial \tilde{u}}{\partial x} \right) + \frac{\partial}{\partial y} \left( \mu_e \frac{\partial \tilde{u}}{\partial x} \right) + \frac{\partial}{\partial z} \left( \mu_e \frac{\partial \tilde{u}}{\partial x} \right)$
Y Momentum	$\tilde{v}$	$\mu_e$	$-\frac{\partial P}{\partial y} + \frac{\partial}{\partial x} \left( \mu_e \frac{\partial \tilde{u}}{\partial y} \right) + \frac{\partial}{\partial y} \left( \mu_e \frac{\partial \tilde{u}}{\partial y} \right) + \frac{\partial}{\partial z} \left( \mu_e \frac{\partial \tilde{u}}{\partial y} \right)$
Z Momentum	$\tilde{w}$	$\mu_e$	$-\frac{\partial P}{\partial z} + \frac{\partial}{\partial x} \left( \mu_e \frac{\partial \tilde{u}}{\partial z} \right) + \frac{\partial}{\partial y} \left( \mu_e \frac{\partial \tilde{u}}{\partial z} \right) + \frac{\partial}{\partial z} \left( \mu_e \frac{\partial \tilde{u}}{\partial z} \right)$
Turbulent Energy	k	$\frac{\mu_e}{\sigma_k}$	$G - \bar{\rho}\epsilon$
Dissipation Rate	$\epsilon$	$\frac{\mu_e}{\sigma_{\epsilon}}$	$\left( \frac{\epsilon}{k} \right) (c_1 G - c_2 \bar{\rho}\epsilon)$

where:

$$G = \mu_e \left\{ 2 \left[ \left( \frac{\partial \tilde{u}}{\partial x} \right)^2 + \left( \frac{\partial \tilde{u}}{\partial y} \right)^2 + \left( \frac{\partial \tilde{u}}{\partial z} \right)^2 \right] + \left( \frac{\partial \tilde{u}}{\partial y} + \frac{\partial \tilde{v}}{\partial x} \right)^2 + \left( \frac{\partial \tilde{u}}{\partial z} + \frac{\partial \tilde{w}}{\partial x} \right)^2 + \left( \frac{\partial \tilde{v}}{\partial z} + \frac{\partial \tilde{w}}{\partial y} \right)^2 \right\}$$

Part B. Cylindrical Coordinate System

$$r \frac{\partial(\bar{\rho}\tilde{u}\phi)}{\partial x} + \frac{\partial(\bar{\rho}\tilde{v}\phi)}{\partial r} + \frac{\partial(\bar{\rho}\tilde{w}\phi)}{\partial \theta} - r \frac{\partial}{\partial x} \left( \Gamma_{\phi} \frac{\partial\phi}{\partial x} \right) - \frac{\partial}{\partial r} \left( r \Gamma_{\phi} \frac{\partial\phi}{\partial r} \right) - \frac{\partial}{\partial \theta} \left( \frac{\Gamma_{\phi}}{r} \frac{\partial\phi}{\partial \theta} \right) = S_{\phi}$$

Equation	$\phi$	$\Gamma_{\phi}$	$S_{\phi}$
Continuity	1	0	0
X Momentum	$\tilde{u}$	$\mu_e$	$-r \frac{\partial P}{\partial x} + r \frac{\partial}{\partial x} \left( \mu_e \frac{\partial \tilde{u}}{\partial x} \right) + \frac{\partial}{\partial r} \left( \mu_e r \frac{\partial \tilde{u}}{\partial x} \right) + \frac{\partial}{\partial \theta} \left( \mu_e \frac{\partial \tilde{u}}{\partial x} \right)$
R Momentum	$\tilde{v}$	$\mu_e$	$-r \frac{\partial P}{\partial r} + r \frac{\partial}{\partial x} \left( \mu_e \frac{\partial \tilde{u}}{\partial r} \right) + \frac{\partial}{\partial r} \left( \mu_e r \frac{\partial \tilde{u}}{\partial r} \right) + \frac{\partial}{\partial \theta} \left( \mu_e \frac{\partial \tilde{u}}{\partial r} - \frac{\tilde{w}}{r} \right) - \frac{2\mu_e}{r} \frac{\partial \tilde{w}}{\partial \theta} - \frac{2\tilde{u}\mu_e}{r} + \bar{\rho}\tilde{w}^2$
$\theta$ Momentum	$\tilde{w}$	$\mu_e$	$-\frac{\partial P}{\partial \theta} + r \frac{\partial}{\partial x} \left( \mu_e \frac{\partial \tilde{u}}{\partial \theta} \right) + \frac{\partial}{\partial r} \left( \mu_e r \frac{\partial \tilde{u}}{\partial \theta} - \mu_e \tilde{w} \right) + \frac{\partial}{\partial \theta} \left[ \left( \frac{\mu_e}{r} \right) \left( \frac{\partial \tilde{w}}{\partial \theta} + 2r \frac{\tilde{v}}{\partial r} \right) \right] + \mu_e \left( \frac{\partial \tilde{w}}{\partial r} + \frac{\partial \tilde{v}}{r \partial \theta} - \frac{\tilde{w}}{r} \right) - \bar{\rho}\tilde{v}\tilde{w}$
Turbulent Energy	k	$\frac{\mu_e}{\sigma_k}$	$r(G - \bar{\rho}\epsilon)$
Dissipation Rate	$\epsilon$	$\frac{\mu_e}{\sigma_{\epsilon}}$	$\left( r \frac{\epsilon}{k} \right) (c_1 G - c_2 \bar{\rho}\epsilon)$

where:

$$G = \mu_e \left\{ 2 \left[ \left( \frac{\partial \tilde{u}}{\partial x} \right)^2 + \left( \frac{\partial \tilde{v}}{\partial r} \right)^2 + \left( \frac{\partial \tilde{w}}{r \partial \theta} + \frac{\tilde{v}}{r} \right)^2 \right] + \left( \frac{\partial \tilde{u}}{\partial r} + \frac{\partial \tilde{v}}{\partial x} \right)^2 + \left( \frac{\partial \tilde{u}}{r \partial \theta} + \frac{\partial \tilde{w}}{\partial x} \right)^2 + \left( \frac{\partial \tilde{v}}{r \partial \theta} + \frac{\partial \tilde{w}}{r^2} \right)^2 \right\}$$

# U-W Velocity Vectors

Large to Small Vector Length Ratio = 20  
Velocity Scale: 1 inch = 1.44 m/s

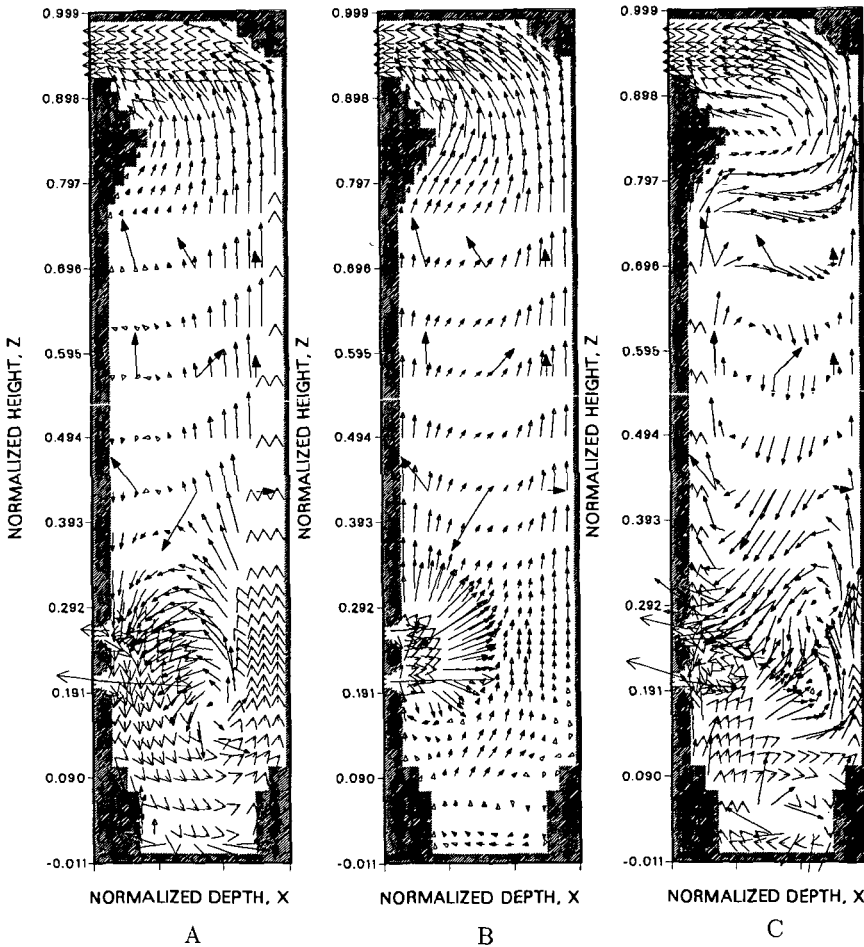


Figure 1. Comparison of velocity predictions and experimental data at a normalized width of 0.5 for the following turbulence models: A, constant eddy diffusivity; B, simple mixing length model; and C,  $k-\epsilon$  model.

# V-W Velocity Vectors

Large to Small Vector Length Ratio = 20  
Velocity Scale: 1 inch = 1.44 m/s

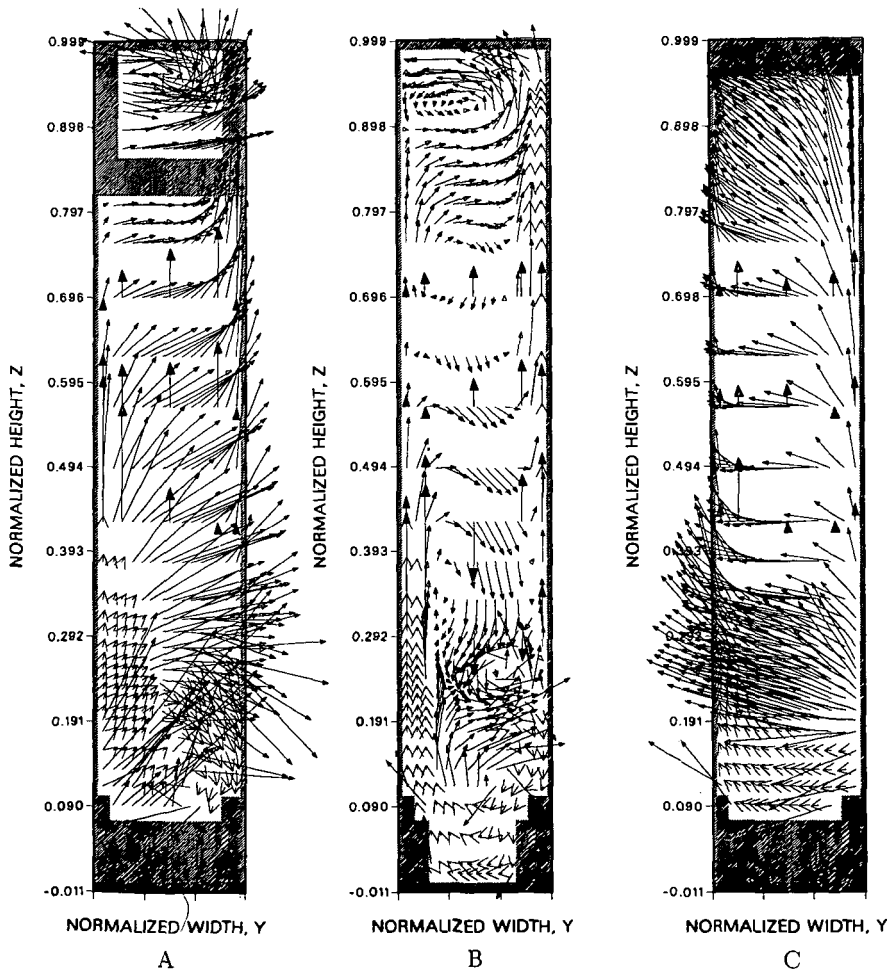


Figure 2. Comparison of velocity predictions and the vertical component of velocity measured in three x planes: A, normalized depth of 0.17; B, normalized depth of 0.50; C, normalized depth of 0.83.